Chapter 12

THE AURORA

Section 12.1 J. A. Whalen
Section 12.2 R. R. O'Neil and R. H. Picard

12.1 PHENOMENOLOGY, MORPHOLOGY, AND OCCURRENCE

12.1.1 General Characteristics of the Aurora

The aurora is the name given to the light resulting from the precipitation of electrons and protons from the magnetosphere into the earth's atmosphere. This light consists of atomic line spectra and molecular band spectra characteristic principally of oxygen and nitrogen, the chief constituents of the upper atmosphere ionized or excited by collisions with these precipitating particles.

Associated with auroral precipitation and ionization, currents called auroral electrojet currents can flow in the atmosphere. These currents produce magnetic fields detectable at ground level by magnetometers and form the basis for magnetic indicators of auroral activity (see Chapter 4).

Subsection 12.1.1 is a qualitative introductory discussion of the general classes of aurora in terms of the precipitating particles, the source of each type of particle in the earth's magnetosphere, the energy spectrum of each, the height at which each produces maximum ionization and excitation in the earth's atmosphere, the resulting electron density for each, the spatial structure of each, and a map of the general global morphology of each. The succeeding subsections provide tables, graphs, and definitions that specify and characterize auroral properties in as quantitative terms as are currently available.

12.1.1.1 Particle Energy—Ionization and Excitation Height Relation. Particles penetrate into the atmosphere to a height dependent on their initial kinetic energy, the higher the energy the deeper the penetration and therefore the lower the altitude of the resulting ionization and excitation.

The condition for electrons (monoenergetic and isotropic) is shown in a graph of height of maximum production of ionization versus electron energy in Figure 12-1. Note that the height scale is divided into three sections which are the three fundamental altitude regimes: the D region (50–90 km), E region (90–160 km), and F region (160–500+ km). The particle energies and morphologies of each are dependent on the source regions in the magnetosphere.

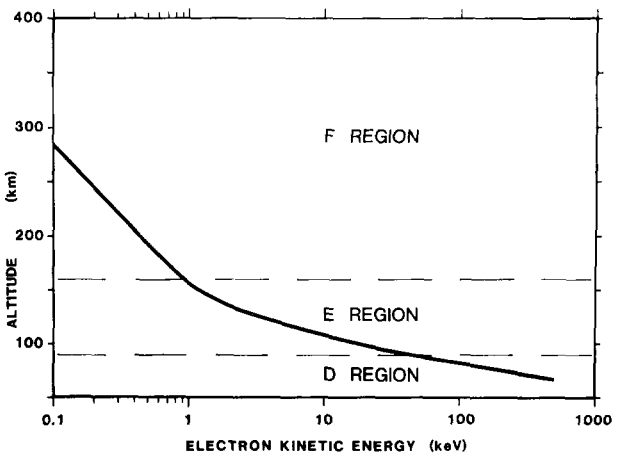

Figure 12-1. Altitude of maximum production of ionization in the upper atmosphere by auroral electrons as a function of incident electron kinetic energy. Calculation by Rees [1964] assumes mono-energetic electrons of isotropic incidence. Dashed lines are the approximate boundaries of the D, E, and F regions which are the principal ionospheric altitude regions.

12.1.1.2 Particle Energy—Magnetospheric Regime Relation. These general source regions are the magnetosheath, the plasmasheet, and the Van Allen or so-called trapped radiation belts. These regions are occupied by electrons of kinetic energies of ~0.1 keV, 1–10 keV, and >40 keV, respectively. (Protons also exist in these regions, the energies of which are greater than electron energies by a factor of ~5).

Quite fortuitously, electrons that precipitate into the atmosphere with energies characteristic of these three magnetospheric regimes produce maximum ionization and excitation in the three different altitude regimes; that is, ~0.1 keV electrons ionize principally at heights in the F region, 1–10 keV in the E region, and >40 keV in the D region.

A cross section of the magnetosphere through the noon-midnight meridian schematically defines these regions to-

gether with their particle populations and associated ionospheric height regimes (Figure 12-2).

The origin of the magnetosheath plasma is the solar wind proton-electron plasma, which is approximately thermalized in passing through the bow shock on the solar side of the

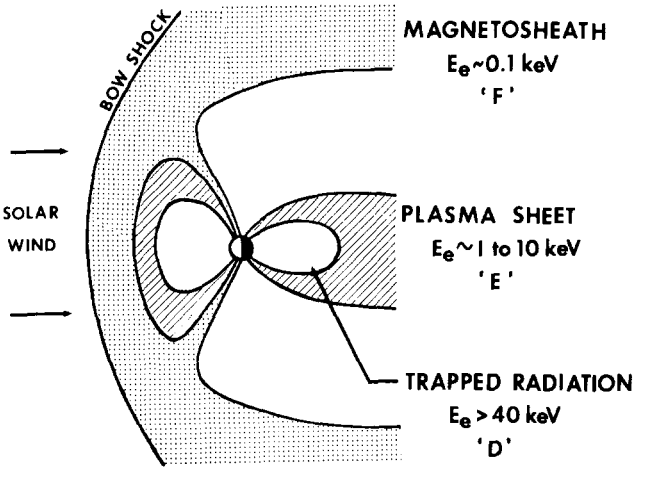

Figure 12-2. Schematic of the magnetosphere of the earth in noon-midnight cross section showing principal magnetospheric domains, the associated particle populations via representative electron kinetic energy, Ee, and the ionospheric region (F, E or D) in which these particles produce maximum ionization.

magnetosphere. These magnetosheath particles are thought to be the source of the plasma sheet particles and they, in turn, to be the source of the Van Allen radiation belt particles. However, the route of entry of the particles into these two regimes and the processes by which they are accelerated are not understood. As such, they remain the fundamental unresolved questions of magnetospheric physics and the subject of much active research (see Chapter 8). It is not the purpose here to deal with these questions, but it is well to note that the fundamental links between the magnetosphere and the ionosphere make the ionospheric measurements important ways of probing the magnetosphere in pursuit of these answers.

12.1.1.3 Spatial Structure. Another key distinction that one must make between auroras is their spatial structure, that is, whether they are relatively structured or unstructured. This distinction is most evident in the 1 to 10 keV plasmasheet precipitation, which represents the bulk of the energy of auroral precipitation. Here the structured component is known as the discrete aurora. Since it is the most visible, it is popularly known as "the aurora". The unstructured component is known as the continuous aurora (also called mantle and diffuse aurora). Although often neglected because its faintness and absence of contrast make it difficult to observe, this unstructured aurora comprised 80% of the total energy input into the polar region at solar maximum (IGY) and 50% in solar minimum (IQSY) [Sandford, 1968].

These two structural types can be distinguished in the large scale photographs of the aurora by the Defense Meteorological Satellite System (DMSP) (Figure 12-3). The bright structured forms at high latitude are the discrete au-

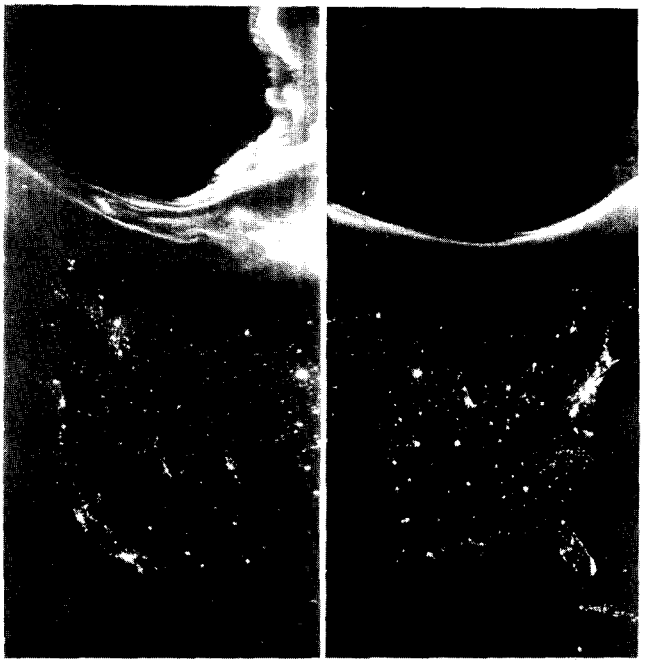

Figure 12-3. Two DMSP photographs showing the midnight aurora across the North American continent defined by city lights.

roras; the relatively faint glow at lower latitudes is the continuous aurora. City lights show the location and scale of the photographs.

12.1.1.4 Morphology of the E Region. The most familiar model of the aurora is the Feldstein and Starkov [1967] auroral oval, a statistical compilation as determined from auroral all-sky camera photographs taken during the IGY. The oval is a band encircling the magnetic pole but displaced eccentrically to higher latitude in the day sector as a consequence of the distortion of the earth's magnetic field by the solar wind. Figure 12-4 shows the oval projected on a map of the northern hemisphere in magnetic coordinates [Whalen, 1970]. The pattern, fixed with respect to the sun, is shown in four different orientations with respect to the earth at the indicated values of UT. With increasing magnetic activity, the oval expands and moves equatorward.

The oval typical of moderate conditions (that designated by the magnetic index Q = 3) will be used to form a reference system for other types of auroras. The coordinate system of the oval, Corrected Geomagnetic Latitude and Corrected Geomagnetic Local Time, is shown in six different plots in Figure 12-5. The Q = 3 oval is drawn in

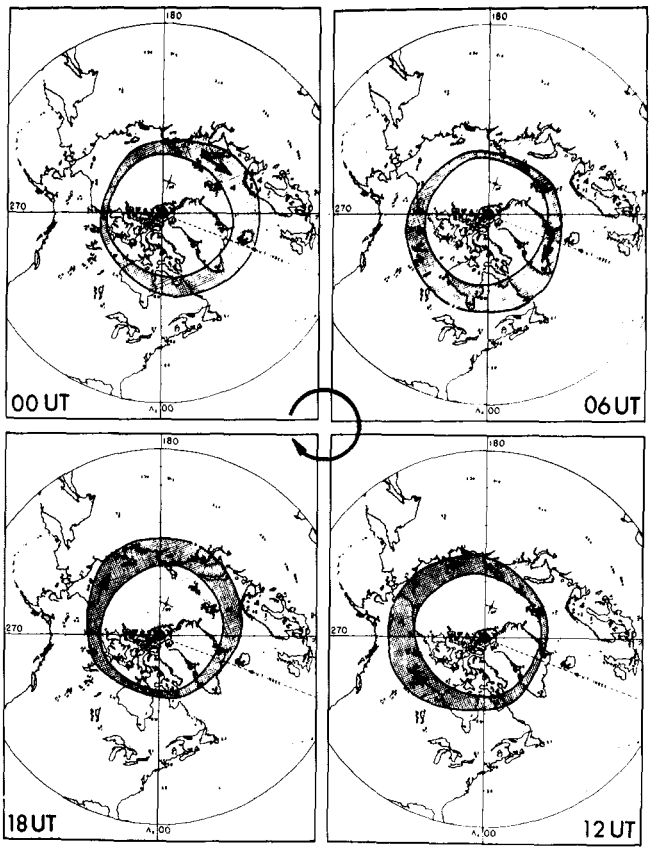

Figure 12-4. The auroral oval, the locus of maximum discrete (E) auroral activity, projected on the north polar region as mapped in Corrected Geomagnetic latitude and longitude. The orientations of the oval at four different values of UT are shown.

each plot bounded by the heavy lines. The shaded areas schematically map the types of auroras differentiated as to structured (top row) and unstructured (bottom row), and to particle energy/ionospheric regime by columns.

The E type auroras appear in the center column of Figure 12-5, the discrete auroral oval itself (above) and the continuous aurora (below). The continuous aurora tends to overlap the oval in the night sector [Whalen et al., 1977], but to locate equatorward of the oval in the day sector [Whalen et al., 1971]. In quiet times the discrete aurora disappears entirely and the continuous aurora remains [Wagner et al., 1973]. Although the continuous aurora forms a band that encircles the pole for all levels of activity, its location can change and the total energy fluxes can vary by several orders of magnitude. In terms of the magnetosphere, the continuous aurora appears to be precipitation from the plasma sheet, both having energy spectra which can be described as Maxwellian [Rearwin and Hones, 1974].

The discrete auroral particles also apparently arise from the plasma sheet but undergo additional accelerations. A further distinction is that the continous aurora can result from both electron and proton precipitation. The discrete aurora results from electrons alone since protons effectively diffuse throughout distances of a few hundred kilometers in the atmosphere. The continuous aurora will be examined in detail in a subsequent section.

12.1.1.5 Morphology of the F Region. The F precipitation appears to have structured and unstructured components analogous to the E region (for example, all-sky photometric observations of Mende and Eather [1976]). The location of each appears to be statistically well represented by the oval—whether there are differences in the morphology of the two is not known. The ionosphere at F layer heights exhibits irregular and spread conditions throughout these regions of soft precipitation. In addition, the polar cap (the circular area poleward of the oval) is also a region of spread F.

An additional ionospheric region of importance is the F layer trough, a region of low ionization 5°–10° wide located equatorward of the oval in the night and evening sectors [Muldrew, 1965]. The poleward edge or wall of the F layer trough is a region of large electron density gradients that can cause large refractions and thus large departures from great circle propagation paths for HF. Buchau et al. [1978] treat a specific case. Pike [1976] has developed an analytical model of the F layer trough wall.

These F region precipitation patterns are shown in the left column of Figure 12-5. Thermalized solar wind from the magnetosheath impinges directly on the atmosphere to produce the dayside region but not the night sector regions, the field lines for which map down from the plasma sheet. In any case the regions are continuous in local time as shown.

One of the complications in the F layer is that the regions of production of ionization are not necessarily the bounds of the location of the ionization. This is because ions in the F-layer have relatively long lifetimes during which they can be transported considerable distances from their origin.

12.1.1.6 Morphology of the D Region. The unstructured component of the D region precipitation exists as a band generally a few degrees wide that extends from midnight to morning and sometimes is entirely circumpolar [for example, Hook, 1968]. In quiet times its locus near midnight is the equatorward edge of the continuous aurora; in active times the distribution can be quite wide. The temporal characteristics have been the subject of many studies [for example Hartz and Brice, 1967]. The occurrence of this precipitation causes D region HF absorption of relatively short duration (15 minutes) near midnight, longer (1–2 hours) in the morning sector. Structured D region auroras seem to be associated with activity in the night sector as, for example, with poleward expanding arcs during substorms. Thus they are transient in nature and occupy the midnight sector of the auroral oval. The patterns for the D region are shown schematically in the righthand column of Figure 12-5.

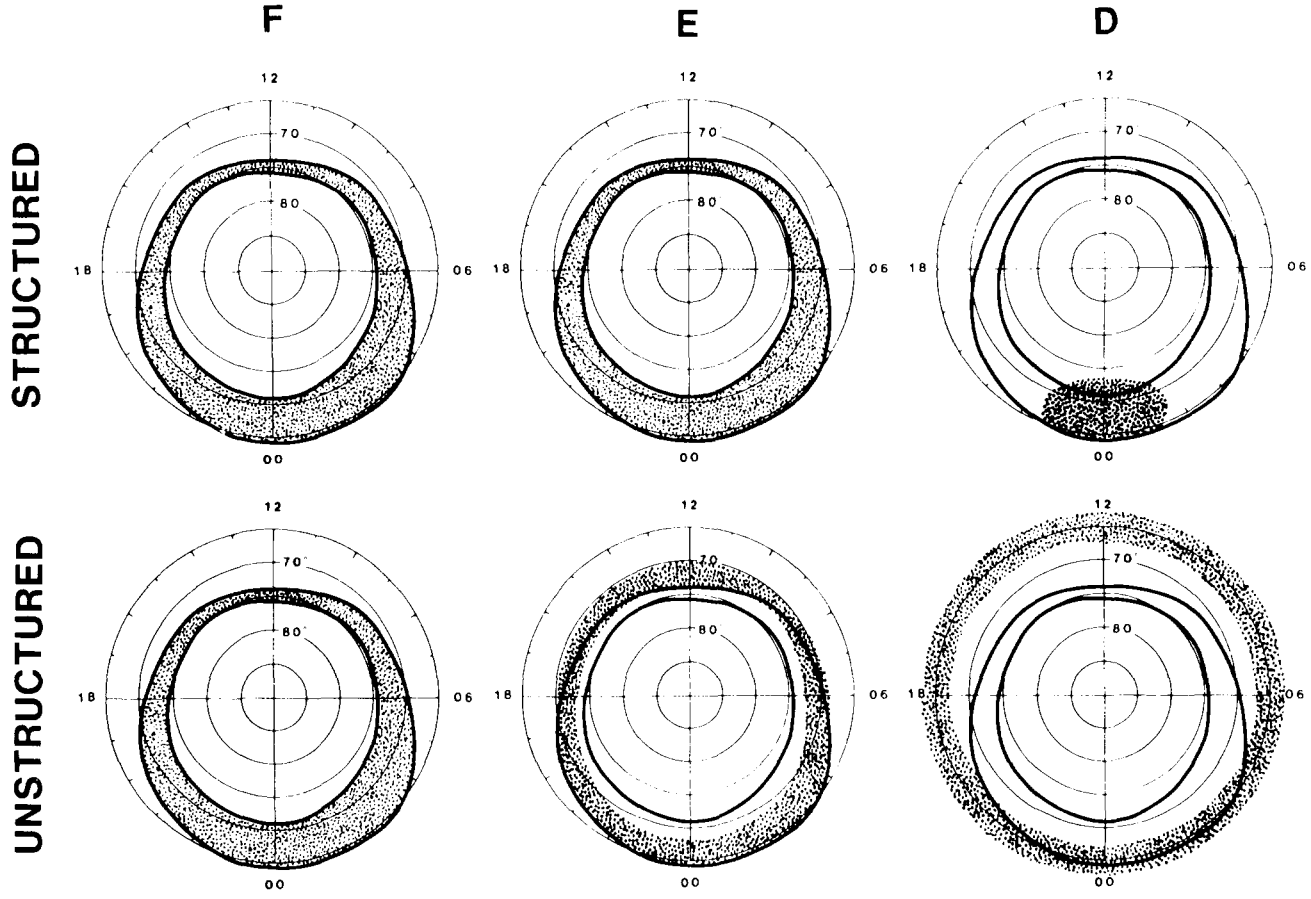

Figure 12-5. A schematic representation of the regions of structured (top row) and unstructured (bottom row) auroras differentiated as to ionospheric regime (particle energy): from left to right, F(~0.1 keV), E(1–10 keV) and D(>40 keV). Coordinate systems are CG latitude and CG local time. The Q = 3 auroral oval is defined by the heavy solid lines; the location of the specific auroras, by the shaded areas.

The unstructured pattern marks the region in which radiation belt particles "un-trap" so as to precipitate into the atmosphere. Berkey et al. [1974] have described a number of events in which the dynamics of this precipitation are detailed.

12.1.1.7 Composite. In Figure 12-5 two generalizations can be made regarding the unstructured auroras. First, in the day sector the D, E, and F precipitation and ionization production are at different latitudes (D lowest, E intermediate, and F highest) so that there should be little question as to their separate identities. Second, in the night sector the three overlap, a condition which had led to the confusion that they are a single phenomenon since they can be in the same place.

For structured auroras, E and F categories are apparently collocated at all local times and with D near midnight. Two features are of note regarding the relation between structured and unstructured auroras. All six categories overlap in the night sector. In the day sector, unstructured F auroras due to particles of magnetosheath origin are collocated with structured E and discrete aurora, the energies of which correspond to those of the plasma sheet. This has lead to the paradoxical situation that the F region has been correctly defined as being the Feldstein oval in the dayside because the photographs have detected structured E auroras (unaccountably) in the same location as the unstructured F auroras.

The foregoing is not intended to be a complete description of the auroral ionosphere but is intended to identify the *minimum* distinctions necessary for such a description. Figure 12-5 presents, schematically, all six of these phenomena together in hopes of clarifying their existence and interrelation about which a great deal of confusion exists.

12.1.2 Distribution of Auroras in Magnetic Latitude and Local Time

The global distribution of auroras has proved to be a difficult subject to quantify. A principal reason is that most studies have failed to distinguish among the large number of auroras, each of which can exhibit quite independent brightness and location on a small and large scale, short and long term.

In addition, studies have been necessarily piecemeal,

ground based studies being too small in scale and satellite studies being too short in time. The Dynamics Explorer (DE) imager addresses these contradictory elements, and if it can distinguish between the classes of auroras, promises to provide valuable information in this area.

At the present time, the available distributions are generally statistical in nature and fall into two categories: morphology of the aurora on the one hand and average values of parameters on the other. However, the former is accomplished without regard to intensity and the latter confuses intensity with location or frequency of occurrence so that the numerical values do not represent actual values. In addition these statistical measurements are ordered through a magnetic index (usually Kp) that encompasses a large variety of auroral conditions.

A second approach has shown progress in defining quantitatively the instantaneous distribution of one of these classes of aurora—the continuous aurora—throughout nearly its entire latitude-local time extent. It finds that no single parameter, magnetic or otherwise, can quantitatively describe the intensity and location of this aurora since both can vary quite independently. Rather this approach measures both intensity and location and takes these parameters to be fundamental auroral indices.

Unfortunately neither of these approaches can be considered to give adequate quantitative descriptions of the aurora in this scale at the present time: the statistical approach because of inherent limitations and the instantaneous approach because it has been demonstrated to date only on a limited basis. Nevertheless, this section will endeavor to present in each of these categories the best results which are available at the present time.

12.1.2.1 Statistical Distributions.

Frequency of Occurrence—The frequency of occurrence of aurora in the zenith as determined by all-sky camera (ASCA) in one-half hour intervals during the IGY is shown in Figure 12-6. The 70% contours define a band which was originally named the auroral oval [Feldstein, 1966] and has since been called the auroral oval zone or the statistical auroral oval. This is apparently the discrete aurora since the continuous aurora has generally too low an intensity and presents too little contrast to be seen in the zenith.

The Auroral Oval—The auroral oval (originally called the auroral oval belt) is a band encircling the pole, the high and low latitude borders of which are the average locations of the edges of auroral luminosity seen in ASCA photographs during the IGY. Such a band has been determined for each value of magnetic index Q, where Q was determined within the same 15 minute intervals of UT in which the ASCA photographs were taken but from magnetometer measurements in the midnight sector near 65°CG latitude [Feldstein and Starkov, 1967]. Figure 12-7 shows examples of ovals for three values of Q.

The ovals are thinner and displaced poleward in the day sector. In addition, the day and night sectors differ in their

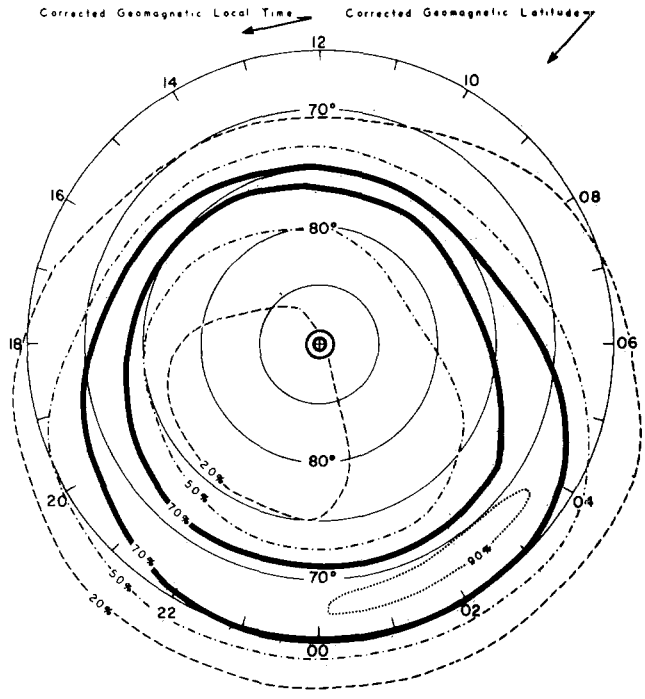

Figure 12-6. Percentage of occurrence of discrete aurora in the zenith as recorded by ASCA in the Northern Hemisphere during the period 1957–1959.

response to increasing activity, the night sector expanding in width and day sector moving equatorward. The standard deviation of these boundaries is about 1°. No clear distinction is made between discrete and continuous auroras. However, they appear not to be exclusively discrete auroras. Since the measurements were generally not in the zenith, the continuous aurora would tend to be visible particularly at large zenith angles due to VanRhijn enhancement. Thus the oval borders could be the continuous aurora and probably are in the equatorward region since the discrete aurora tends to be absent there [Lui et al., 1977; Whalen, 1983].

Although no intensity information was recorded, the oval pattern has been found in a number of cases to be quite representative of the instantaneous pattern of the aurora (for example, the DE image—Figure 12-25 in Section 12.2).

The solar cycle dependence of the oval is such that at solar minimum the midnight sector (the only sector reported) was displaced 1° to 2° poleward of its location at solar maximum [Starkov and Feldstein, 1970].

The equatorward boundary Λ_{eq}, of the auroral oval can be represented by the expression

$$\Lambda_{eq} = 72° - 0.9°Q - 5.1°\cos\left(\frac{360°}{24}\, t_{CG} - 12°\right) \tag{12.1}$$

for $Q > 1$ where Q is the magnetic index, t_{CG} is the CG local time [Starkov, 1969]. This border can be closely ap-

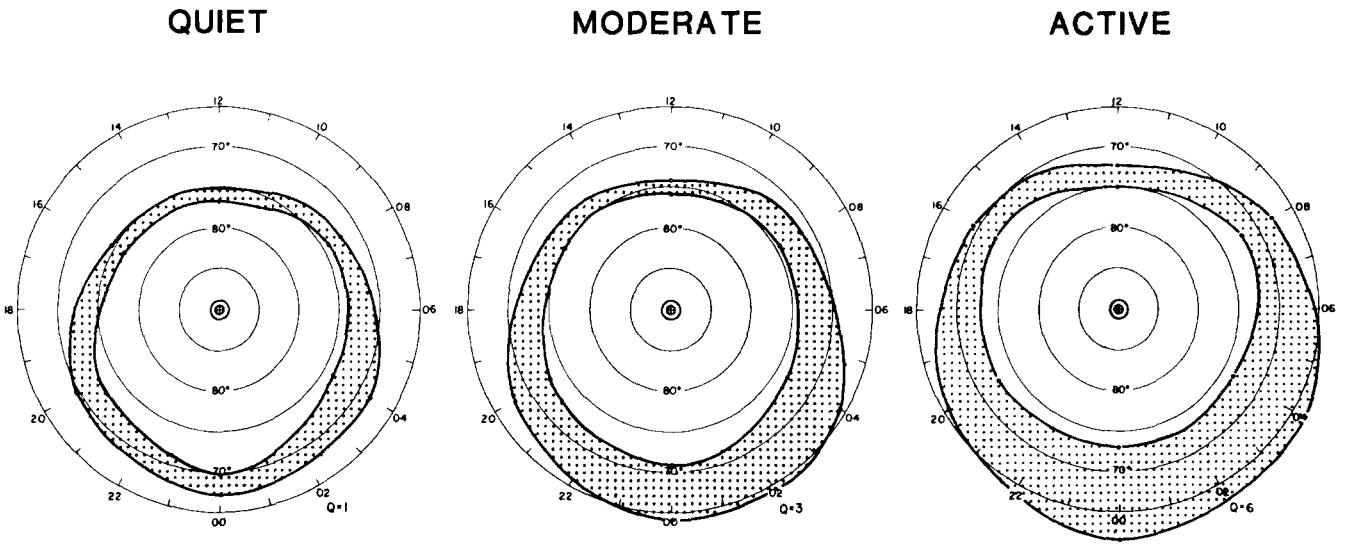

Figure 12-7. Variation in the size of the auroral oval with activity as denoted by the magnetic index Q. Coordinate system is CG latitude and CG local time.

proximate by a circle centered at 84.9°CG latitude 00:48 CG local time having a radius R = 18° + 0.9°Q [Gassman, 1973]. Holzworth and Meng [1975] have derived similar expressions for the ovals.

An example of the nature of the fit of such an offset circle will be shown in Figure 12-11 for the Q = 2 oval. Also shown in Figure 12-11 are other examples of other auroral parameters that can be ordered in such an offset pole reference frame and which will be discussed below.

The magnetic Q index is not generally available, an unfortunate circumstance because it has been the most successful single parameter in ordering auroral morphology. In the absence of the magnetically measured Q, it is possible to infer Q by taking a measurement of Λ_{eq} at a single t_{CG}, substituting these values into Equation (12.1) and solving for Q. By substituting this effective Q into Equation (12.1) one can calculate Λ_{eq} at other local times.

Average Values—A number of studies have provided distributions in magnetic latitude-local time of the average values of auroral parameters. One of the difficulties in this approach is that the measurements are ordered in terms of magnetic indices that typically span three hours. During such an interval auroral intensity and location are never fixed so that a given Kp represents a large variety of auroral conditions. In particular the aurora can move throughout a range that is generally much larger than its instantaneous extent. As a result instances of non-occurrence of aurora within a spatial interval are considered to be zero intensity and these are averaged together with cases of finite intensity within that interval. Accordingly the resulting average can produce values of intensity that never occur in nature; the average spatial distribution is one than can never occur instantaneously.

Nevertheless these average distributions have been useful in revealing some overall trends related to activity and in producing large scale spatial integrals. However, it is important to keep in mind Sandford's [1968] caveat that such distributions "give an average gross representation of parameters that show rapid and large variations in space and time."

The most extensive set of distributions of important optical auroral parameters are due to Sandford [1968]. Included in Figures 12-8 and 12-9 are contours in CG latitude—CG local time of intensity of emissions at 6300 Å, 5577 Å, and 3914 Å, and frequency of occurrence of discrete aurora for three levels of activity (quiet, moderate and disturbed based on magnetic local K indices of 0–2, 3–4, and >4 respectively) for solar cycle maximum (1958–1959) and minimum (1963).

The latitudinal distributions of these same parameters are shown at midnight and at noon for values of K from 0 to 8 for solar maximum (Figure 12-10, left) and solar minimum (Figure 12-10, right).

In addition, Sandford [1968] has shown conclusively the existence of a non-discrete form of the aurora which he termed mantle aurora. The term continuous aurora [Whalen et al., 1971] was coined to distinguish the E-region component of this aurora from the possible D-region component which Hartz and Brice [1967] had named diffuse aurora.

Sandford found that at solar maximum the mantle aurora contributed 80% of the total overall auroral energy flux and the discrete aurora accounted for only 20%. At solar minimum, on the other hand, the two energy fluxes were equal. The principal solar cycle difference in auroral energy fluxes was that the mantle auroral energy flux was lower by a factor of four at solar minimum than it was at solar maximum. Energy flux in the discrete aurora on the other hand was the same at solar minimum as it had been at solar maximum although the spatial distributions at solar minimum were narrower and more contracted toward the pole.

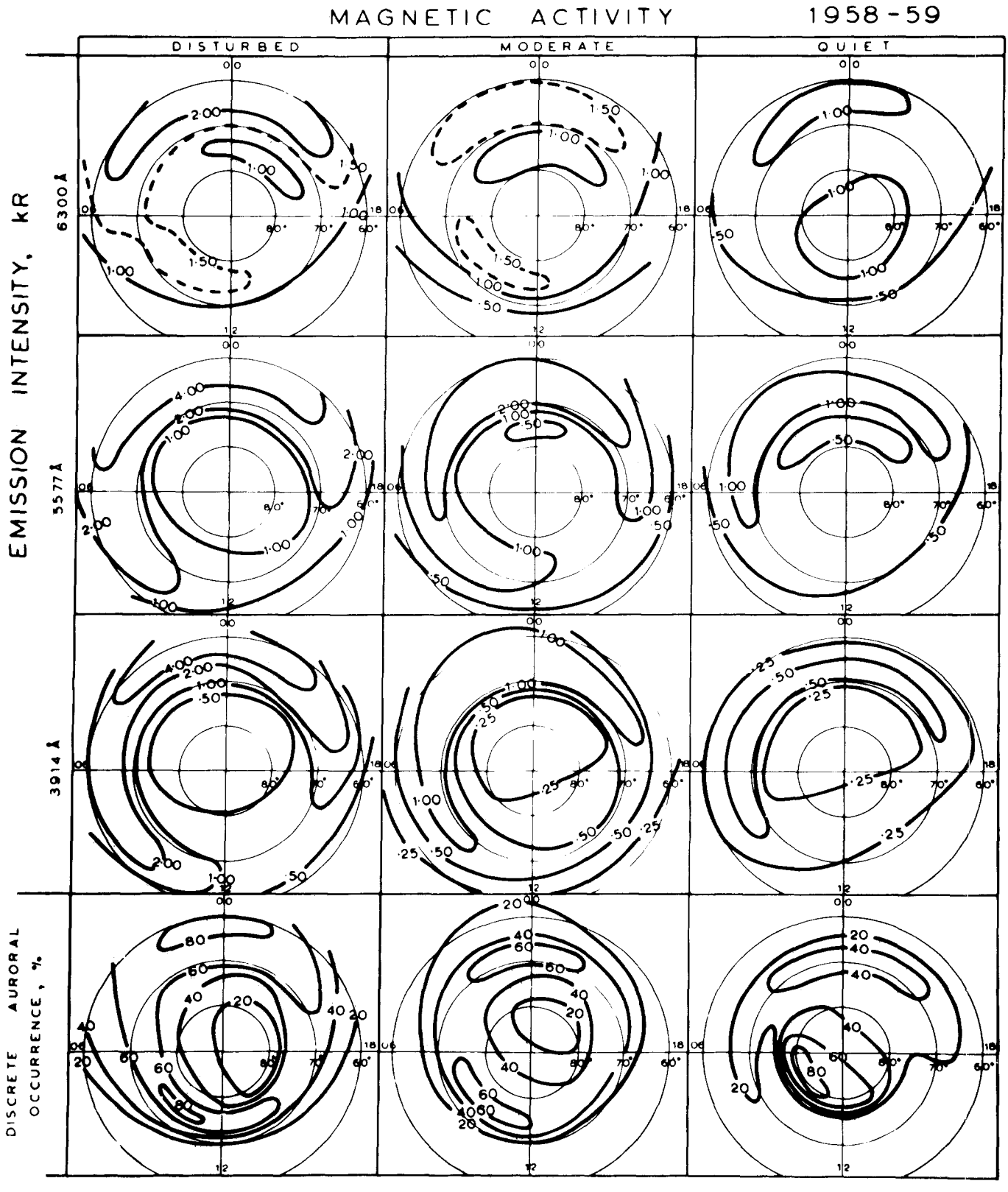

Figure 12-8. Contours of occurrence of discrete aurora (in percent) and average intensity of auroral emissions (in kilo-Rayleighs) for 3 levels of activity from Southern Hemisphere measurements in years 1958–1959. Coordinates are CG latitude and CG local time. [Sanford, 1968] (Reprinted with permission from Pergamon Press, Ltd. © 1968.)

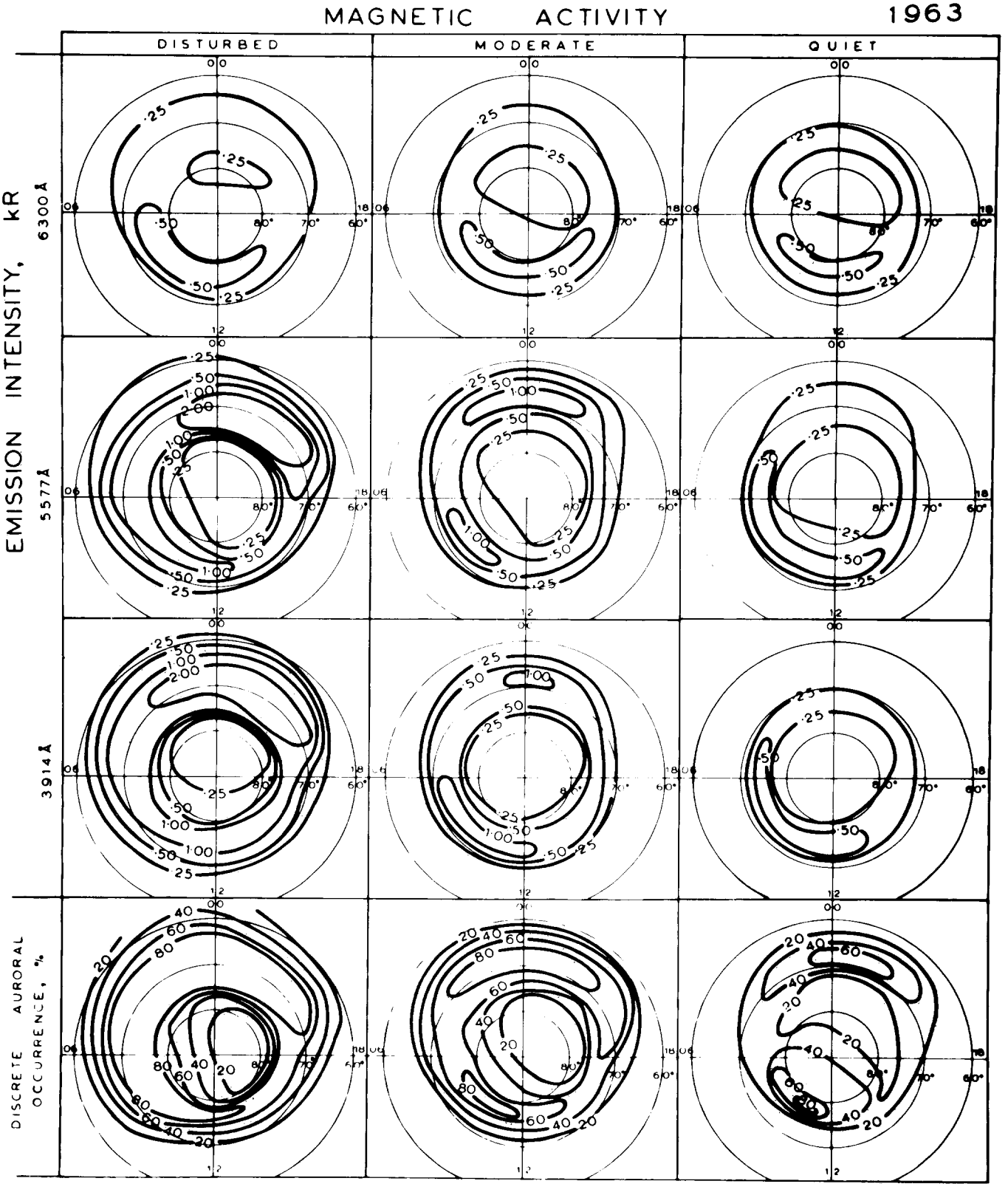

Figure 12-9. Contours of occurrence of discrete aurora (in percent) and average intensity of auroral emissions (in kilo-Rayleighs) for 3 levels of activity from Southern Hemisphere measurements in 1963. Coordinates are CG latitude and CG local time. [Sanford, 1968] (Reprinted with permission from Pergamon Press Ltd. © 1968.)

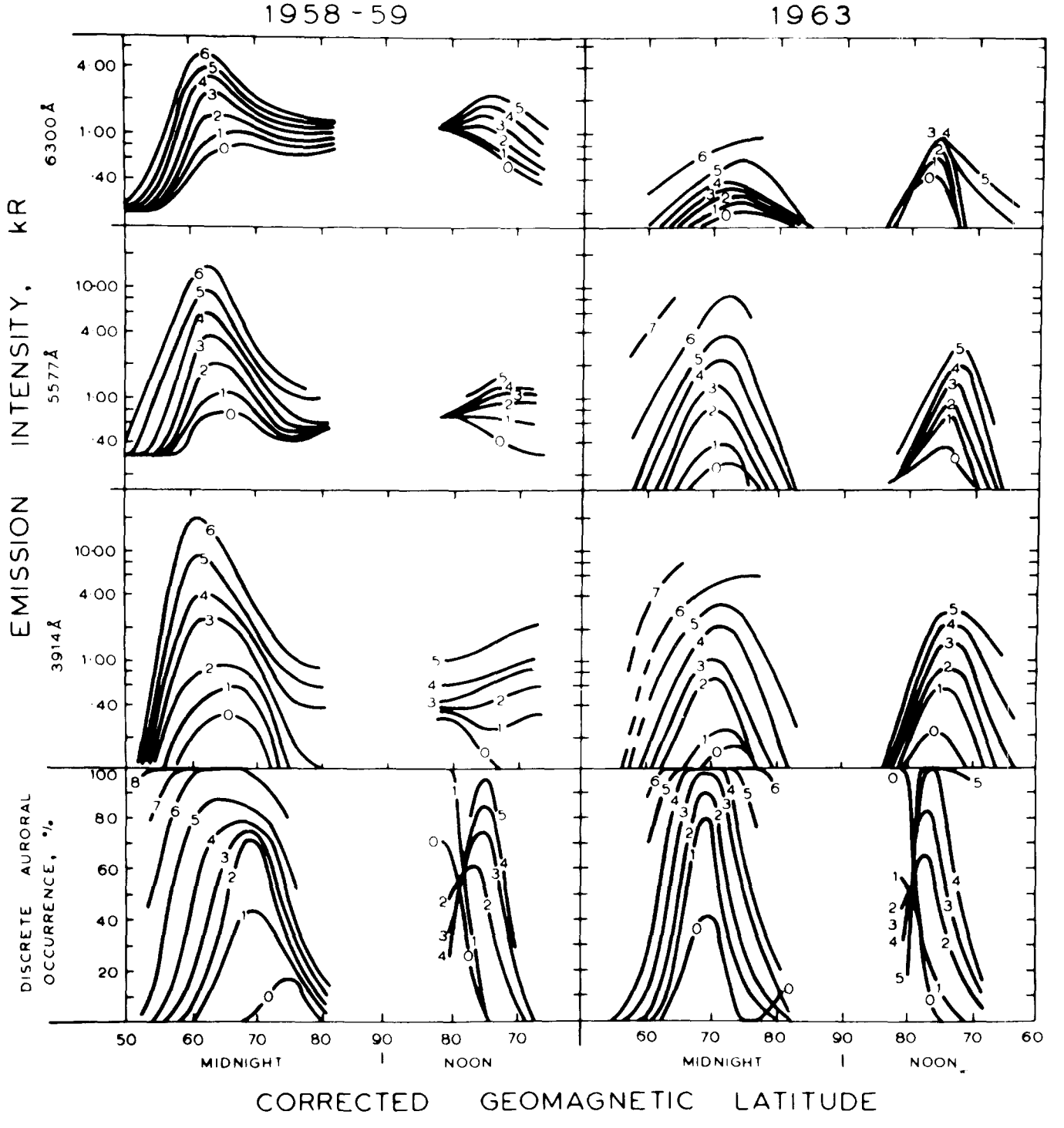

Figure 12-10. The percentage occurrence of discrete aurora and the median intensities of 3914, 5577 and 6300 Å emissions as a function of local K-index and CG latitude along the noon-midnight CG time meridian for the years 1958–1959 and 1963. [Sanford, 1968] (Reprinted with permission from Pergamon Press Ltd. © 1968.)

Other examples of distributions of average parameters will be shown in Figure 12-11.

Equatorward Boundaries—The equatorward boundary of precipitating electrons measured by DMSP satellites has been related to magnetic index Kp via

$$\Lambda_{eq} = \Lambda_0 + \alpha Kp \qquad (12.2)$$

where Λ_{eq} is the CG latitude of this equatorward boundary, Λ_0 is the latitude at Kp = 0 and α is the straight line slope [Gussenhoven et al., 1983]. Values of these parameters are

Table 12-1. Parameter values measured by DMSP satellites.

		$\Lambda = \Lambda_0 + \alpha Kp$		
MLT	Number*	Λ_0	α	CC†
0000–0100	312	66.1	−1.99	−0.80
0100–0200	220	65.1	−1.55	−0.68
0400–0500	267	67.7	−1.48	−0.57
0500–0600	1123	67.8	−1.87	−0.71
0600–0700	2462	68.2	−1.90	−0.74
0700–0800	3159	68.9	−1.91	−0.76
0800–0900	2159	69.3	−1.87	−0.73
0900–1000	1178	69.5	−1.69	−0.66
1000–1100	864	69.5	−1.41	−0.57
1100–1200	513	70.1	−1.25	−0.52
1200–1300	353	69.4	−0.84	−0.35
1500–1600	63	70.9	−0.81	−0.34
1600–1700	204	71.6	−1.28	−0.66
1700–1800	526	71.1	−1.31	−0.69
1800–1900	997	71.2	−1.74	−0.82
1900–2000	2469	70.4	−1.83	−0.82
2000–2100	3309	69.4	−1.89	−0.82
2100–2200	3092	68.6	−1.86	−0.79
2200–2300	1482	67.9	−1.78	−0.77
2300–2400	461	67.8	−2.07	−0.81

*Number of boundaries.
†Correlation coefficient.

given in Table 12-1. This relation is plotted for the 2300–2400 MLT sector in Figure 12-12 where the points are mean values and the error bars are standard deviations. Also shown in this figure are the midnight sector boundaries determined by the following means: (1) ASCA [Feldstein and Starkov, 1967], (2) DMSP Images [Sheehan and Carovillano, 1978], and (3) 6300 Å at 100 R [Slater et al., 1980]. The trend in all four cases is that latitude decreases with increasing Kp. However, there is considerable scatter which is due primarily to the fact that Kp encompasses a large range of auroral conditions [Feldstein and Starkov, 1967]. An additional uncertainty can arise in particle data since the electrons are measured at a single pitch angle and pitch angle distributions can depart appreciably from isotropy [for example, Sharber, 1981].

This boundary has been found to be solar cycle dependent as noted earlier in relation to the auroral oval. In addition it has been reported to vary by several degrees as a function of UT, being at highest latitude near 0600 UT and lowest latitude near 1800 UT [Sheehan and Carovillano, 1978; Meng, 1979; Whalen, 1983].

Finally the instantaneous distribution of energy flux typically has a gradient with latitude that makes the location of an equatorward boundary a function of detector threshold. Strickland et al. [1983] show a case where a sensitive detector would place the apparent edge as much as 4° equatorward of that determined by a less sensitive detector. For statistical distributions the situation is worse judging by the 3914Å distributions of Sandford [1968] shown in Figure 12-10 (right).

Offset Pole Coordinates—A number of auroral phenomena have been found to be ordered by a coordinate system that lies within the frame of reference of magnetic latitude—magnetic local time but has an effective pole offset from the magnetic pole. This offset pole lies near the midnight meridian and has a colatitude near 4°.

The auroral oval was noted earlier as having an equatorward boundary which is such an offset circle. The Q = 2 oval is shown in Figure 12-11a together with a circle whose circumference is defined by the small circular points and whose center is the circled cross. As noted earlier, this is better approximated by an analytical expression then by a circle.

Three other examples are shown in Figure 12-11 (b) average intensity of auroral emissions at 3914 Å determined by Sandford [1968] for IGY, (c) blanketing frequencies, fbEs, of the ionized auroral E layer determined by Besprozvannaya and Shchuka [1976] for Kp 0 and 1 in IGY, and (d) average precipitating electron energy flux measured by satellites AE-C and AE-D in years 1974–1976 for AE $\leq$ 100 γ [Spiro et al., 1982].

That the offset pole reference frame is not an artifact of the statistical averaging process is indicated by the existence of auroral arcs seen nearly instantaneously (within approximately 10 min). Meng et al. [1977] have found a group of about 50 quiet auroral arcs imaged by DMSP satellites which are offset circles. These arcs extend continuously over 12 hours of magnetic local time and occur at all local times. Average radius of the arcs was 19° ± 5°. Average offset pole location was 85.8° CG latitude, 00:15 h CG local time.

12.1.2.2 Instantaneous Distributions. Recently progress has been made in quantitatively formulating the instantaneous distribution of the energy flux in the continuous aurora throughout much of its entire latitude-local time extent. This occurred in an 8-hour case study in which this energy flux was found to be constant instantaneously along contours that were defined analytically and approximated by offset circles. Changes that took place did so simultaneously (within 15 minutes time resolution) throughout local time, the extent of which was from evening through midnight to noon [Whalen, 1983].

The latitudinal distribution was therefore the same instantaneously at all local times within the observed extent. Two distributions were defined, the principal one being Gaussian. Furthermore, the Gaussian scale factor was constant in all 32 consecutive determinations. Therefore, the dynamics of the entire nearly global distribution could be described by the variation of only two parameters, the Gaussian maximum energy flux and its offset pole latitude. These

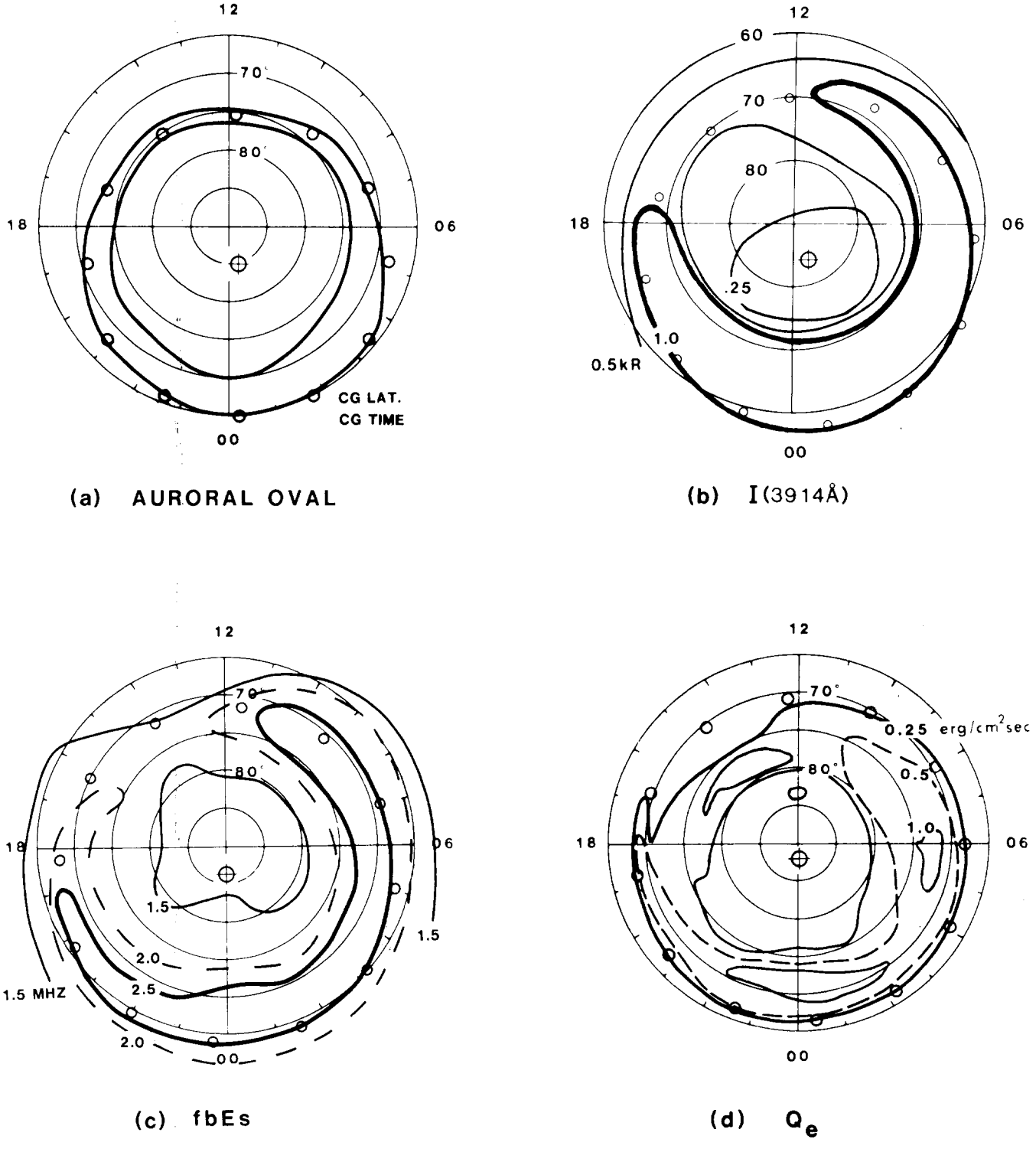

Figure 12-11. Examples of iso-energy flux contours of the continuous aurora which are approximately circles about a pole offset from the CG pole. Circumference of each offset circle is defined by the 12 small circular points, and the offset pole, by the circled cross. (a) The auroral oval for magnetic index Q = 2 [Feldstein and Starkov, 1967]. (b) Median intensity of 3914 Å auroral emissions for IGY [Sandford, 1967]. (c) Auroral E ionization measured by median values of fbEs for Kp of 0 and 1 for 1958 [Besprozvonnaya and Shchuka, 1976]. (d) Average precipitating electron energy flux for AE ≤ 100 for 1974–1976 [Spiro et al., 1982].

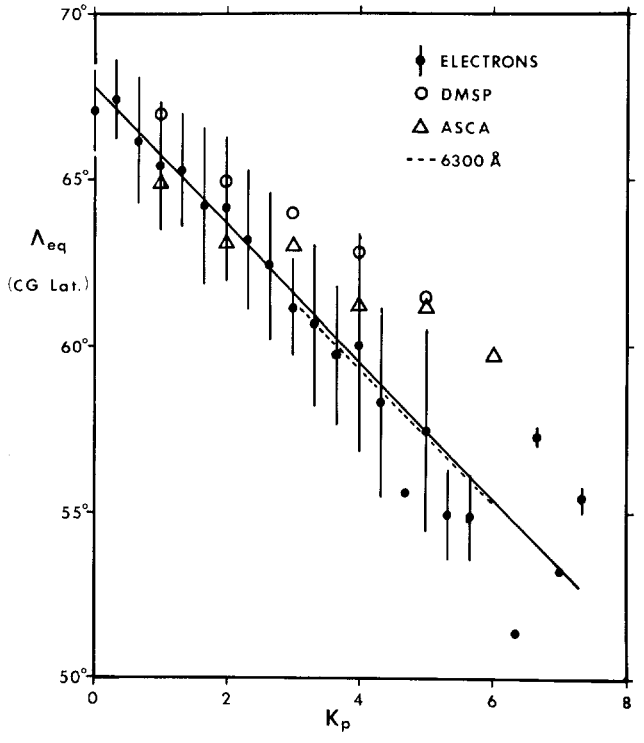

Figure 12-12. Examples of auroral equatorward boundaries near midnight. Electrons: Precipitating electrons [Gussenhoven et al., 1983] ASCA: All-sky camera photographs [Feldstein and Starkov, 1967] DMSP: DMSP images [Sheehan and Carovillano, 1978] 6300 Å: Photometer [Slater et al., 1980]. Error bars indicate standard deviations for the precipitating electrons but are also comparable for the other measurements.

parameters are therefore global indices of this aurora expressing independently the location and intensity of this aurora.

A second latitudinal distribution was found at higher latitude. Gaussian and high latitude distributions corresponded to the regions of particle precipitation named Central Plasma Sheet and Boundary Plasma Sheet by Winningham [1975]. The distributions in magnetic latitude and local time are shown schematically in Figure 12-13.

These distributions have additional significance in that the latitude of the Gaussian maximum, Γmax, is at or near the interface between positive and negative field aligned currents [Robinson et al., 1982]. In addition, Γmax is the equatorward limit of discrete auroras for a large range of conditions [Lui et al., 1977; Whalen, 1983]. Thus the Meng et al. [1977] auroral circles apparently also locate Γmax. Finally, Heelis et al. [1980] find the convection reversal region near the CPS-BPS boundary.

The latitudinal coordinates used in this case study are those approximated by the offset pole at 85.8° CG latitude and 00:00 hr CG time. This pole is determined from the ionospheric data of Besprozvannaya and Shchuka [1976] (Figure 12-11c), and is also very close to the average value which Meng et al. [1977] determined from the DMSP images (85.8°CG latitude, 00:15 h CG time). Although named the offset pole coordinate system, the formulation is an analytical expression similar to that found by Starkov [1969] [Equation (12.1)] for the low latitude boundary of the auroral oval to which the offset circles themselves are approximations. In this formulation the latitude Γ of a point on the earth is given by

$$\Gamma = \Lambda_{CG} + \Theta p \cos \frac{2\pi}{24} (UT - UT_{MN}) \quad (12.3)$$

where Λ_{CG} is the average latitude and has the value of the CG latitude of the point, Θp is the amplitude of the latitudinal variation and has the value of the CG colatitude of the offset pole (4.2° here), UT is universal time and UT_{MN} is the universal time corresponding to CG local midnight for the point considered. During this case study, contours of equal latitude Γ calculated by this expression were measured to be contours of equal energy flux Q, which were accurate to within 0.4° over the CG local time extent of 10 hours.

The function that describes the distribution of energy flux, Q, in offset pole latitudes Γ is

$$Q(\Gamma) = Qmax \exp\left[-1/2\left(\frac{\Gamma - \Gamma max}{\sigma}\right)^2\right] \quad (12.4)$$

where Qmax and Γ max define the peak value as shown in Figure 12-13.

The Gaussian scale parameter σ has been found to have a typical value of 1.4° (3.2°FWHM) and extremes of 1.2° and 2.0° [Whalen, 1981, 1983]. The maximum energy flux Qmax has a typical value of 1 erg $cm^{-2}s^{-1}$ and extremes of 0.25 to 12 erg $cm^{-2}s^{-1}$ [Omholt, 1955; Hilliard and Shepherd, 1966; Whalen, 1981, 1983].

The latitude of the Gaussian maximum, Γmax, has a median vlaue of 71° and extremes of 64° to 74° [Whalen 1981, 1983]. The circular auroral arcs of Meng et al. [1977] had an average latitude of 71° ± 5°, which is consistent with their being interface arcs [Robinson et al., 1982] at or near Γmax.

The spectrum of precipitated (that is, loss cone integrated) electrons in the Gaussian/CPS region is Maxwellian, so that the differential number flux (in electrons $cm^{-2}s^{-1}$ keV^{-1}) is

$$\phi(E) = \frac{Q}{2 E_M^3} E \exp\left(\frac{-E}{E_M}\right), \quad (12.5)$$

where E is electron kinetic energy and E_M the characteristic energy.

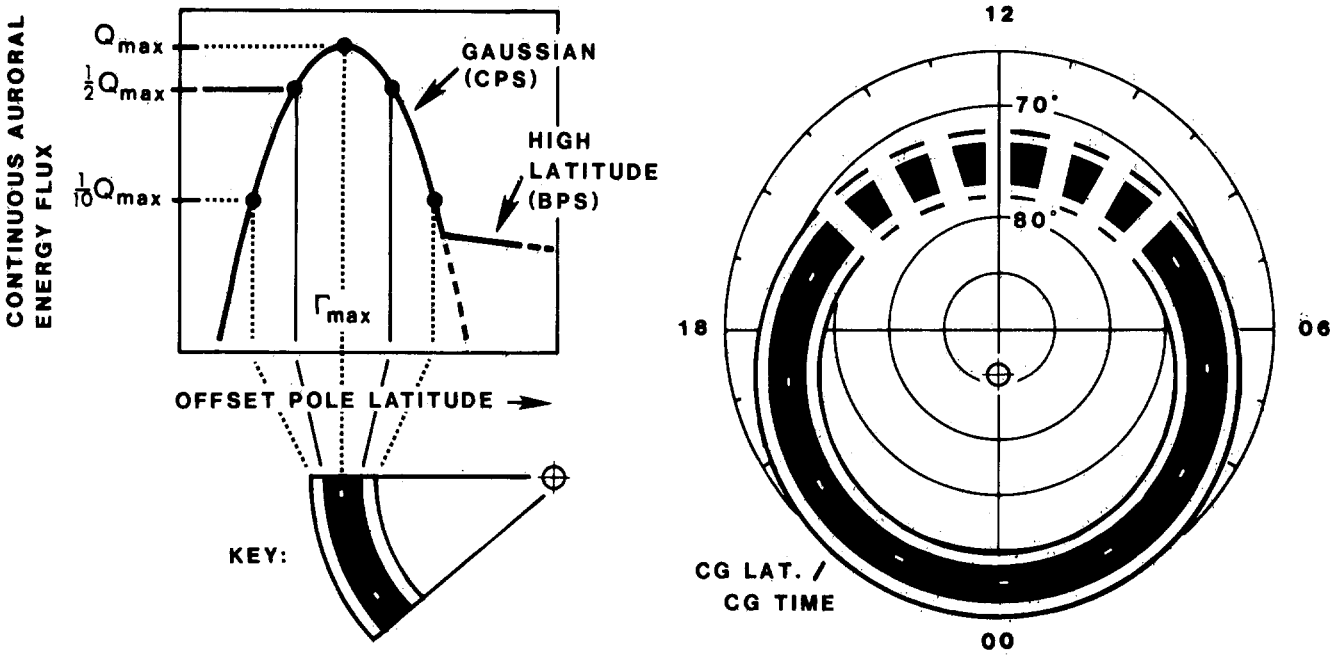

Figure 12-13. Schematic diagrams illustrating the instantaneous distribution of energy flux in the continuous aurora as described in the text. *Left*: Energy flux, Q, as a function of offset pole latitude, Γ, showing the Gaussian/CPS and high latitude/BPS distributions. *Right*: Contours of constant energy flux approximated as circles centered at the offset pole (the circled cross) in CG latitude and CG local time. The offset pole latitudinal distribution, which is therefore the same at all local times except for a region in the day sector, is the Gaussian/CPS distribution shown at the left. The contour of the Gaussian maximum energy flux, Q_{max}, as well as the contours of 1/2 Q_{max} and 1/10 Q_{max} are identified via the sector marked "Key" in the lower left. The dashed contours in the day sector indicate the approximate region in which statistical studies find energy fluxes to be lower than at other local times.

E_M has been found near midnight also to be Gaussian in latitude with a scale parameter close to that of Q.

$E_M$max has been measured at 1 keV [Sharber, 1981]. Inferring particle energies from the production heights measured by Hunten et al. [1963] for this aurora (which they termed diffuse surfaces), $E_M$max was generally between 0.4 and 1.5 keV with extremes of 0.3 and 9 keV. The dependence of $E_M$max on local time however has not been established.

Because of the equivalence of the particle, optical, and ionospheric parameters for the continuous aurora and auroral E-layer (as described in Section 12.1.3.2 and Figure 12-19) the following is true: contours of equal loss-cone integrated electron energy flux Q_e are also contours of equal column integrated N_2^+ emission at 3914 Å, I(3914 Å), as well as contours of equal $foEa^4$, where foEa is the auroral E layer critical frequency. Furthermore, because these three parameters are proportional to one another, for a Gaussian latitudinal distribution, the three have the same Gaussian scale parameter.

Contours of equal $foEa^4$ are also contours of equal maximum electron density, Ne_{max}, as well as contours of equal foEa. However, for a Gaussian latitudinal distribution, the scale parameters are related by the following multiple proportionality:

$$\sigma\,(foEa^4):\ \sigma\,(Ne_{max}):\ \sigma\,(foEa) = 1:\sqrt{2}:2. \quad (12.6)$$

12.1.3 Empirical and Model Relationships

12.1.3.1 Auroral-Ionospheric Profiles. This section describes the ionospheric effects of auroral particle precipitation calculated by a number of workers. The effects of continuous and discrete electron auroras are presented as well as those of proton auroras. In general, isotropic pitch angle distribution of particles is assumed. Other distributions have been studied as well as energy spectra that are different from those assumed here [for example, Rees, 1963].

Continuous Aurora—The electron spectrum of the continuous aurora has been found to be Maxwellian. Sharber [1981] has found good agreement between precipitating electrons fluxes and their simultaneously measured ionospheric E-layer effects provided the particles are integrated over the actual loss cone and averaged over intervals of time and space appropriate to the response of the ionosphere itself and of the characteristics of the ionospheric measurements. The energy spectrum which results from this procedure is well represented by a Maxwellian function.

The Maxwellian differential electron number flux as a function of energy has the form

$$\phi(E) = \frac{Q_M}{2E_M^3} E \exp\left(\frac{-E}{E_M}\right) \text{ electrons cm}^{-2}\text{s}^{-1}\text{eV}^{-1}, \quad (12.7)$$

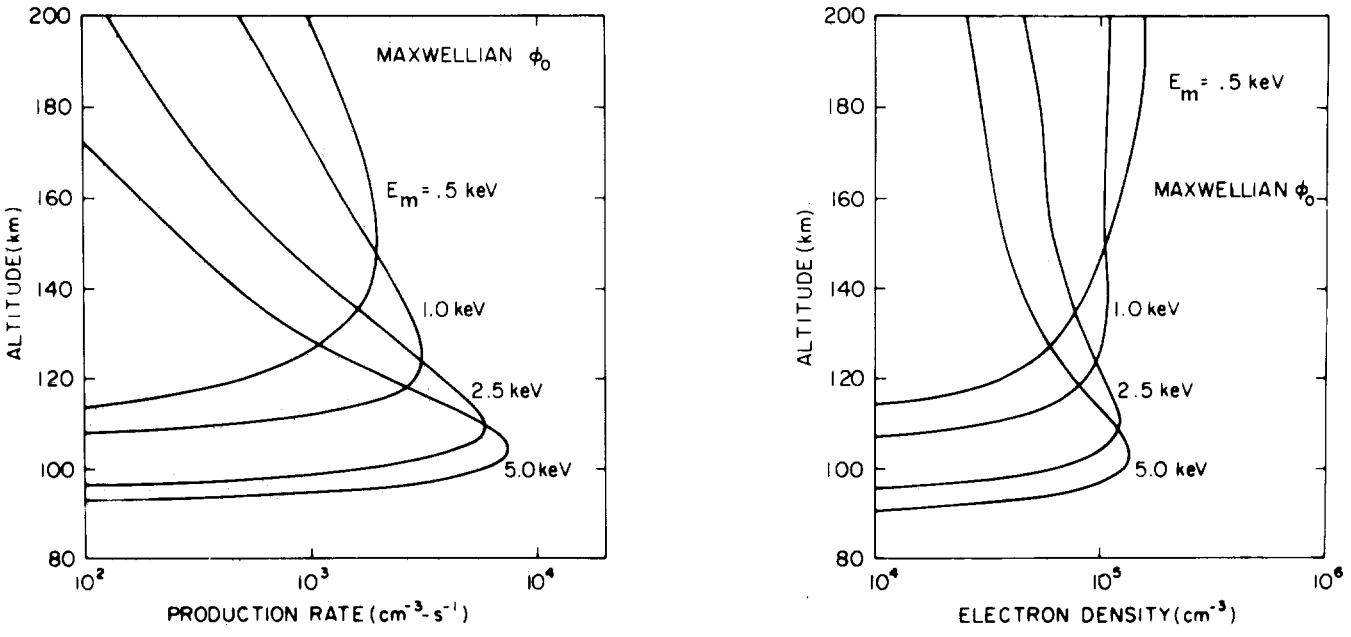

Figure 12-14. Altitude profiles of ion production rates (left) and electron densities (right) resulting from electron precipitation which produces the continuous aurora. Calculations [Strickland et al., 1983] assume Maxwellian spectra, isotropic incidence and energy flux of 1 erg $cm^{-2}s^{-1}$. Curves for 4 values of Maxwellian characteristic energy, E_M, are shown.

where energy E is in eV, energy flux Q_M is in eV $cm^{-2}s^{-1}$ and E_M is the characteristic energy (or temperature).

Since the average energy for the Maxwellian is $2E_M$, the total integral number flux, N_m (electrons $cm^{-2}s^{-1}$) is given by $N_M = Q_M/2E_M$.

Other useful relations can be derived from $N_M = eE_M\phi(E_M)$ where $\phi(E_M)$ is the maximum value of $\phi(E)$.

Altitude profiles of the rates of ion-electron pair production per unit volume resulting from this Maxwellian spectrum have been calculated by Strickland et al. [1983] for four values of E_M and are shown in Figure 12-14 (left). An energy flux of Q_M = 1 erg $cm^{-2}s^{-1}$ has been assumed; profiles for other values of Q_M can be determined from those shown since ionization rate is proportional to Q_M. In addition these profiles can be converted to energy deposition per cm^3 by multiplying the ion production rate by the factor 34 eV per ion pair.

The electron density profiles resulting from these production profiles have been calculated by Strickland et al. [1983] and appear in Figure 12-14 (right). In these calculations equilibrium conditions have been assumed since they are appropriate to the slowly varying nature of this aurora and the E-region.

A plot of the altitude of the peak ionization rate as a function of characteristic energy is shown in Figure 12-15 displaying the agreement in the results of several workers.

Discrete Aurora—The electron spectra that produce the discrete aurora have been modeled by either monoenergetic or Gaussian spectra. Although the actual spectra are more accurately modeled by a Maxwellian spectrum that has been accelerated through a fixed potential, the Gaussian is an adequate approximation for the calculation of the ionospheric response.

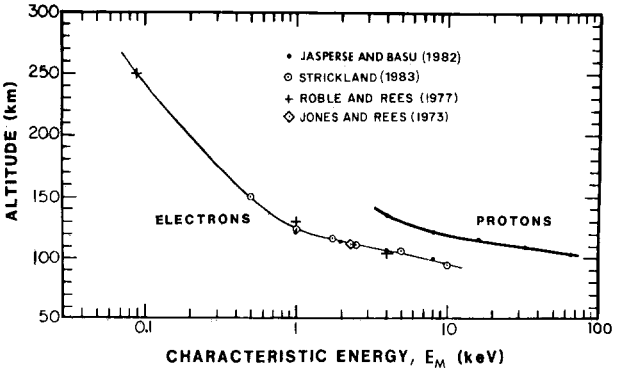

Figure 12-15. Altitude for the maximum ion production rate versus Maxwellian characteristic energy for ionization resulting from the precipitation of particles with Maxwellian spectra and at isotropic incidence.
Left: Electrons which produce the continuous aurora.
Right: Protons.

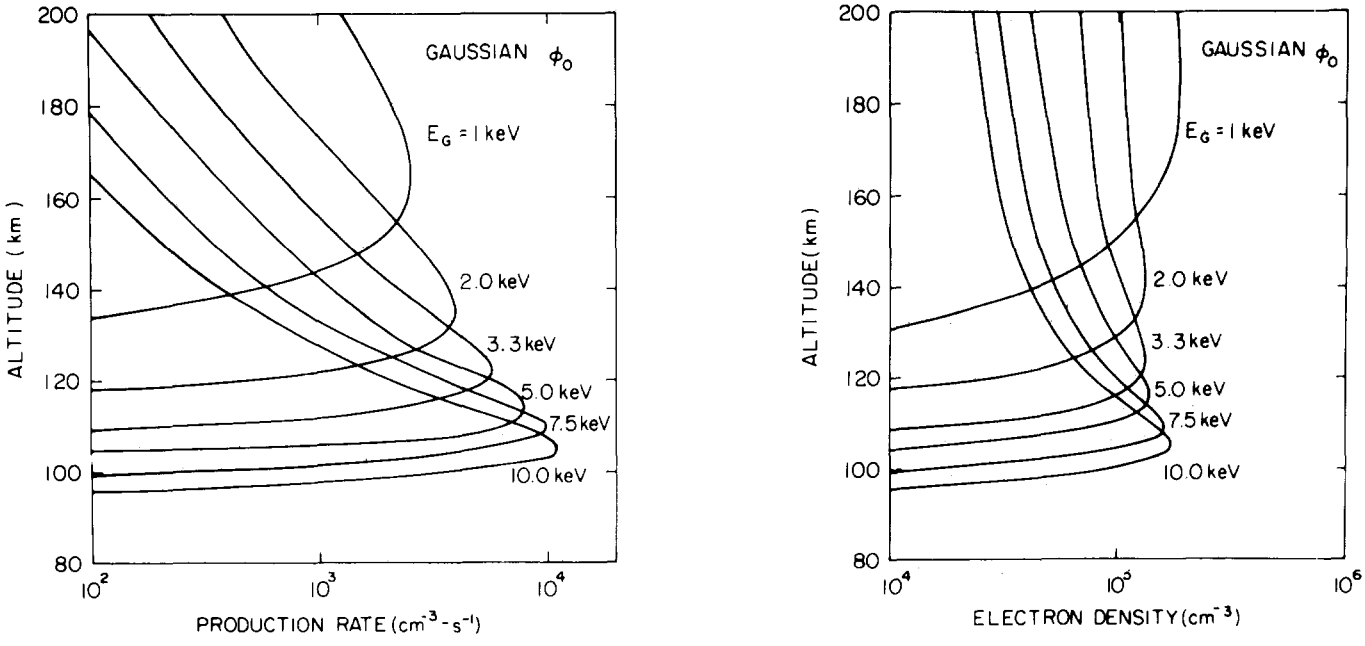

ELECTRON PRECIPITATION

GAUSSIAN SPECTRA (DISCRETE AURORA)

Figure 12-16. Altitude profiles of ion production rates (left) and electron densities (right) resulting from electron precipitation which produces the discrete aurora. Calculations [Strickland et al., 1983] assume Gaussian spectra, isotropic incidence and energy flux of 1 erg $cm^{-2}s^{-1}$. Curves are shown for 6 values of Gaussian maximum energy, E_G.

The representation of the discrete differential number flux is

$$\phi(E) = \frac{Q_G}{\pi^{1/2}\sigma E_G} \exp\left[-\left(\frac{E - E_G}{\sigma}\right)^2 \right] \text{electrons cm}^{-2}\text{s}^{-1}\text{eV}^{-1} \qquad (12.8)$$

where E_G is the maximum energy in eV. The Gaussian scale parameter σ has values near 0.2 E_G.

Altitude profiles of ionization rates for values of E_G and for Q_G = 1 erg $cm^{-2}s^{-1}$ appear in Figure 12-16 left and the resulting electron density profiles are shown in Figure 12-16 right [Strickland et al., 1983]. Again electron density has been calculated assuming equilibrium and so applies specifically to auroras that are constant in all respects for periods greater than about 1 min. For auroras that are more transitory, these electron density profiles can be considered to be upper limits.

The altitude of maximum ionization rate (points) and the altitudes at which the rate has fallen to 10% of maximum (bars) is shown in Figure 12-17 for the case of monoenergetic electrons of isotropic incidence [Rees, 1964].

Proton Aurora—Proton spectra have been found to be consistent with Maxwellian spectra [for example, Sharber, 1981]. Ionization rate profiles for precipitating protons with Maxwellian spectra have been calculated by Jasperse and Basu [1982] assuming isotropic incidence. Figure 12-18 shows a profile for each of five values of characteristic energy, E_M for energy flux of 1.0 erg $cm^{-2}s^{-1}$. A plot of the altitude of the peak ionization rate as a function of characteristic energy is shown in Figure 12-15.

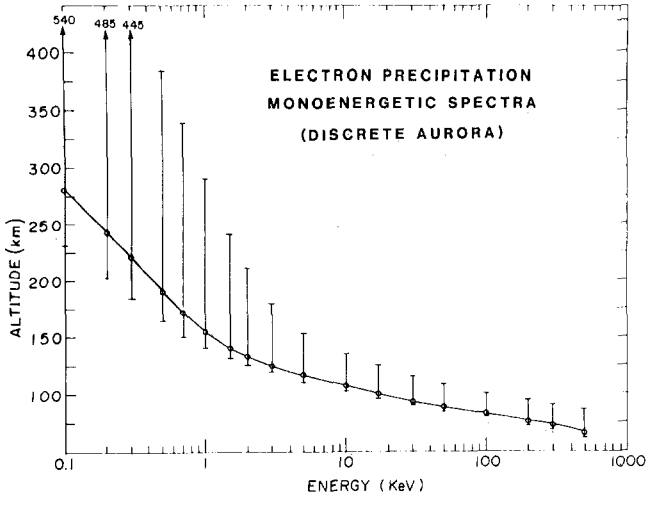

Figure 12-17. Altitude of the maximum ionization rate (points) and the altitudes at which this rate has fallen to 10% of the maximum (bars) versus energy, for ionization produced by electrons which form the discrete aurora as modeled by monoenergetic spectra of isotropic incidence [Rees 1964].

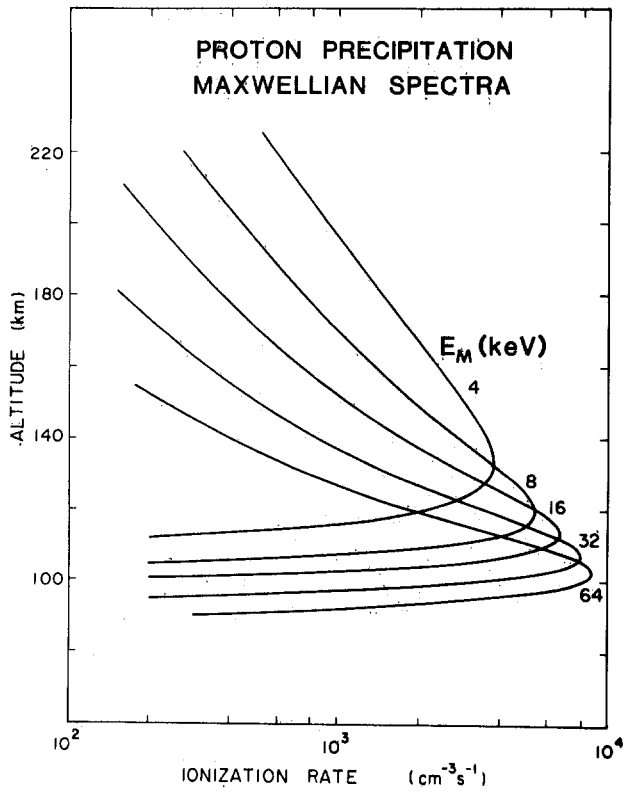

Figure 12-18. Altitude profiles of ion production rates resulting from precipitation of protons of isotropic incidence and Maxwellian spectra of characteristic energy E_M. Energy flux is 1.0 erg $cm^{-2}s^{-1}$ [Jasperse and Basu, 1982].

12.1.3.2 Relations Between Auroral Electron, Optical, and Ionospheric Parameters. Auroral studies are conducted in three major disciplines: particle, optical and ionospheric. Under some conditions parameters in all three are closely enough related so that a measurement in one discipline permits inference of parameters in the other two. This section presents a graph interrelating these parameters in a convenient form as well as a description of the conditions under which these relations apply.

The parameters plotted in columns in Figure 12-19 are as follows:

IBC—The International Brightness Coefficient, a semi-quantitative index for visible auroras.

Q—Energy flux in erg $cm^{-2}s^{-1}$ of precipitated electrons. These are loss cone integrated and subject to the space and time constraints described in Section 12.1.3.1.

I(3914Å)—Column integrated intensity of the N_2^+ emission band at 3914 Å produced by auroral particle precipitation.

The above relationships are well established [Dalgarno et al., 1965] and apply in the E-region to both discrete and continuous auroras. In addition, the relation between Q and I(3914 Å) is correct for the D-region although IBC is not defined there.

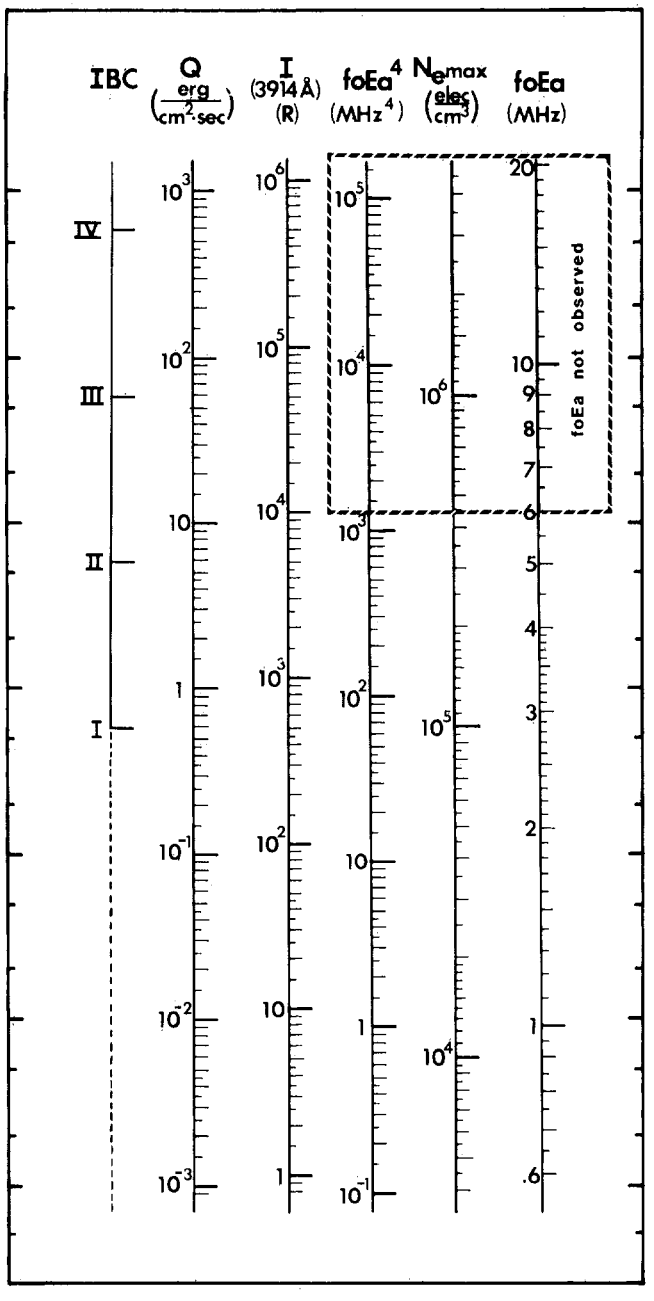

Figure 12-19. Inter-relations of particle, optical and ionospheric parameters for the continuous aurora and auroral E layer.
IBC: International Brightness Coefficient.
Q: Energy flux of precipitating auroral electrons.
I(3913 Å): Column integrated intensity of the N_2^+ emission band at 3914 Å.
$foEa^4$: Fourth power of auroral E layer critical frequency for the ordinary ray.
Ne_{max}: Electron density of the auroral E layer at its maximum in altitude.

The ionospheric parameters obey these quantitative relations only for the auroral E layer, which is produced by the continuous (or diffuse) auroral precipitation. This layer is extensive, highly uniform and is in equilibrium. foEa, the critical frequency of the ordinary ray measured by the

ionospheric sounder, is the maximum plasma frequency of the E-layer and has been related empirically to both Q and I(3914 Å) via its fourth power, foEa^4 [Omholt, 1955; Sharber, 1981] as shown in column 4.

Ne_{max} is the peak electron density in the auroral E-layer, being derived via $foEa = 8.98 \times 10^3 \sqrt{Ne_{max}}$ where foEa is in Hz and Ne_{max} in electrons per cm^3.

12.1.3.3 Auroral Activity. The discrete aurora on the small scale is frequently very unstable and chaotic. However, certain ordering of brightness and extent has been achieved on the large scale using DMSP auroral images the breadth of which is 2200 km, and airborne ASCA photographs, with a diameter of 900 km. The two data bases represent very different time scales, DMSP images being separated in time by 100 min and the ASCA by 1 min.

Auroral images by the DMSP satellite have been categorized as active, moderate, or quiet as described in Table 12-2 [Sheehan et al., 1982]. The distribution of frequency of occurrence appears in Figures 12-20a, b, c, and d showing the relation of occurrence frequency to magnetic indices Kp and AE and dependence on UT. In Figure 12-20e the columns are headed by activity observed on a given orbit; the rows are the occurrence frequencies observed on the following orbit.

Auroral images have been recorded by ASCA at 1-min intervals aboard an aircraft flying at local midnight for durations of 5–10 h [Krukonis and Whalen, 1980]. This data has permitted analysis of auroral activity over a considerable range of time durations as distinct from the DMSP images, the sampling rate of which is limited by the orbital period.

Twelve flights totaling 93 hours provided 5600 photographs in the midnight sector near 69° (±4°) CG latitude. When mounted in a montage format these photographs revealed individual events of auroral activation with measurable lifetimes. Categorizing the auroras in the above manner produced the histograms of the lifetimes or auroral activity shown in Figure 12-21. The combined A, M, and Q categories indicate a characteristic lifetime of auroral activity near 15 min (Figure 12-22).

Table 12-2. Description of the criteria used to rate auroral activity in DMSP images.

Category	Auroral Morphology	Latitudinal Extent	Longitudinal Extent	Comments
N	No aurora visible in a properly exposed image having adequate auroral zone coverage.			Seldom observed in a good quality image
Q	Quiet auroras consiting of a single, thin, structureless discrete arc or broader band of diffuse aurora [Lui et al., 1973] also called continuous aurora [Pike and Whalen, 1974].	$\lesssim$ 1° CGL (discrete arc)	Up to the entire longitudinal extent of the image ($\approx$ 3–12 hours of local time depending on coordinate orientation)	
M	Moderate state of auroral activity typified by patches, knots, or loops in discrete auroras, including 'westward surges' and bulges along otherwise thin arc structures: also, polar cap arcs extending from oval auroras. Gradations in the moderate range (M−, M, and M+) attempt further refinement, but distinctions are often difficult to make, particularly between M+ and A.	$\lesssim$ 5° CGL	A few hours of magnetic local time, usually not the entire oval	Statistically most common situation
A	Very active auroral conditions with (apparent) large westward surges, poleward bulges, and a broad band of discrete aurora. With linear amplifiers employed in older satellites, bright auroras can saturate and wash out all detail. Newer satellites with logarithmic detectors can distinguish detail over a wide range of intensities.	$\gtrsim$ 5° CGL	The entire longitudinal extent of the oval visible in an image	M+ and A categories often difficult to distinguish

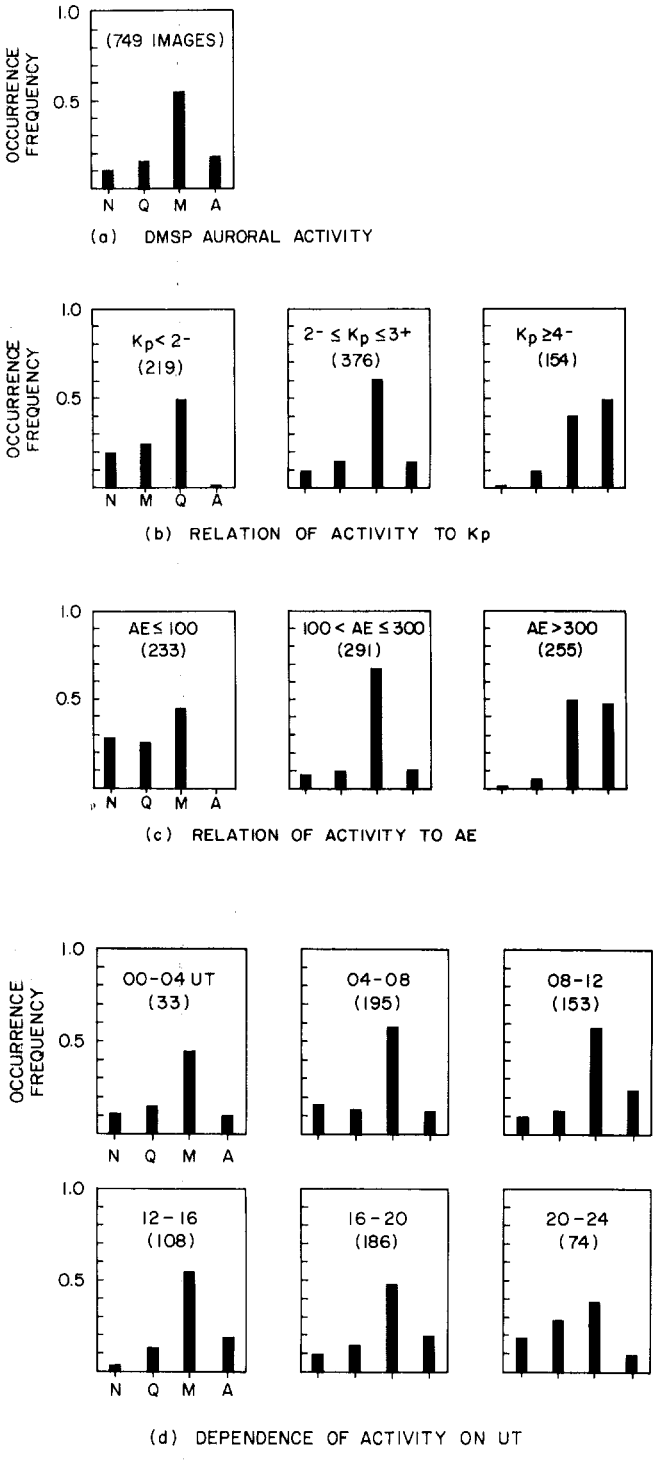

Figure 12-20. Frequency of occurrence of auroral activity observed in the DMSP images in categories of Active, Moderate, Quiet and No visible aurora as defined in Table 12-2 [Sheehan et al., 1982].
a. All cases.
b. Relation to Kp.
c. Relation to AE.
d. Dependence on UT.
e. Recurrence of activity where columns are headed by activity observed on initial orbit; the 3 rows are the distribution of occurrence frequency on the following orbit.

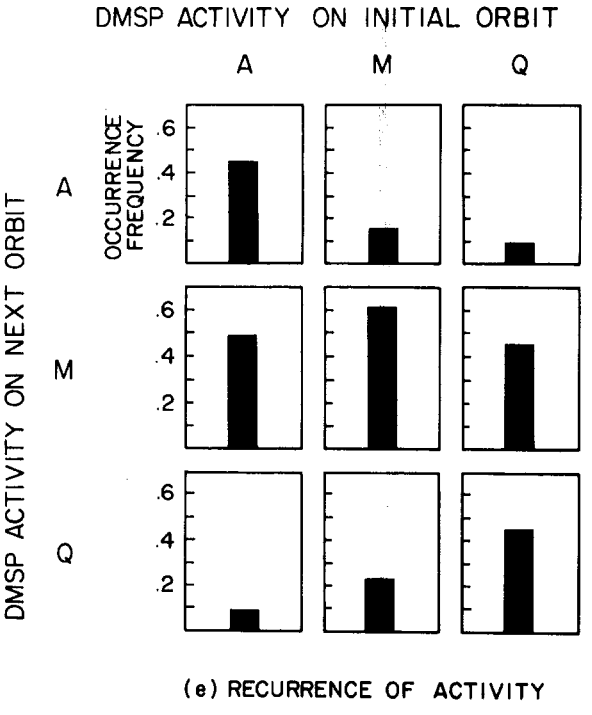

Figure 12-20. (*Continued*)

12.1.3.4 Heights of Discrete Auroras.

Dependence of Heights on Magnetic Latitude and Local Time—The altitude and latitude of peak emission at 5577 Å have been measured for homogeneous arcs by photometers using triangulation methods [Boyd et al., 1971]. The resulting heights versus magnetic latitude are plotted in Fig-

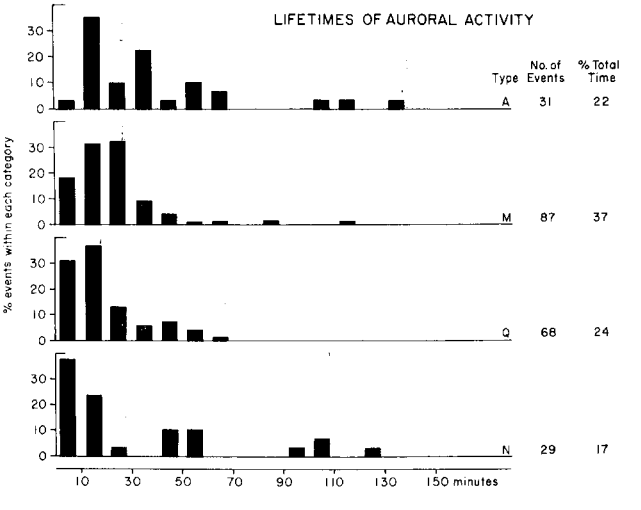

Figure 12-21. Distributions of lifetimes of auroral activity within categories described in Figure 12-20 as determined by airborne all-sky photographs near midnight. Number of events within each category and the percent of the total time represented by each category are listed at the right [Krukonis and Whalen, 1980].

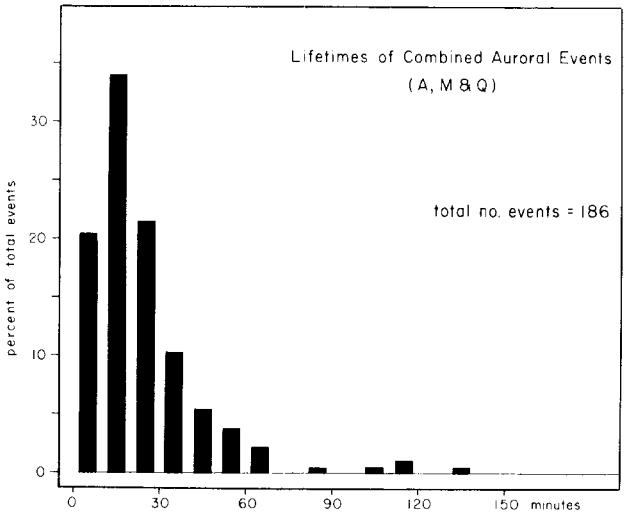

Figure 12-22. Percentage occurrence of lifetime of auroral activity for combined active, moderate and quiet categories (from Figure 12-21) showing Poissonian lifetime of ~15 minutes.

ure 12-23 in four 3-hour intervals of local time encompassing evening through midnight to morning. Heights have been related to the energy at which monoenergetic electrons produce maximum emission via the relations of Rees [1963] and these energies are plotted on the right hand scale.

Two relations are apparent: heights decrease with latitude within each local time interval and heights decrease as local time increases from evening to morning at each latitude where the aurora is observed.

The limitation of this study is that the triangulation technique requires relatively stable arcs, hence the results apply to relatively quiet conditions.

Height-Brightness Relations—A number of workers have reported that discrete auroras increase in brightness with decreasing heights as determined by optical triangulation [for example, Starkov, 1968 and Harang, 1951; Boyd et al., 1971]. Evidence for this effect, which is more quantitative in nature and not as dependent on auroral stability, has resulted from a study of discrete aurora by airborne ionospheric sounder and ASCA during 11 north-south crossings of the auroral oval near midnight [Wagner and Pike, 1972; Gassmann et al., 1972]. Auroral sporadic E echoes recorded by the ionospheric sounder were selected for times when the ASCA films showed aurora to be in the zenith. Virtual height for these echoes, h'Esa, is plotted versus the frequency fEsa in Figure 12-24, together with the qualitative designation of brightness from the ASCA photographs. The trend that brightness increases with decreasing height can be described in a more quantitative way by the approximate translation of frequency to intensity of 3914 Å emission via Figure 12-19. Height can be translated into approximate monoenergetic electron energy via Figure 12-17.

12.2 AURORAL OPTICAL AND INFRARED EMISSIONS

The optical emissions that characterize an aurora are produced by the deposition of energy in the atmosphere by energetic particles, primarily electrons and, in some instances, protons. The energetic particles are derived from

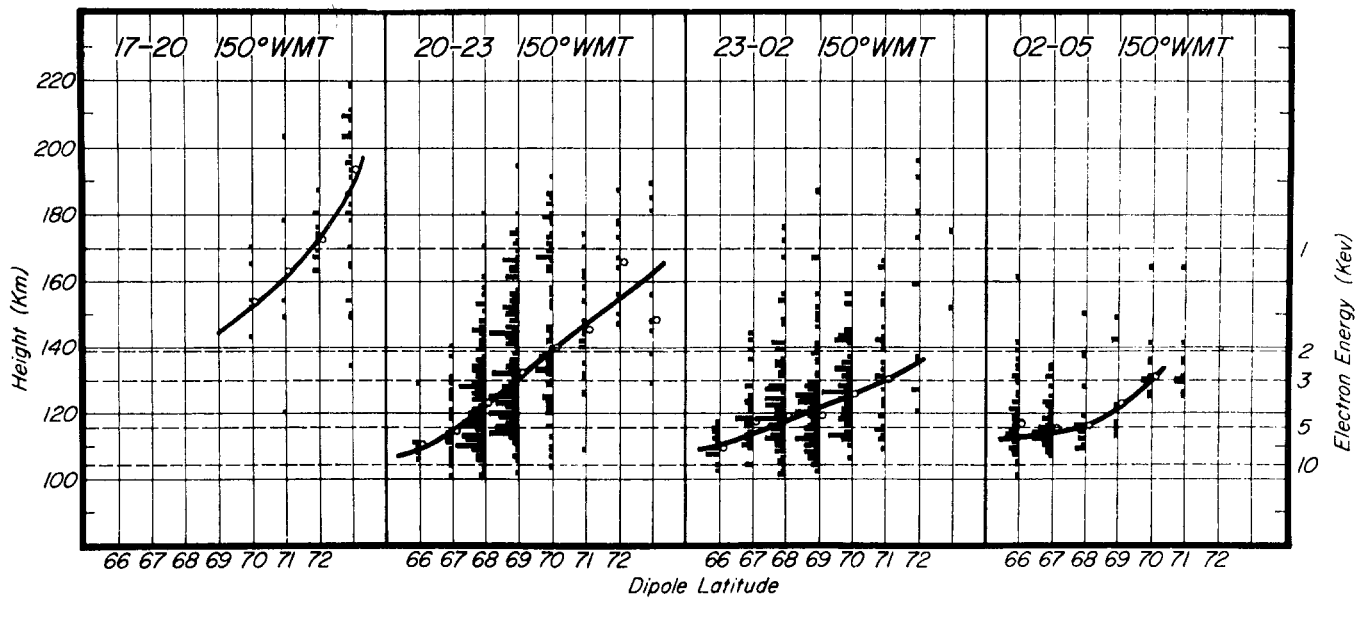

Figure 12-23. Distributions of the height of the peak emission in 5577 Å as a function of dipole latitude for four 3-hour time periods shown as 150°WMT. Local magnetic midnight is approximately 0115 150°WMT. The median point of the distribution in each latitude interval is shown by a circle.

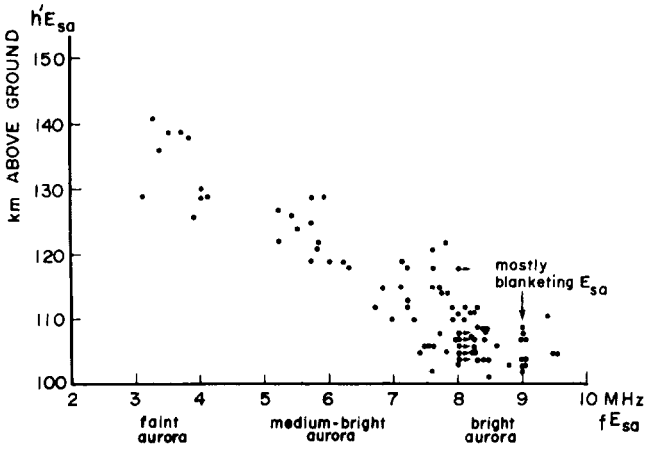

Figure 12-24. Relations between brightness (from airborne ASCA), auroral sporadic E frequency, fEsa, and virtual height of auroral sporadic E layer, h'Esa (from airborne ionospheric sounder) for discrete aurora in the zenith. from 11 latitudinal scans across the oval near midnight by aircraft [Wagner and Pike, 1972].

Figure 12-26. Photo of the earthlimb seen from Skylab 3 looking toward the southern auroral zone. The airglow layer runs in a thin band across the center of the photo, while a bright auroral arc crosses the earthlimb at lower right and ends in the foreground in the middle of the scene [Garriott, 1979]

the interaction of the solar wind, a gaseous plasma continuously streaming from the sun's surface, and the earth's magnetic field [Chapter 8]. The currents of charged particles generated by the energy coupling between the solar wind and the magnetosphere produce energetic electrons surging earthward along geomagnetic field lines in the auroral zone. Collisions of the precipitating energetic auroral particles with the increasingly denser atmospheric neutral atoms and molecules in the 200 to 100 km altitude range produce the luminosity associated with auroras illustrated in Figures 12-25, 12-26, and 12-27. As reviewed in Section 12.1, satellite images of auroral luminosity in the polar regions have contributed significantly to the understanding of the interaction of the solar wind and the magnetosphere, auroral substorms, and the morphology of the diurnal cycle of the auroral ovals surrounding the geomagnetic poles [Akasofu, 1981]. Auroral optical emissions have been examined by instrumentation located in ground-based observatories [Vallance Jones, 1974], research aircraft [E.R. Huppi et al., 1974], rocket probes [Stair et al., 1975; K.D. Baker et al., 1977; Stair et al., 1980; Feldman and Gentieu, 1982], and satellites [Hanson, 1973; Huffman et al., 1980; Frank et al., 1982]. These studies involve measurements of spectral distributions, photon emission rates, and altitude profiles. The data are then analyzed to identify the excited states of

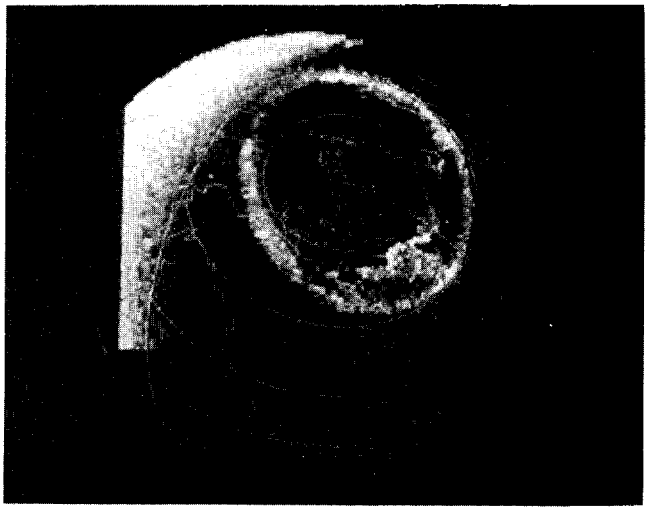

Figure 12-25. View from space of intense auroral emission distributed around entire auroral oval. Image was taken at 0241 UT, 8 Nov 1981, with University of Iowa's ultraviolet auroral imaging instrumentation aboard Dynamic Explorer 1 while orbiting 20 000 km over North America. (Courtesy of L.A. Frank.)

Figure 12-27. Bright auroral arcs recorded from the ground at Poker Flat, Alaska. (Courtesy of A.L. Snyder.)

the radiating atomic and molecular species and to determine their auroral production and loss processes.

Auroral phenomenology, morphology, and occurrence are the subject of Section 12.1. The current section will concentrate on the overall photon emission rates, spectral distributions, and altitude profiles of auroral optical emissions and the identification of the radiating species and their production and loss mechanisms. Particular emphasis will be placed on the infrared portion of the spectrum. Only emissions from aurorally disturbed atmospheres will be discussed; quiescent atmospheric emissions are treated in Chapter 13.

This section begins with a discussion of laboratory studies and their impact on auroral models and continues with a general discussion of emission rates in terms of production and loss mechanisms for auroral species. Processes giving rise to various auroral visible and ultraviolet emissions are discussed, and the section concludes with a discussion of the dominant aurorally enhanced infrared bands, especially the important CO_2 4.3 μm emission and the NO 2.7 μm and 5.3 μm emissions.

12.2.1 Laboratory Studies and Auroral Models

Auroral mechanisms are studied in laboratory experiments involving particle beams incident on atmospheric gases or gas mixtures. Such experiments measure specific parameters that quantify the incident electron energy loss, energy deposition profile, and excited-stated production [Cohn and Caledonia, 1970], as well as the spectral, temporal, and spatial radiative characteristics of the gases. Gas discharges have been used in flowing afterglow experiments [Piper et al., 1981a, b] and chemiluminescent reaction cells [Rawlins et al., 1981b] to determine rate coefficients and photon yields for specific auroral reactions. The laboratory experiments provide an opportunity to study a specific production or loss process for an excited species under controlled conditions of temperature and gas density.

Measured parameters, including cross sections for energy loss by incident electrons and for production of specific new species or excited states [Wadzinski and Jasperse, 1982], have contributed to the generation of a number of auroral models. Such models typically include descriptions of electron energy deposition and excited-state production, usually followed by chemistry codes to describe production of additional species and perhaps by an atmospheric motion code and a radiative transfer code. Descriptions of electron interaction with the ambient atmospheric gas have used a variety of techniques. Simple semi-empirical models of electron energy deposition have been constructed [Rees, 1963] using energy dissipation functions measured in the laboratory. The secondary electron production rate in such models is calculated from the observation that an electron-ion pair is produced for every 34 eV of energy deposited by the primary electron. Once the ionization rates are known, the production rate of secondaries as a function of energy and the secondary electron flux can be calculated [Rees et al., 1969], using analytic or experimental values for secondary electron production cross sections and electron-neutral inelastic cross sections. From the secondary electron flux, excited-state production rates may be deduced. Other descriptions of electron energy deposition and excited-state production have used range-theoretic methods [Stolarski and Green, 1967; Peterson et al., 1973], Monte-Carlo techniques [Berger et al., 1970], and Fokker-Planck [Banks et al., 1974] and Boltzmann [Strickland et al., 1976] transport equation methods. In addition to the above time-independent approaches, recent time-dependent models taking atmospheric motion into account have been formulated [Roble and Rees, 1977].

The models have been tested against the results of field experiments. Advances in instrumentation design and sensor technology have resulted in steady improvement of the precision, spectral resolution, and minimum detectable emission level in the field and laboratory experiments. The resulting improved and expanding data set has broadened the scope and increased the precision of our understanding of auroral processes.

12.2.2 Artificial Auroral Experiments

In recent years, rocketborne electron accelerators have been used in a variety of active experiments in the upper atmosphere [Winckler, 1982], including the investigation of wave-particle interactions, beam-plasma discharge, particle trapping in the geomagnetic field, generation of radio-frequency electromagnetic waves, and artificial auroral experiments (Figure 12-28). A series of artificial auroral experiments using rocketborne electron accelerators has been conducted at AFGL under the EXCEDE program [O'Neil et al., 1978a and b, 1979, 1982]. In artificial auroral ex-

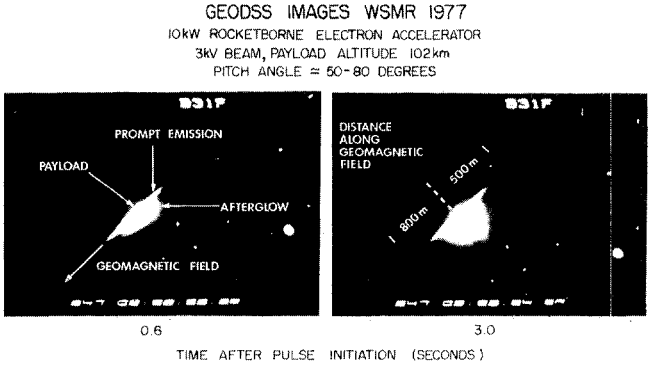

Figure 12-28. Ground-based image of emission from EXCEDE artificial auroral experiment taken through 31-inch GEODSS telescope at White Sands, New Mexico. The prompt emissions and afterglow are shown at two different times after pulse initiation.

periments such as EXCEDE, the dose conditions (primary electron energy, ionization rate, dose time, and dose altitude) are carefully controlled and defined. By contrast, in natural auroras the dose conditions must be inferred from the observations and may be less certain because the effects are integrated over a range of altitudes and dose levels. Consequently, artificial auroral experiments provide a useful adjunct to observations of naturally occurring auroras in the attempt to understand auroral phenomena.

12.2.3 Emission Rates

The kinetic energy of the auroral particles is converted to optical and infrared emissions of discrete wavelengths through processes initiated by inelastic collisions with ambient atmospheric species. These species may spontaneously relax to lower energy states directly while emitting radiation. Alternatively, they may undergo one or more chemical reactions, finally resulting in an excited product which also emits energy by spontaneous radiative decay. The specific auroral processes involved in the production of various excited species continue to be the focus of much aeronomic study. Excellent general reviews of auroral processes are given by Chamberlain [1961], Vallance Jones [1974], and Bates [1982]. The reader is also referred to the textbooks on atmospheric radiation by Goody [1964] and on infrared and optical spectroscopy by Herzberg [1950, 1945, 1967] and Huber and Herzberg [1979].

The intensity of atomic and molecular transitions from upper state u to lower state ℓ is given by the relation

$$I_{u\ell} = N_u A_{u\ell}, \tag{12.9}$$

where $I_{u\ell}$ is the optical intensity in photons $cm^{-3}\ s^{-1}$, N_u is the population of the upper state in molecules cm^{-3}, and $A_{u\ell}$ is the Einstein A coefficient, or radiative transition probability, in s^{-1}. If auroral activity has continued long enough for the production and loss processes of a given state to come to equilibrium, the number of excited molecules per cm^3 at steady state, N_{uss}, is given by

$$N_{uss} = P_u/L_u, \tag{12.10}$$

where P_u is the production rate per unit volume in $cm^{-3}s^{-1}$ and L_u the loss rate in s^{-1}. The loss rate of a given state may be described by the relation

$$L_u = \sum_{\ell} A_{u\ell} + K_{uO_2}[O_2] + K_{uN_2}[N_2] + K_{uO}[O] + \ldots, \tag{12.11}$$

where K_{uM} is the rate coefficient in cm^3s^{-1} molecule^{-1} for collisional deactivation (or quenching) of the excited state by species M.

The production of a given excited state may be the result of electron impact in inelastic collisions of the form

$$e + N \rightarrow N^* + e, \tag{12.12}$$

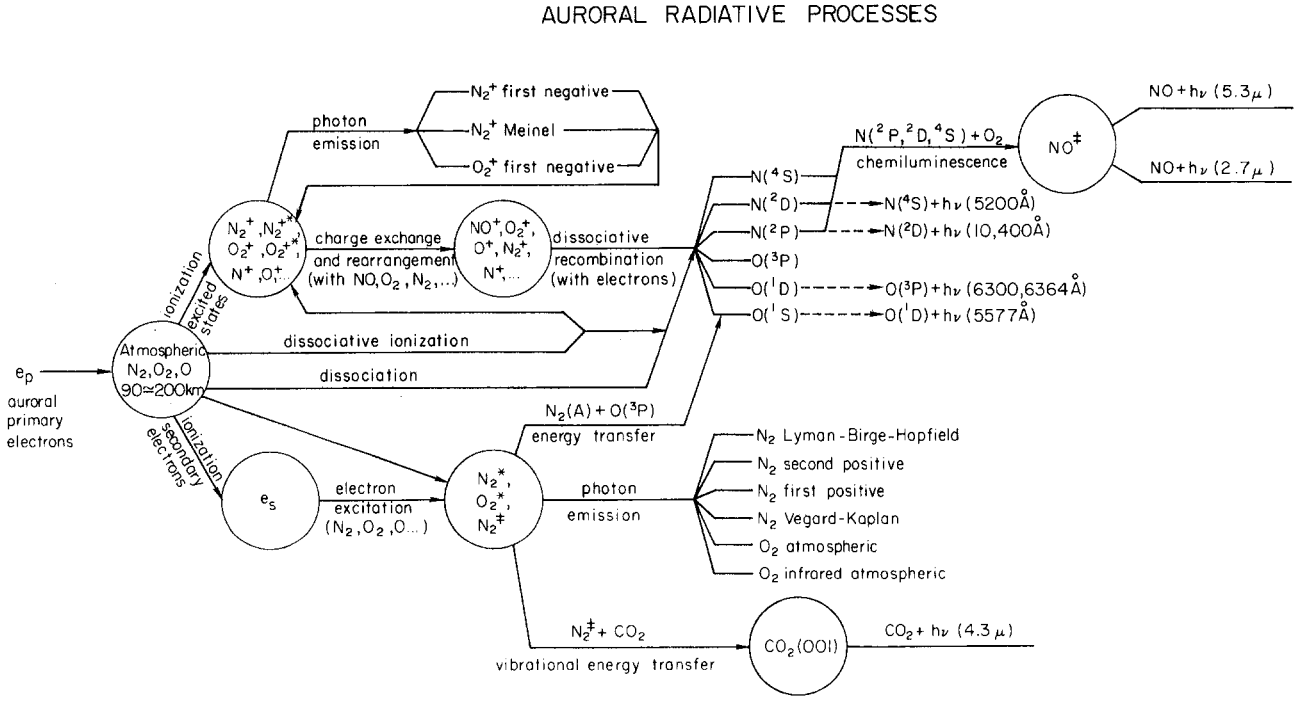

Figure 12-29. Schematic diagram of auroral radiative processes, showing sources of most important infrared emissions at 2.7, 4.3, and 5.3 μm.

the result of energy transfer

$$M^* + N \rightarrow M + N^*, \qquad (12.13)$$

or the result of a chemiluminescent reaction

$$A + BC \rightarrow AB^* + C. \qquad (12.14)$$

Here the asterisk indicates an excited state of the atom or molecule. In the case of energy transfer, production of the excited state N* has resulted from the collisional deactivation or quenching of the excited M* to some lower energy state. For the chemiluminescent reaction, some fraction of the exothermicity of the reaction has been converted to internal energy of the product molecule. A comprehensive review of auroral production and loss processes is given in the monograph by Vallance Jones [1974]. Production and loss processes for metastable states were recently reviewed by Torr and Torr [1982].

12.2.4 Auroral Processes

A flow diagram indicating some physical and chemical processes leading to selected ultraviolet, visible, and infrared auroral emissions is presented in Figure 12-29. This figure is schematic and indicates only examples of selected auroral production and loss mechanisms. All primary electrons with energies in excess of 100 eV partition their kinetic energy in the atmosphere in approximately the same branching ratios. That is, regardless of the primary electron energy, approximately the same fraction of the initial kinetic energy is spent in forming various ions (N_2^+, N_2^+*, N^+, N^+*, O_2^+, O_2^+*, O^+, . . .) or various neutral excited states (N_2^*, O_2^*, $N_2^\ddagger$, $CO_2^\ddagger$, $NO^\ddagger$, . . .). Here and in the remainder of this chapter, the asterisk is used to indicate electronically excited species, while the symbol ‡ indicates vibrational excitation.

Excited-state ions produced when the primaries ionize atmospheric neutrals may relax by spontaneous decay to a

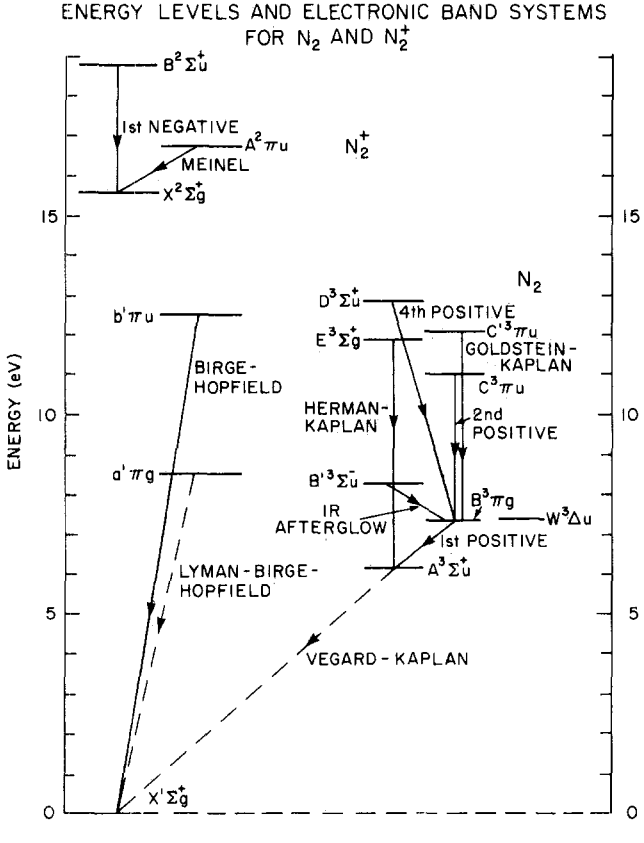

Figure 12-30. Electronic energy levels and principal electronic band system of N_2 and N_2^+ [adapted from Vallance Jones, 1974]. Forbidden transitions are indicated by dashed lines.

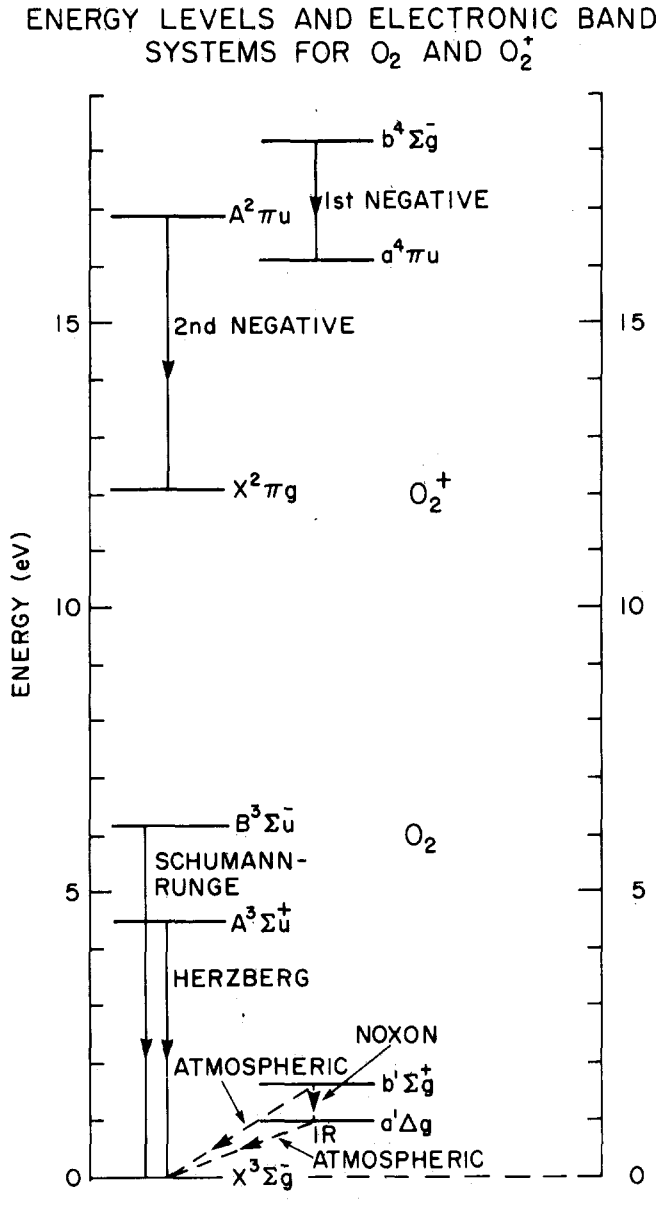

Figure 12-31. Electronic energy levels and principal electronic band systems of O_2 and O_2^+ [Vallance Jones, 1974]. Forbidden transitions are indicated by dashed lines.

lower state emitting a quantum of energy or photon in the process. The N_2^+ first negative ($B^2\Sigma_u^+ - X^2\Sigma_g^+$), N_2^+ Meinel ($A^2\Pi_u - X^2\Sigma_g^+$), and O_2^+ first negative ($b^4\Sigma_g^- - a^4\Pi_u$) systems (Figures 12-30 and 12-31) are examples of electronic transitions of molecular ions producing significant levels of auroral emissions. The secondary electrons resulting from ionization of the ambient atmosphere account for a large fraction of the primary electron's energy as it is slowed and stopped in the atmosphere by successive ionizing collisions. The secondary electrons lose most of their energy in inelastic collisions which result in excited states of neutral atmospheric species, N_2*, O_2*, and N_2‡. The N_2 ($a^1\Pi_g$) state, giving rise to the Lyman-Birge-Hopfield system, and vibrationally excited N_2‡ are representative of the excited-state neutral species produced by secondary electrons, as illustrated in Figures 12-29 and 12-30. Thus, the neutral excited species are produced by impact with neutrals of secondary electrons, which themselves result from ion-pair production by the more energetic primary auroral electrons. These excited neutral species, in turn, radiate, giving rise to aurorally enhanced emissions. Some of the affected band systems of N_2 and O_2 are shown in Figures 12-30 and 12-31.

The fraction of the primary electron energy radiated in a given optical transition as an energetic electron and its secondary electrons are stopped in the atmosphere is defined as the electron-induced radiant efficiency for that transition. The electron-induced radiant efficiency is independent of electron energy for energies greater than approximately 100 eV. Radiant efficiencies for selected auroral emissions are presented in Table 12-3, which indicates that 21 to 34% of the electron energy radiates in these auroral emissions, with the infrared emissions of CO_2 and NO accounting for large fractions of the incident electron energy. Table 12-3 is based

Table 12-3. Auroral IBC III intensities and electron-induced radiant efficiencies.

Emission	Zenith brightness[a](kR)	Electron-induced radiant efficiency (X 10^{-2})
N_2 first positive system[b]	900	1.6
N_2 second positive system[c]	90	0.5
N_2 Lyman-Birge-Hopfield system	380	4.4
N_2 Vegard-Kaplan system	55	0.3
N_2^+ first negative system	150	0.7
N_2^+ first negative (0-0) band	98	0.45[d]
N_2^+ Meinel system[e]	770	1.3
O_2 atmospheric system	1300	3.0
O_2 infrared atmospheric system	2500	3.5
O_2^+ first negative system	26	0.1
NO γ band	60	0.5
NI 8680 Å (^4P–$^4D^o$)	10.5	0.022
NII 2144 Å (^3P–$^5S^o$)	32[f]	0.3
OI 7774 Å ($^5S^o$–^5P)	9.6	0.022
OI 8446 Å ($^3S^o$–^3P)	11.5	0.024
OI 5577 Å (^1D–^1S)	100[d]	0.32
OI 6300, 6364 Å (^3P–^1D)[g]	2–100	0.0056–0.28
OI 1302–1306 Å (2^3P–3^3S^o)	30	0.4
NO first overtone 2.7 μm[h]	0.5–1.4 × 10^3	0.4–1.0
CO_2 (001–000) 4.3 μm[i,j]	3–30 × 10^3	1–12
NO fundamental 5.3 μm[k]	6–12 × 10^3	2–4
		Total 20.8–34.7

[a]Intensities are from Vallance Jones [1974], unless otherwise indicated.
[b]Vallance Jones and Gattinger [1976].
[c]Vallance Jones and Gattinger [1975].
[d]Reference value.
[e]Gattinger and Vallance Jones [1981].
[f]Sharp [1978].
[g]Intensity and efficiency are strongly altitude (or primary electron energy) dependent.
[h]R.J. Huppi and Stair [1979].
[i]Values are typical for rocketborne measurements of this strongly self-absorbed band. The primary production process, vibrational energy transfer from N_2‡, is a slow process, and steady-state radiance efficiencies are difficult to establish. See Stair et al. [1975].
[j]See also Gordiets et al. [1978].
[k]Inferred from Caledonia and Kennealy [1982].

principally on the auroral multiplet and band system intensities presented by Vallance Jones [1974] for an IBC III aurora and assumes an electron-induced radiant efficiency of 4.5 × 10^{-3} for the N_2^+ first negative (0-0) band at 3914 Å.

The band system intensities of Table 12-3 are given in Rayleighs (R). The unit, proposed by Hunten et al. [1956], is an equivalent column radiance of 10^6 photons cm^{-2} s^{-1} and was named in honor of the fourth Lord Rayleigh, who made the initial measurement of the absolute intensity of the night airglow. Standards of auroral optical intensity were proposed by Seaton [1954] and Hunten [1955] based on the brightness of the most intense visible feature of the aurora, the O(^{1}S – ^{1}D) 5577 Å auroral green line (Figure 12-32).

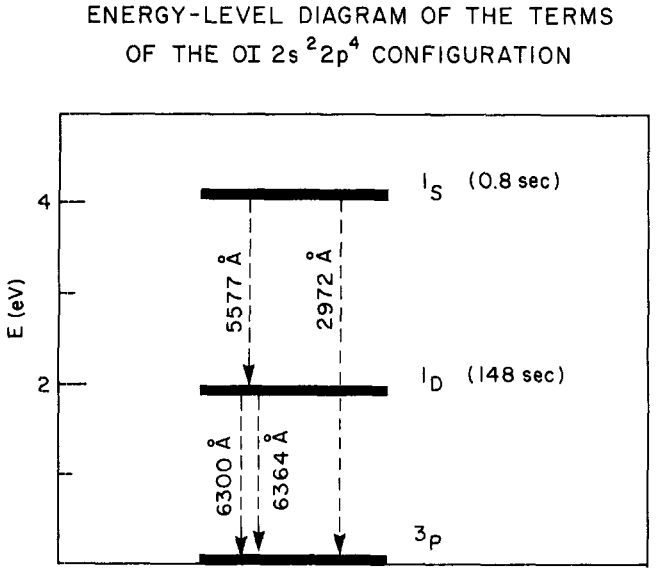

Figure 12-32. Lowest-lying energy levels and forbidden transitions in atomic oxygen. The radiative lifetimes of the ^{1}S and ^{1}D levels are indicated.

The result was the establishment of a logarithmic scale, the International Brightness Coefficient (IBC), defined in Table 12-4. In Figure 12-19 the IBC is related to other auroral parameters, such as the electron energy flux, peak E region electron density at steady-state, and optical radiance at 3914 Å.

The probability of radiative decay, or Einstein transition probability $A_{u\ell}$, is governed by quantum-mechanical selection rules [Herzberg, 1950], the most important of which are the electric-dipole selection rules. Transitions obeying electric dipole selection rules have high probability for decay (large $A_{u\ell}$ values) and are designated as allowed or permitted transitions. The N_2^+ first negative, N_2^+ Meinel (Figure 12-30), and O_2^+ first negative (Figure 12-31) transitions are examples of allowed electronic transitions. Transitions violating the selection rules have small transition probabilities and are denoted as forbidden transitions. Excited states from which only forbidden transitions originate are metastable. Forbidden transitions in atomic oxygen, atomic nitrogen, molecular oxygen, and molecular nitrogen are important auroral transitions (Figure 12-29), and their intensities and altitude profiles have been used as indices of both auroral brightness and auroral color type.

Table 12-4. International Brightness Coefficient (IBC).

IBC Class	Brightness (kR), 0(^{1}S–^{1}D) 5577 Å
I	1
II	10
III	100
IV	1000

The color of an aurora varies markedly and has been used to classify auroras into color classes according to the International Auroral Atlas (IAA), published by the International Union of Geodesy and Geophysics in 1963. Since energetic electrons penetrate to lower altitudes, the color variations are primarily due to differing mean energies and energy distributions for the primary electrons incident on the atmosphere. Metastable species with small Einstein transition probabilities are vulnerable to collisional deactivation at relatively low gas densities (high altitudes). The O(^{1}D) state (Figure 12-32) with an A value of 6.8 × 10^{-3} s^{-1} is quenched in collisions with N_2 at altitudes less than 300 km. Thus, at altitudes less than 300 km, the 6300 Å auroral red line emissions from this state to $^3P_2$ and $^3P_1$ levels are diminished relative to other visible emissions. As a consequence, ground-based measurements of the 4278 Å N_2^+ first negative (0 – 1) band intensity I(4278) and of the atomic oxygen red line intensity I(6300) can be used to determine the total auroral electron flux and characteristic electron energy, or equivalently the altitude profile of energy deposition [Rees and Luckey, 1974; Shepherd and Eather, 1976]. While I(4278) is proportional to the total energy deposited, I(6300)/I(4278) is sensitive to the altitude profile of energy deposition and decreases in value for lower altitude auroras (more energetic primary electrons).

Similarly, the O(^{1}S) state, which is the source of the green line (Figure 12-32), has an A coefficient of 1.25 s^{-1} and is quenched by O_2 at altitudes less than 100 km. The collisional destruction of this species contributes to the red lower border of the type-B red aurora. The $N_2(A^3\Sigma_u^+)$ state (Figure 12-30) is the major source of O(^{1}S) in the aurora through the energy-transfer process (Figure 12-29)

$$N_2(A^3\Sigma_u^+) + O(^3P) \rightarrow O(^1S) + N_2, \quad (12.15)$$

as reported by O'Neil et al. [1979] and Piper [1982]. Einstein A coefficients for molecular transitions of auroral interest, in some cases summed over all possible lower states, are given in Table 12-5, while A coefficients for atomic oxygen transitions are the reciprocals of the lifetimes listed in Figure 12-32. Ultraviolet and visible auroral spectra re-

Table 12-5. Einstein coefficients for auroral molecular transitions.[a]

System	v′	$\sum_{v''} A_{v'v''}(s^{-1})$
N_2 first positive ($B^3\Pi_g$-$A^3\Sigma_u^+$)	0	1.12 (+5)[b]
(2.53–0.478 μm)	1	1.29 (+5)
	2	1.43 (+5)
	3	1.54 (+5)
	4	1.64 (+5)
	5	1.73 (+5)
	6	1.81 (+5)
	7	1.98 (+5)[c]
	8	2.12 (+5)[c]
	9	2.27 (+5)[c]
	10	2.31 (+5)[c]
	11	2.39 (+5)[c]
	12	2.43 (+5)[c]
N_2 second positive ($C^3\Pi_u$-$B^3\Pi_g$)	0	2.73 (+7)
(0.546–0.268 μm)	1	2.75 (+7)
	2	2.73 (+7)
	3	2.67 (+7)
	4	2.50 (+7)
N_2 Wu-Benesch($W^3\Delta_u$-$B^3\Pi_g$)	0	6.00 (−2)
(2.2–4.3 μm)	1	5.00 (+2)
	2	2.04 (+3)
	3	4.28 (+3)
	4	7.26 (+3)
	5	1.08 (+4)
	6	1.45 (+4)
	7	1.84 (+4)
N_2 Vegard-Kaplan ($A^3\Sigma_u^+$-$X^1\Sigma_g^+$)	0	5.30 (−1)
(0.532–1.25 μm)		
N_2 Lyman-Birge-Hopfield ($a^1\Pi_g$-$X^1\Sigma_g^+$)[d]		6.7 (+3)
(0.260–0.100 μm)		
N_2 Herman-Kaplan ($E^3\Sigma_g^+$-$A^3\Sigma_u^+$)[e]		3.0 (+3)
(0.274–0.213 μm)		
N_2^+ first negative ($B^2\Sigma_u^+$-$X^2\Sigma_g^+$)	0	1.41 (+7)
(0.587–0.286 μm)	1	1.38 (+7)
	2	1.4 (+7)
N_2^+ Meinel ($A^2\Pi_u$-$X^2\Sigma_g^+$	0	6.04 (+4)
(0.177–0.550 μm)	1	7.20 (+4)
	2	8.30 (+4)
	3	9.34 (+4)
	4	1.03 (+5)
	5	1.12 (+5)
	6	1.21 (+5)
	7	1.30 (+5)
	8	1.37 (+5)
	9	1.45 (+5)
	10	1.52 (+5)

System	v′–v″	$A_{v'v''}$ (s^{-1})	Band origin (μm)
O_2 atmospheric ($b^1\Sigma_g^+$-$X^3\Sigma_g^-$)[f]	0–0	8.5 (−2)	0.7619
	1–0	6.9 (−3)	0.6882
	2–0	(1.636 ± 0.040) (−4)	0.6287
	1–1	(7.04 ± 0.42) (−2)	0.7708
	0–1	4.16 (−3)[g]	0.8645
O_2 IR atmospheric ($a^1\Delta_g$-$X^3\Sigma_g^-$)[f]	0–0	2.58 (−4)[g]	1.269
	0–1	1.75 (−6)[g]	1.580
O_2 Noxon ($b^1\Sigma_g^+$-$a^1\Delta_g$)[f]	0–0	1.5 (−3)	1.908

[a]All data are from Loftus and Krupenie [1977] unless otherwise indicated.
[b]The notation "a(n)" means "ax10^n".
[c]Eyler and Pipkin [1983].
[d]Corrected for a → a′ cascade [Freund, 1972].
[e]Using relative transition probabilities for E → A, E → C, and E → B from Freund [1969] and lifetime of E state from Borst and Zipf [1971].
[f]Krupenie [1972].
[g]Calculated from upper-state lifetime and Franck-Condon factor.

sulting from the EXCEDE artificial auroral experiment are presented in Figures 12-33a and b. Natural auroral spectra in the ultraviolet and visible are shown in Figures 12-34 through 12-37.

Caution is urged in applying artificial auroral spectra to situations involving natural aurora. The former are biased toward prompt emitters, and delayed emitters such as the CO_2 4.3 μm band may not be measured efficiently. This is true of ground-based spectra such as Figure 12-33b due to continual motion of the electron gun through the atmosphere into undosed regions. However, the remark applies especially to rocketborne spectra, where the spectrometer can only observe a dosed region for a short while.

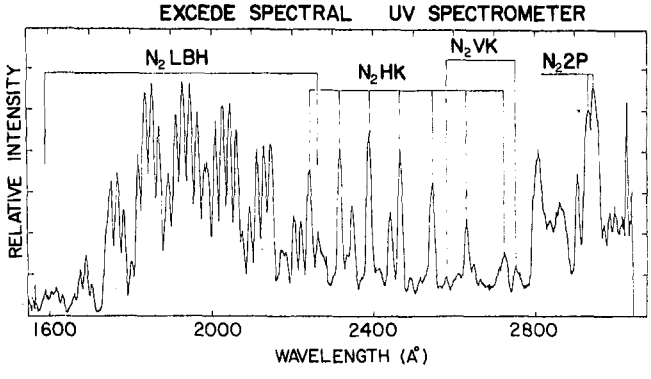

Figure 12-33a. Ultraviolet spectrum taken during EXCEDE SPECTRAL artificial auroral experiment at 125 km altitude. Principal band systems seen are the Lyman-Birge-Hopfield (LBH), Herman-Kaplan (HK), Vegard-Kaplan (VK), and second positive (2P) systems of N_2 [O'Neil et al., 1982].

12.2.5 Infrared Auroral Emissions

The development of infrared cryogenic instrumentation and sensors has facilitated the measurement of infrared auroral emissions in recent years [Stair et al., 1983]. Infrared artificial auroral spectra from EXCEDE are shown in Figures 12-38a and b, while natural airglow and auroral emissions in the 0.88 to 5.4 μm range are illustrated in Figures

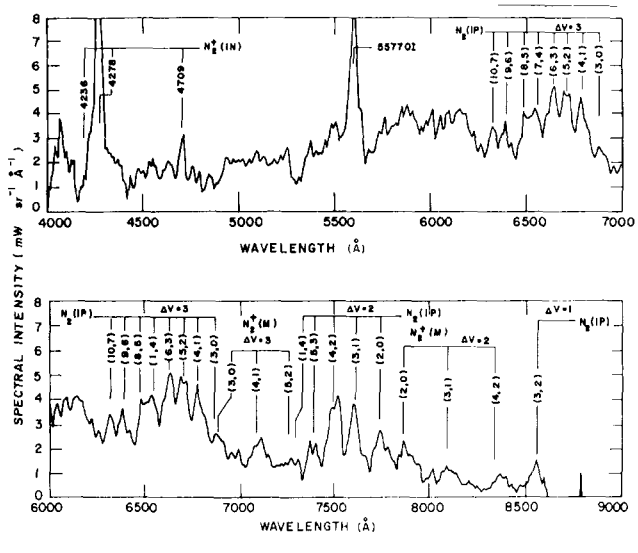

Figure 12-33b. Visible spectrum taken from the ground with an image-intensified spectrograph during the PRECEDE artificial auroral experiment with payload at 92 km. Principal band systems seen are N_2^+ first negative (1N) and Meinel (M) systems and the N_2 first positive (1P) system [O'Neil et al., 1978a].

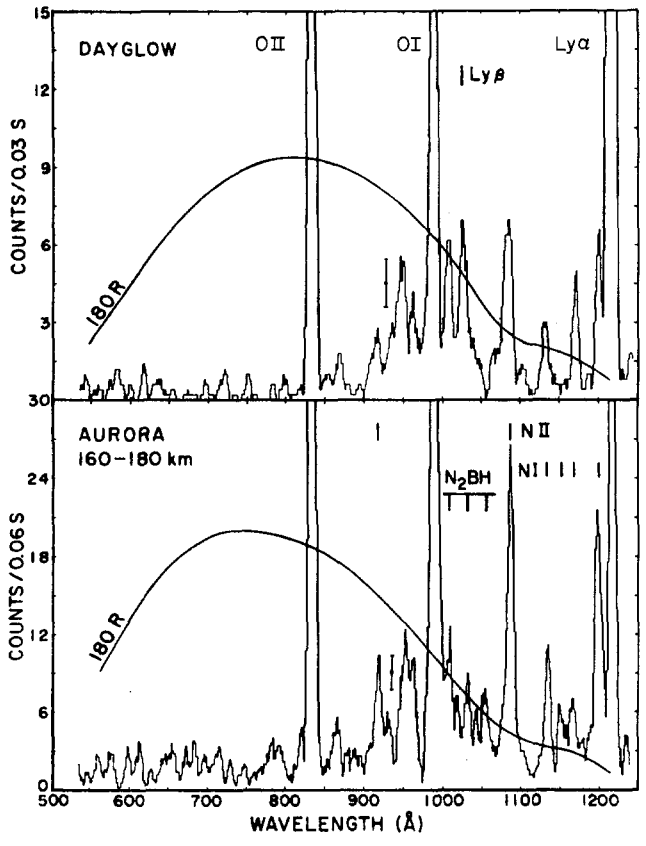

Figure 12-34a. Extreme ultraviolet side-looking spectrum (525–1250 Å) of a natural aurora taken at 160–180 km altitude (bottom), with a comparable measured dayglow spectrum (top). Principal band system is the N_2 Birge-Hopfield (BH) system. Prominent N I and N II lines and off-scale O I, O II, and Ly-α lines are also present [Feldman and Gentieu, 1982].

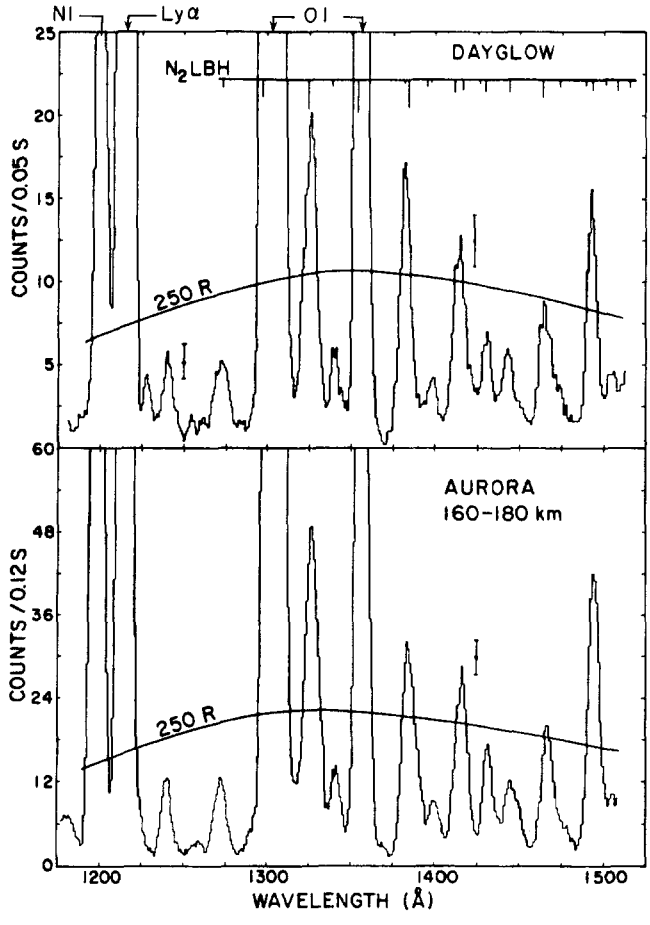

Figure 12-34b. Far ultraviolet auroral spectrum (1175–1520 Å) under the same conditions as Figure 12-34a. Dominant features are the N_2 Lyman-Birge-Hopfield (LBH) band system and atomic emissions from N I (1200 Å), Ly α (1216 Å), and O I (1304 and 1356 Å) [Feldman and Gentieu, 1982].

12- 39, 12-40, and 12-41. Spectra of the near-infrared portion of this range are also shown by D. Baker et al. [1977]. Emissions in this wavelength range correspond to energies varying from 1.4 eV at 0.88 μm to 0.23 eV at 5.3 μm. The energy levels involved in these less energetic transitions producing infrared emission are both electronic states of N_2 and O_2 (Figures 12-30 and 12-31) and vibrational transitions within the ground electronic state of minor atmospheric species. Pure vibrational transitions are forbidden in the homonuclear diatomic molecules N_2 and O_2 forming the major constituents of the atmosphere. Thus infrared-active minor atmospheric species, such as the diatomics OH, CO, NO, and NO^+ and the triatomic species CO_2, N_2O, NO_2, and O_3 become the principal sources of infrared airglow [Chapter 13] and auroral emissions at longer wavelengths. The potential energy curve and fundamental and first-overtone vibrational transitions of NO are shown in Figure 12-42, and the band origins and Einstein coefficients are given in Table 12-6. The vibrational energy levels of CO_2

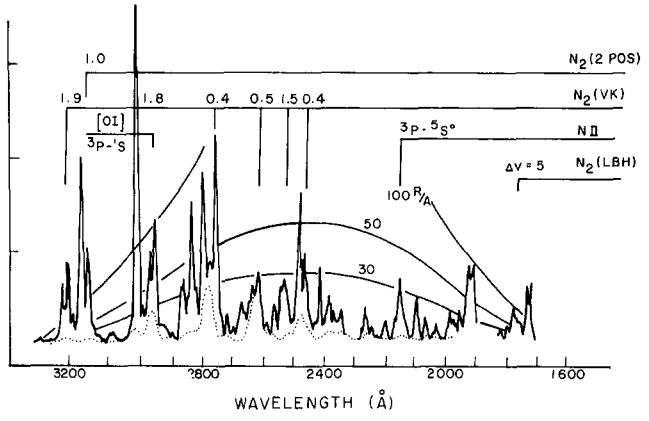

Figure 12-35. Far ultraviolet auroral spectrum from a nadir-looking satellite (1700–3200 Å). Principal band systems are the N_2 Lyman-Birge-Hopfield (LBH), Vegard-Kaplan (VK), and second positive (2POS) systems [Sharp and Rees, 1972; Sharp, 1978]. The dotted curve is a synthetic spectrum.

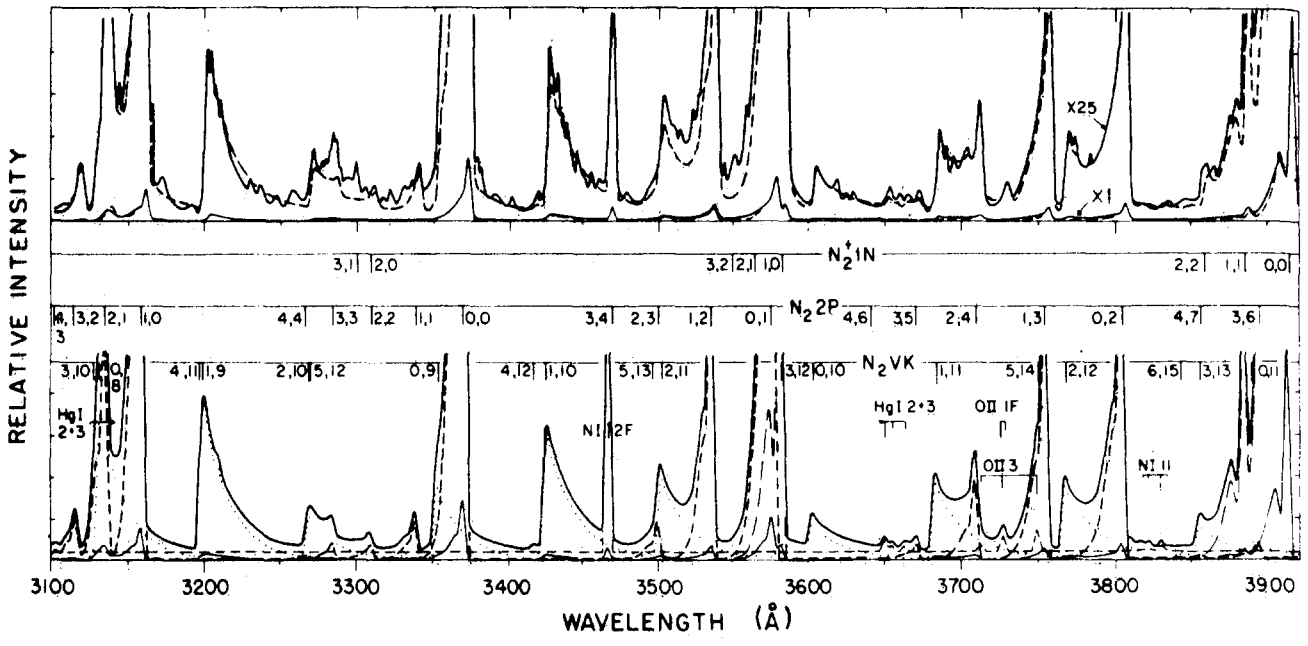

Figure 12-36a. Observed ultraviolet ground-based spectrum of an aurora from 3100–3920 Å (top) along with synthetic spectrum (bottom). The synthetic spectrum is also shown as a dotted line in the top panel, and various components of the synthetic spectrum are shown in the bottom panel. Several band systems are shown with the same notation as in Figures 12-33a,b [Vallance Jones and Gattinger, 1975].

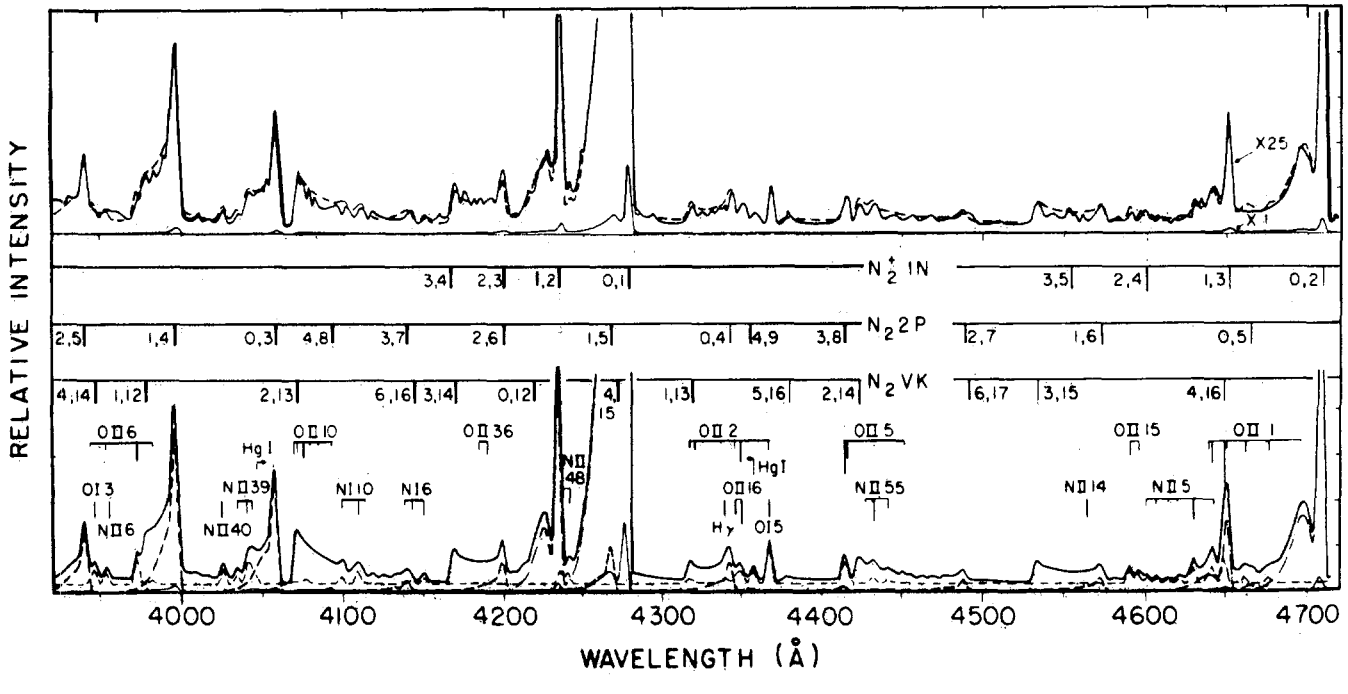

Figure 12-36b. Ground-based visible auroral spectrum from 3920– 4720 Å. Details are as in Figure 12-36a [Vallance Jones and Gattinger, 1975].

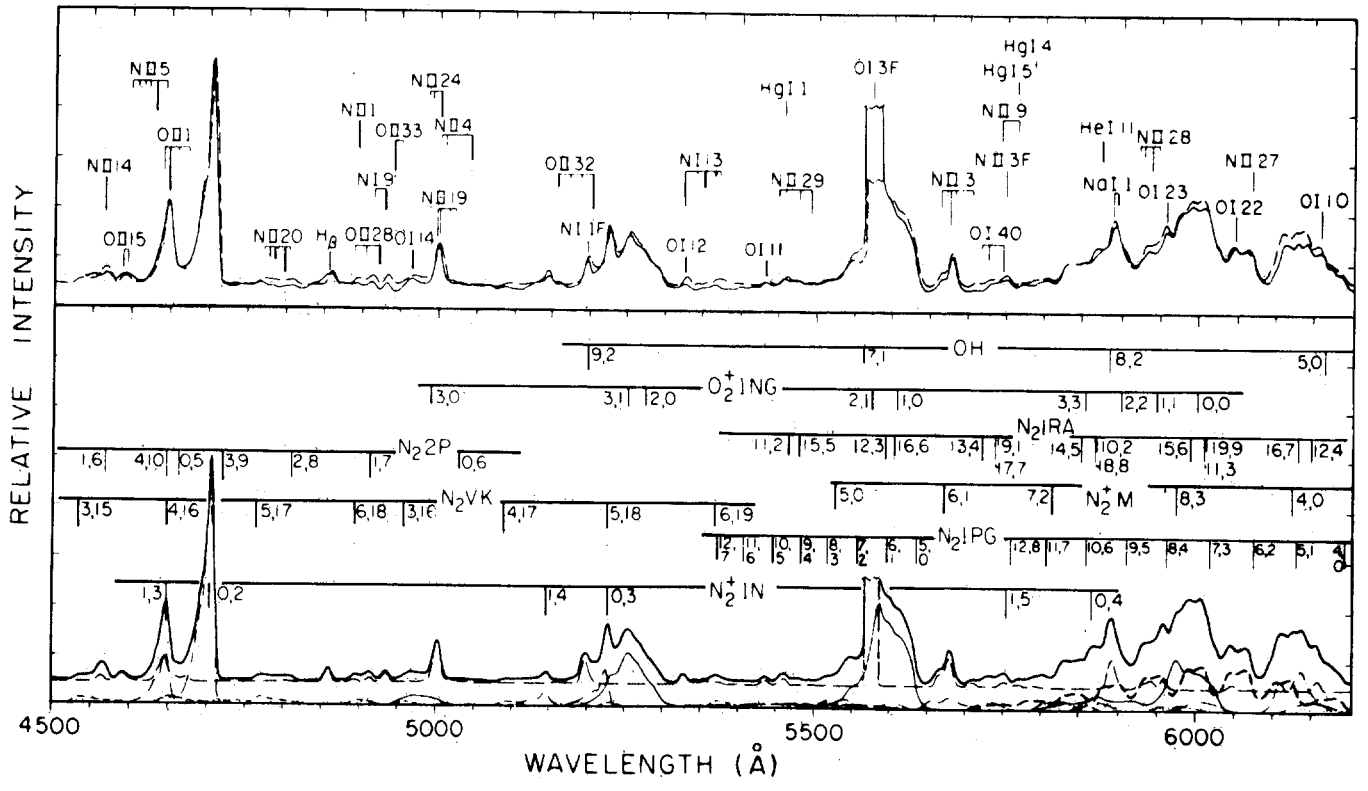

Figure 12-37a. Ground-based visible auroral spectrum from 4500– 6200 Å. Details are as in Figure 12-36a. Additional band systems shown are the O_2^+ first negative (1N) and the N_2 infrared afterglow (IRA) [Gattinger and Vallance Jones, 1974].

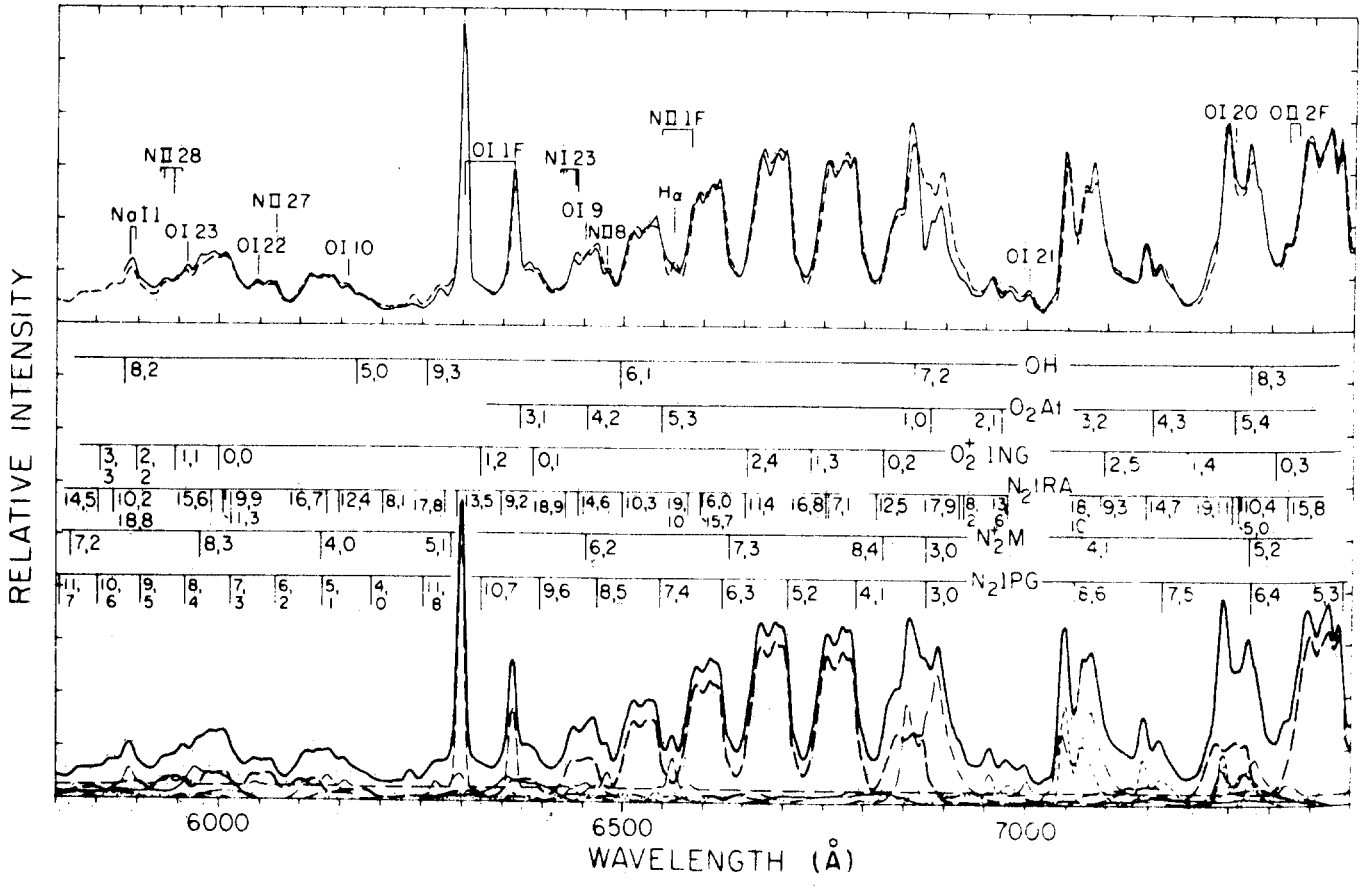

Figure 12-37b. Same as Figure 12-37a, but for spectral range 5800– 7400 Å. One additional band system, the O_2 atmospheric (At), is present.

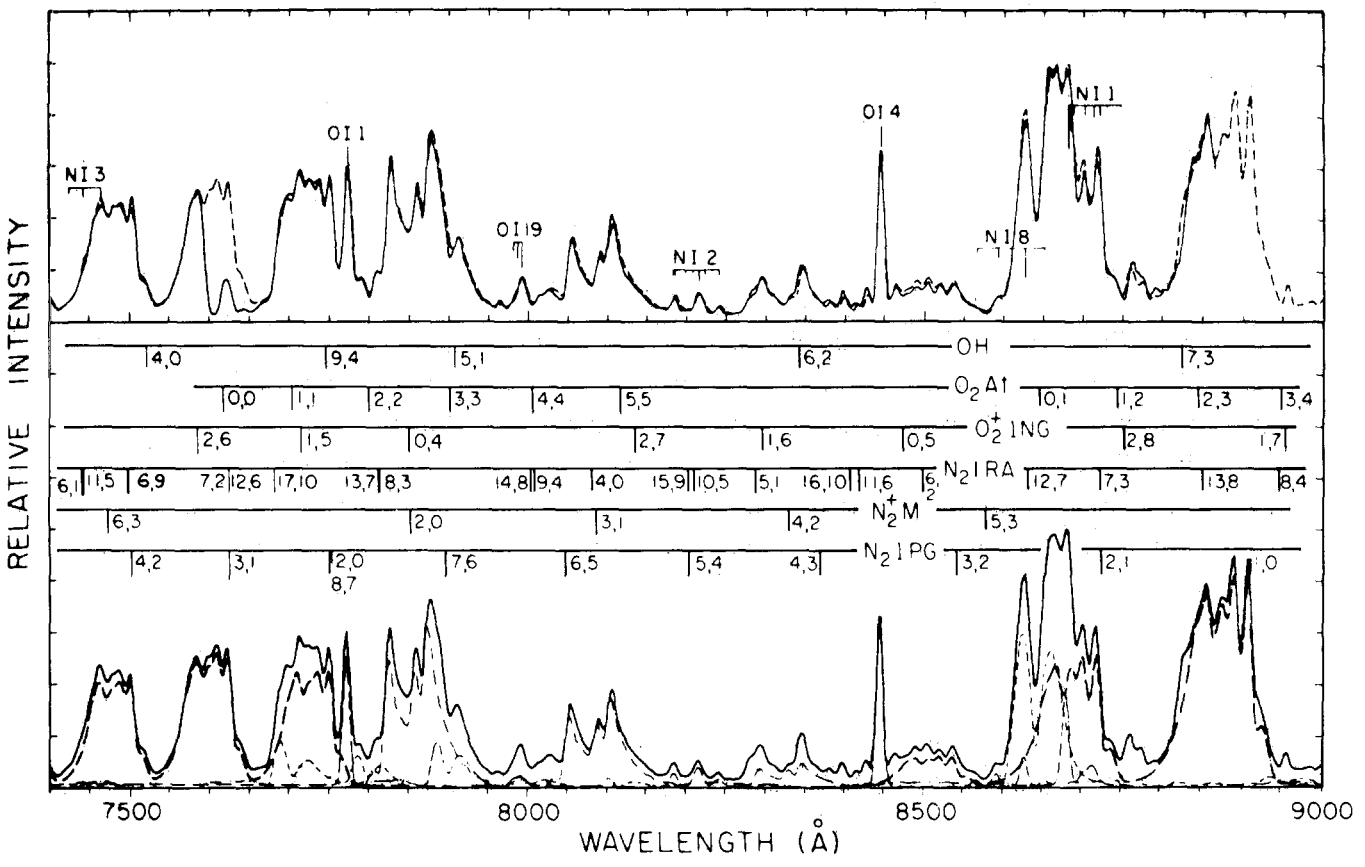

Figure 12-37c. Same as 12-37a, but for the spectral range 7400–9000 Å.

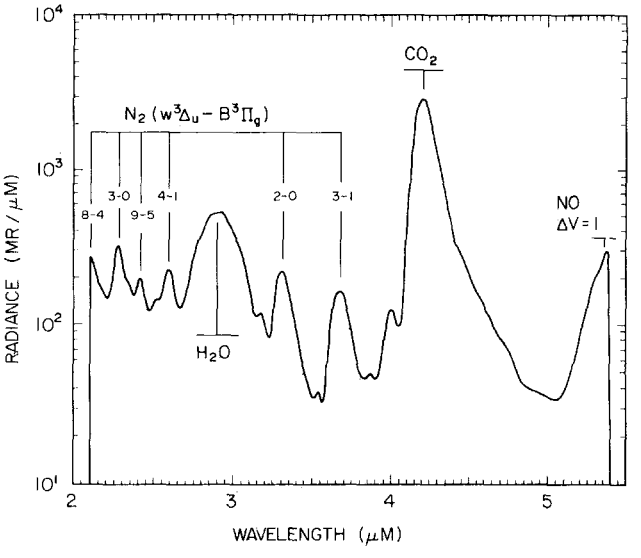

Figure 12-38a. Short-wave infrared spectrum taken of electron-induced emission with liquid-nitrogen-cooled spectrometer during EXCEDE artificial auroral experiment at altitude of 74 km. Dominant emissions are the N_2 Wu-Benesch band system, as well as NO and CO_2 vibrational bands [O'Neil et al., 1982].

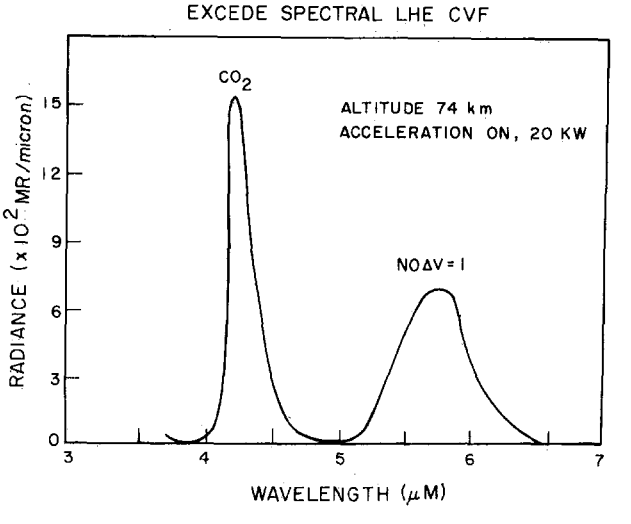

Figure 12-38b. Electron-induced infrared spectra taken with liquid-helium-cooled spectrometer at 74 km during EXCEDE artificial auroral experiment [O'Neil et al., 1982].

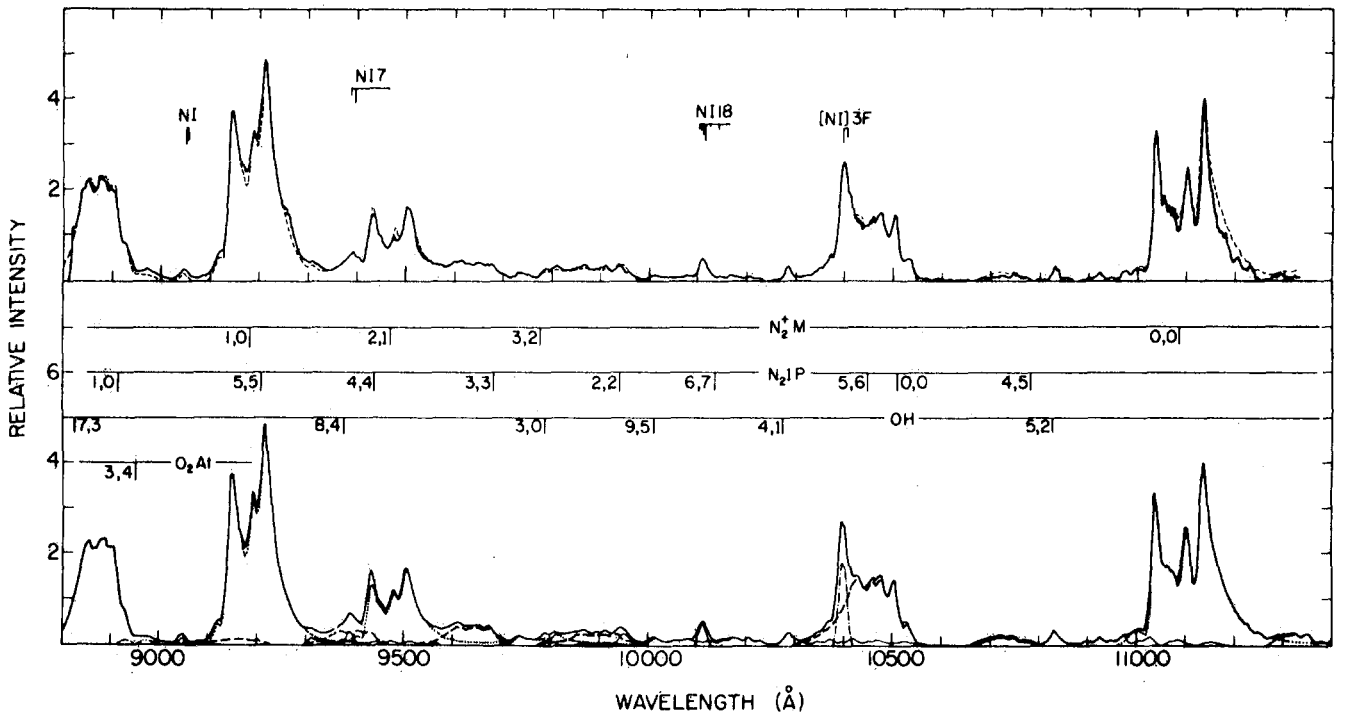

Figure 12-39. Observed ground-based auroral near-infrared spectrum from 8800–11400 Å (top), along with synthetic spectrum (bottom). Details are as shown in Figure 12-36a [Vallance Jones and Gattinger, 1976].

are schematically represented in Figure 12-43, and the band origins and transition probabilities for CO, CO_2, N_2O, NO_2, H_2O, O_3, and NO^+ are presented in Table 12-7.

Not all the above atmospheric infrared radiators give rise to emissions that are aurorally enhanced. Modest two-fold enhancements of the 1.27 μm emission from the O_2 (0—0) infrared atmospheric band ($a^1\Delta_g - X^3\Sigma_g^-$) (Figure 12-31) have been reported in a very strong IBC III$^+$ aurora, and the enhancement has been explained through direct electron excitation of O_2 [D.J. Baker et al., 1978]. Due to the long lifetime (3900 s) of the $O_2(a^1\Delta_g)$ state, horizontal winds can transport the excited species downwind by several hundred kilometers before it decays [Rees and Roble, 1980], serving to complicate the analysis. The Wu-Benesch bands of N_2 ($W^3\Delta_u - B^3\Pi_g$) (Figure 12-30) are strong features of the EXCEDE artificial auroral spectra (Figure 12-38a) in the 2–4 μm region, but have not been observed in natural auroras, probably due to lack of sensor sensitivity. Recent observations [Stair et al., 1983] during the HIRIS experiment indicate enhancements of the 15 μm CO_2 ν_2 band emission as well as the 9.6 μm O_3 ν_3 band emission in a very strong (IBC III$^+$) aurora. However, no mechanism for these enhancements is known at the present time. Consequently, these observations await elaboration through further experiments and data analysis. The remainder of this section deals with the most firmly established and best understood infrared auroral enhancements, namely the 2.7 μm and 5.3 μm emission from NO and the 4.3 μm emission from CO_2.

Nitric oxide is an important minor constituent in the thermosphere. It is infrared-active, radiating near 5.3 μm in the fundamental $\Delta v = 1$ sequence and near 2.7 μm in the first overtone ($\Delta v = 2$) (Figure 12-41). The 5.3 μm fundamental band emission is an important cooling mechanism for the thermosphere [Chapter 13; Kockarts, 1980]. The $v = 1$ state is predominantly produced, in the nighttime quiescent atmosphere, by collision with atomic oxygen and by absorption of earthshine [Chapter 13],

$$NO\ (v = 0) + O \rightleftarrows NO\ (v = 1) + O \qquad (12.16)$$

$$NO\ (v = 0) + h\nu\ (\text{earthshine}) \rightarrow NO\ (v = 1). \qquad (12.17)$$

These processes primarily produce the NO ($v = 1$) level with insignificant population of levels $v \geq 2$.

Vibrationally excited NO is also produced by chemical reactions initiated by precipitating auroral electrons. Laboratory studies have shown that the major chemiluminescent auroral process that produces NO (Figure 12-29),

$$N(^2D) + O_2 \rightarrow NO(v) + O, \qquad (12.18)$$

populates NO levels up to $v = 12$ [Kennealy et al., 1978]. The $N(^2D)$ is produced directly from N_2 by precipitating

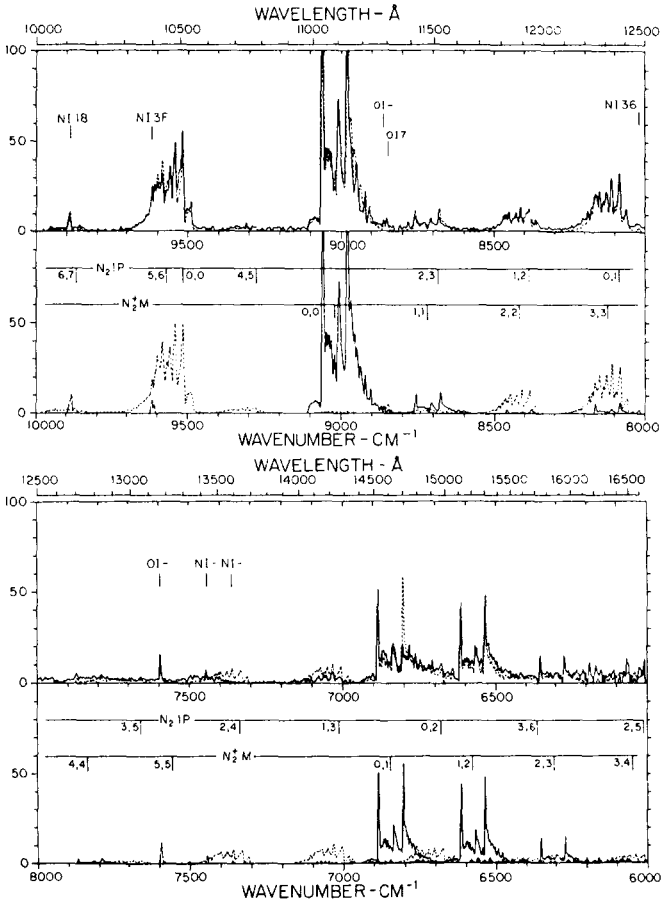

Figure 12-40. Infrared spectrum from 1.0 to 1.65 μm taken from the ground (top panels) along with corresponding synthetic spectra (bottom panels) [Gattinger and Vallance Jones, 1981].

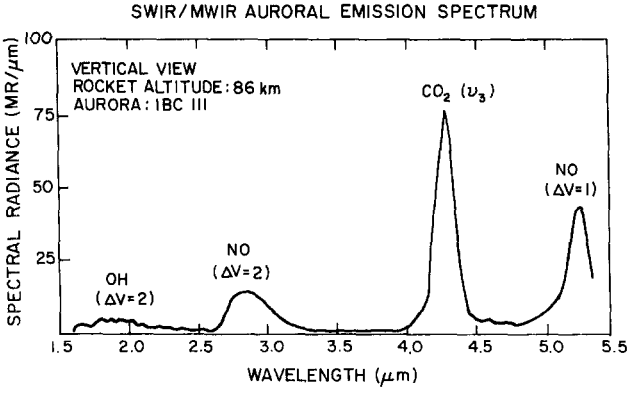

Figure 12-41. Zenith spectrum of natural aurora in the 1.5 to 5.4 μm spectral range taken from 86 km showing principal emitters [Stair et al., 1975].

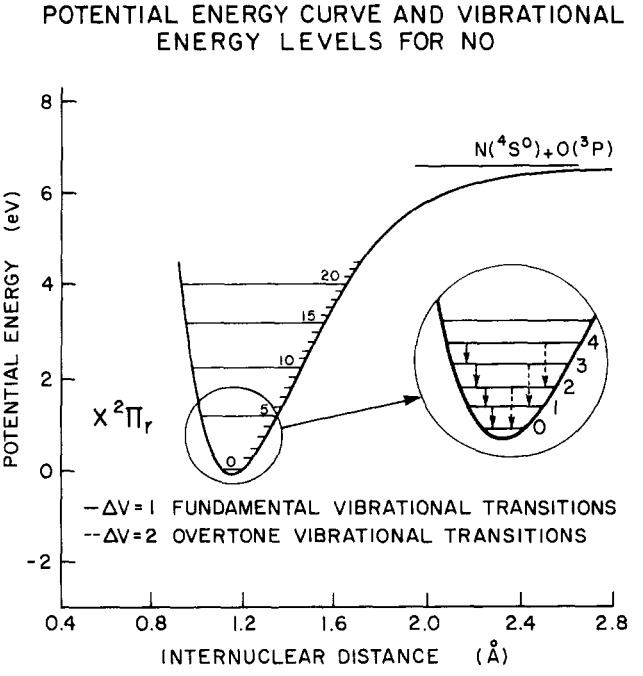

Figure 12-42. Potential energy curve for lowest electronic state of nitric oxide, showing vibrational energy levels as well as fundamental and first overtone vibrational transitions [adapted from Gilmore, 1965].

electrons and by dissociative recombination and charge-exchange reactions of aurorally produced ionic species,

$$
\begin{aligned}
N_2 + e &\rightarrow 2e + f_1 N(^2D) + (1 - f_1)\, N(^4S) + N^+ \\
N_2 + e &\rightarrow e + 2f_2 N(^2D) + 2(1 - f_2) N(^4S) \\
N_2^+ + e &\rightarrow 2f_3 N(^2D) + 2(1 - f_3) N(^4S) \\
NO^+ + e &\rightarrow 0.76\, N(^2D) + 0.24\, N(^4S) + O \\
N_2^+ + O &\rightarrow f_4\, N(^2D) + (1 - f_4)\, N(^4S) + NO^+ \\
N^+ + O_2 &\rightarrow f_5\, N(^2D) + (1 - f_5)\, N(^4S) + O_2^+ .
\end{aligned}
\qquad (12.19)
$$

The branching ratios f_i are of crucial importance, but they are uncertain for all reactions except NO^+ recombination (f_4 and f_5 are probably near unity). Nevertheless, the proportion of $N(^2D)$ that reacts with O_2 to produce NO(v) should vary with altitude as the reaction of Equation (12.18) competes with quenching of $N(^2D)$ by atomic oxygen. The variation of the $[O]/[O_2]$ ratio with altitude above 100 km then leads to an altitude-dependent efficiency for auroral NO(v) production. The altitude dependence of this production efficiency can then account for the variability of 5.3 μm auroral emission with auroral strength since auroras produced by more energetic electrons have lower peak ionization altitudes.

Table 12-6. Band origins and thermally-averaged Einstein coefficients for the fundamental and first overtone vibrational transitions of nitric oxide.

	Δv = 1			Δv = 2		
	$A_{v'v''}$[a]	BAND ORIGIN[b]		$A_{v''v''}$[a]	BAND ORIGIN[b]	
v'	(s^{-1})	(cm^{-1})	(μm)	(s^{-1})	(cm^{-1})	(μm)
1	10.8	1876	5.33	—	—	—
2	20.4	1848	5.41	0.460	3724	2.68
3	29.1	1820	5.50	1.51	3668	2.73
4	36.5	1792	5.58	3.10	3612	2.77
5	42.9	1764	5.67	4.90	3556	2.81
6	48.5	1736	5.76	7.28	3500	2.86
7	53.5	1708	5.86	9.63	3444	2.90
8	57.5	1680	5.95	12.5	3388	2.95
9	60.6	1652	6.05	15.7	3332	3.00
10	62.8	1624	6.16	19.1	3275	3.05
11	64.2	1596	6.27	22.9	3219	3.11
12	64.6	1567	6.38	27.2	3163	3.16
13	64.2	1539	6.50	31.9	3107	3.22
14	63.2	1511	6.62	36.9	3050	3.28
15	61.7	1483	6.74	41.9	2994	3.34
16	59.8	1455	6.87	46.4	2938	3.40
17	57.6	1427	7.01	50.5	2882	3.47
18	55.0	1399	7.15	54.3	2825	3.54
19	51.9	1370	7.30	58.1	2769	3.61
20	48.5	1342	7.45	61.8	2713	3.69

[a]Billingsley [1976]
[b]Calculated from vibrational constants of Goldman and Schmidt [1975].

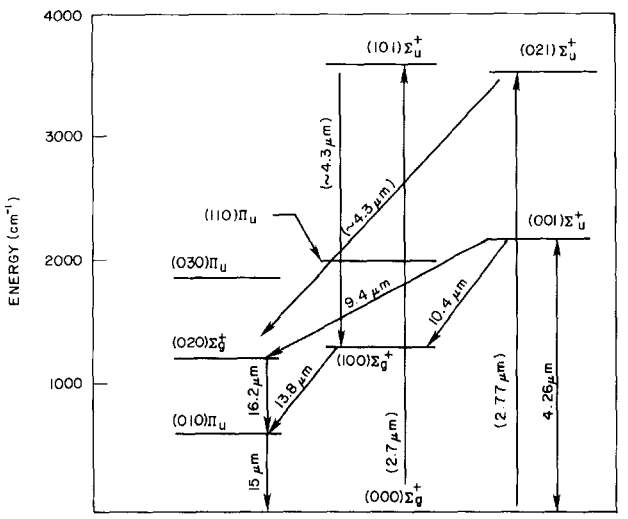

Figure 12-43. Lowest vibrational energy levels of CO_2 molecule showing some transitions of aeronomic interest.

The situation is somewhat complicated by the large variability of NO and by its transport. Since the rates of reaction of NO [Equations (12.16) and (12.17)] are proportional to the NO density, the nighttime quiescent component of the fundamental band should be stronger at high latitudes, especially in aurorally predosed regions where the NO density is expected to be large [Swider and Narcisi, 1977]. Nitric oxide is a long-lived species in the thermosphere, and model calculations have pointed out the importance of thermospheric winds in redistributing aurorally produced NO [Roble and Gary, 1979].

The NO 5.3 μm band radiance and the spectral shape of the emission depend on whether the NO(v) is produced by the quiescent mechanisms [Equations (12.16) and (12.17)] or the auroral mechanism [Equation (12.18)]. As alluded to previously, the quiescent processes can only excite the 1-0 transition, while the auroral process should yield in addition appreciable emission in the hot bands 2-1, 3-2, . . . , 12-11. Evidence of these components of the NO Δv = 1 emission in an aurora of only moderate intensity (IBC II) is clearly seen in the spectra resulting from the launch of a high-resolution (1.2 cm^{-1}) rocketborne field-widened interferometer (FWI) from Poker Flat, Alaska, in March 1983 [Steed et al., 1983; Murphy et al., 1983]. Preliminary analysis of the FWI flight data indicates that the hot band component increases with auroral energy deposition in a manner consistent with the mechanism of Equation (12.18).

In contrast to the 5.3 μm NO fundamental, the overtone band near 2.7 μm arises only when levels $v \geq 2$ are excited. Thermal collisions and earthshine do not populate these levels significantly, and thus the 2.7 μm emission is negligible during quiet nighttime conditions. However, the Δv = 2 sequence is observed even for moderate IBC II auroras [Caledonia and Kennealy, 1982], the emission occurring with an efficiency of 0.4–1.0% [R.J. Huppi and Stair, 1979; Reidy et al., 1982].

The altitude profiles of zenith spectral radiance measured during several earlier auroral rocket experiments in the ICECAP series involving lower-resolution spectrometers than the FWI, are shown in Figure 12-44 [Stair et al., 1975]. The 5.3 μm radiance is seen to be enhanced for the IBC III^+ aurora, but essentially at quiescent levels for the weaker IBC II and II^+ auroras. On the other hand, the 2.7 μm radiance is enhanced for both the IBC II and III^+ auroras recorded.

The failure to observe any enhancement of NO 5.3 μm radiance in moderate IBC II-II^+ auroras during the ICECAP series of flights contrasts sharply with the enhancement of the Δv = 1 hot band component seen in the FWI experiment during a moderate aurora. The lack of enhancement in the ICECAP observations is due to the existence of two conditions: (1) The ICECAP detector's long-wavelength cutoff, shown at 5.4 μm in the data of Figure 12-41, passes all of the Q and R branches of the NO (1-0) band, but misses more than half of the hot-band emission. (2) Quiescent-atmosphere emission dominates auroral emission in the re-

Table 12-7. Data on infrared bands of atmospheric interest.[a]

Species	Rotational constant B (cm^{-1})	Transition	Band Origin		Band strength S ($cm^{-2}atm^{-1}$ at 273 K)	Einstein coefficient A (s^{-1})	Reference
			Wave number ν_0 (cm^{-1})	Wavelength λ_0 (μm)			
CO_2	0.390	10^00–00^00	1388	7.20	Inactive	Inactive	c
		01^10–00^00	667.4	15.0	205	1.28	c
		00^01–00^00	2349	4.26	2380	368	c
		10^01–00^00	3715	2.69	37.2	14.4	c
		20^01–00^00	4978	2.01	0.868	0.603	c
		00^01–10^00	961.0	10.4	0.0170[b]	0.411	c
H_2O	d	100–000	3657	2.73	12.0	4.52	e
		010–000	1595	6.27	257	18.30	f
		001–000	3756	2.66	172	67.90	e
		011–000	5331	1.88	19.9	15.90	e
N_2O	0.419	00^01–00^00	2224	4.50	1420	196	g
		01^10–00^00	588.8	17.0	24.4	0.119	e
		10^00–00^00	1285	7.78	218.0	10.1	e
O_3	d	100–000	1103	9.07	16.6	0.568	f
		010–000	700.9	14.3	15.6	0.214	f
		001–000	1042	9.60	345	10.5	f
NO_2	d	100–000	1320	7.58	—	—	h
		010–000	749.6	13.3	13.1	0.207	i
		001–000	1617	6.18	1520	111	i
		101–000	2906	3.44	64.0	15.2	i
CO	1.931	1–0	2143	4.67	243	31.3	e
		2–0	4260	2.35	1.86	1.12	e
NO^+	1.997	1–0	2344	4.27	70.8	10.9	j
		2–0	4656	2.15	1.15	0.697	j
		2–1	2312	4.32	135[b]	20.2	j
NO	1.705	1–0	1876	5.33	109	10.8	k
		2–0	3724	2.68	1.18	0.460	k
OH	18.871	1–0	3570	2.80	24.0	8.58	i
		2–0	6974	1.43	8.98	12.2	i

[a]Table adapted and updated from Kennealy and Del Greco [1972].
[b]Band strength is strongly temperature-dependent, since the lower level is not the ground state.
[c]Rothman and Young [1981].
[d]Molecule is an asymmetric rotor with three distinct rotational constants.
[e]Rothman [1981].
[f]Rothman et al. [1983b].
[g]McClatchey et al. [1973].
[h]Herzberg [1945].
[i]Rothman et al. [1983a].
[j]Werner and Rosmus [1982].
[k]Billingsley [1976].

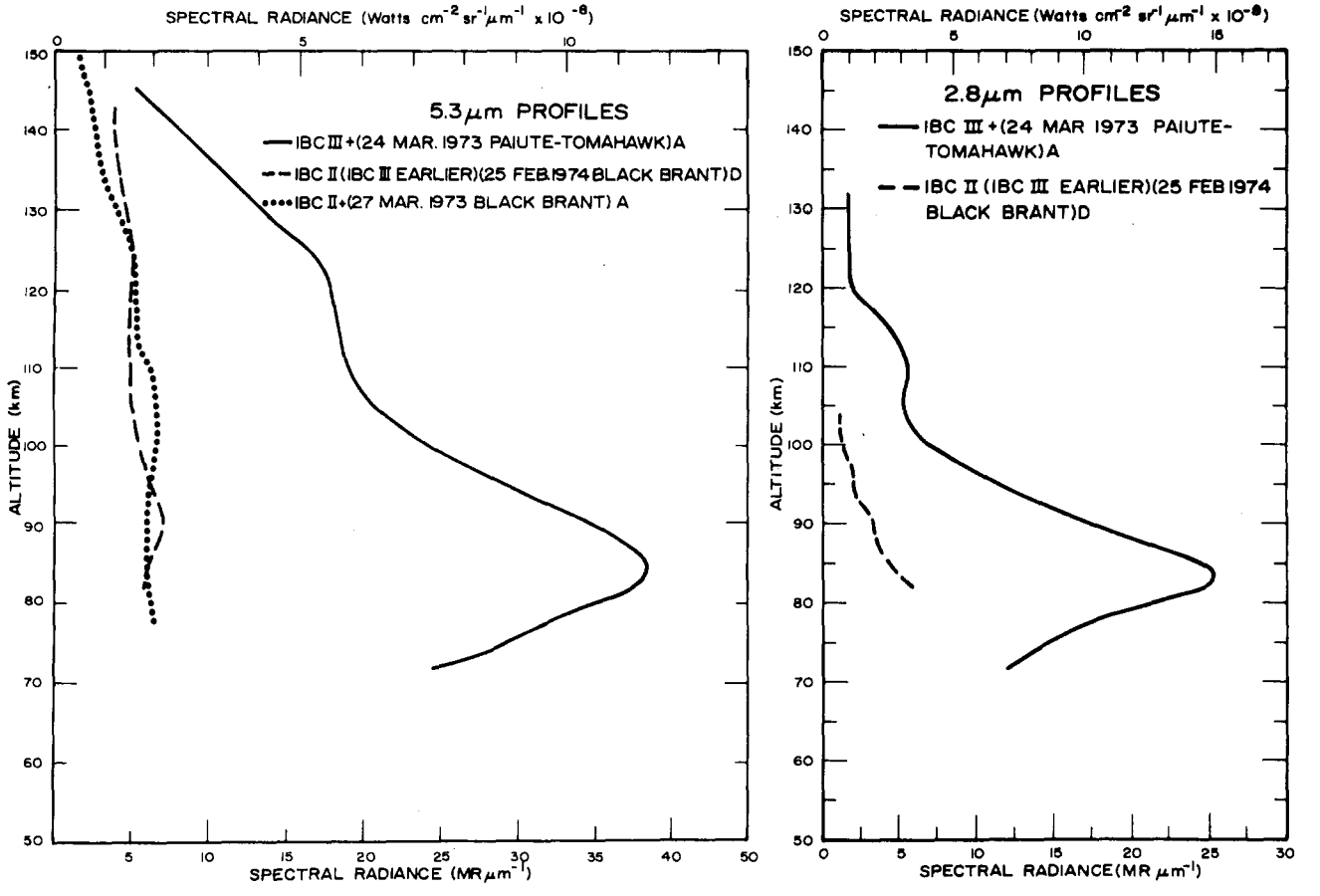

Figure 12-44. Altitude profiles of zenith peak spectral radiance observed in the NO fundamental 5.3 μm and overtone 2.8 μm bands for auroras of different brightness [Stair et al., 1975].

gion of the (1-0) band for moderate auroras and masks any auroral contribution. On the other hand, the long-wavelength cutoff for the recent FWI launch was sufficiently high to show clearly resolved lines of the NO hot bands on the low-frequency side of the NO (1-0) band, whose strength varied in altitude with the energy deposition [Steed et al., 1983; Murphy et al., 1983].

In summary, the intensity in the NO $\Delta v = 1$ system for $v' \geq 2$ responds to energy input from moderately strong auroras in the same way that the NO overtone does, in accord with model predictions. By contrast, for moderately strong auroras the NO (1-0) emission is dominated by airglow from the background atmosphere, as described by Equations (12.16) and (12.17).

As a final note on auroral NO(v), we mention that the HIRIS experiment previously referred to found the NO fundamental emission to be rather strongly enhanced for the very strong IBC III$^+$ aurora which it observed. This is consistent with models of NO emission [Caledonia and Kennealy, 1982], which indicate that chemiluminescent contributions to the NO $\Delta v = 1$ bands become comparable to emission from the background atmosphere under such auroral conditions.

We turn now to the 4.3 μm radiation from the ν_3 asymmetric-stretch mode of CO_2, which results from the emission process

$$CO_2(k\ell\ m) \rightleftarrows CO_2(k,\ell,m-1) + h\nu \qquad (12.20)$$

and, in particular, from the fundamental band emission

$$CO_2(001) \rightleftarrows CO_2(000) + h\nu \qquad (12.21)$$

at 4.26 μm. The altitude profile of this emission in the zenith is indicated in Figure 12-45, showing results from four ICECAP rocket launches [Stair et al., 1975], one launched under quiet conditions and three under various levels of electron precipitation in discrete arcs. The increase of spectral radiance between 75 and 90 km and the peak at 92 km are due to the fact that the ν_3 band becomes optically thick in the zenith at about 90 km. There is a general correlation between the peak radiance level and the electron flux, or the 5577 Å radiance, except that the IBC II$^+$ aurora is considerably less bright at 4.3 μm than the IBC II aurora. The explanation for this apparent anomaly is that a very

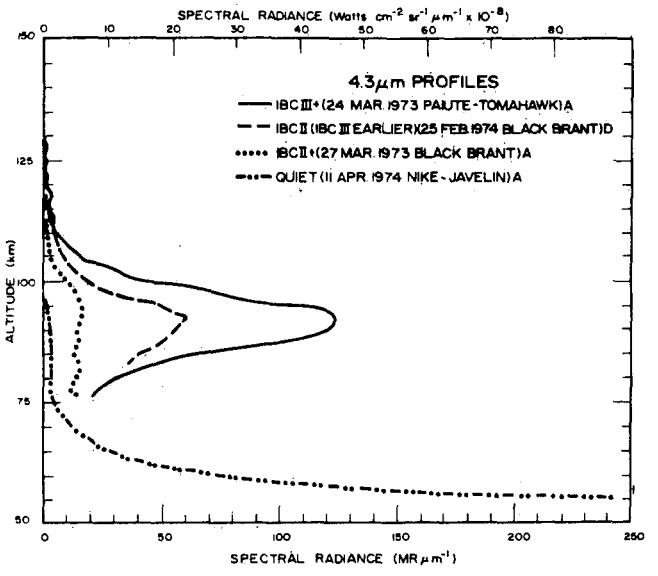

Figure 12-45. Altitude profiles of peak spectral radiance observed in the zenith in the CO_2 4.3 μm band for several classes of aurora [Stair et al., 1975].

bright IBC III arc had occupied the observation region in the latter case before the rocket arrived.

There are two possible sources of aurorally enhanced CO_2 excited vibrational states: (1) direct excitation of CO_2 by precipitating secondary electrons,

$$CO_2\ (000) + e \rightarrow CO_2\ (k\ell m) + e, \qquad (12.22)$$

and (2) vibrational pumping of N_2 by secondary electrons followed by vibration-to-vibration (VV) energy transfer from N_2 to CO_2 (Figure 12-29),

$$N_2 + e \rightarrow N_2^{\ddagger} + e \qquad (12.23a)$$

$$N_2^{\ddagger} + CO_2\ (k,\ell,m-1) \rightleftarrows N_2 + CO_2\ (k\ell m). \qquad (12.23b)$$

Due to the low CO_2 mixing ratio, the rate for the direct process [Equation (12.22)] is too small by several orders of magnitude to explain the observed radiance. Moreover, since the radiative lifetime of the 001 state is $A^{-1} = 2.3 \times 10^{-3}$ s (Table 12-7), the 4.3 μm emission due to the direct reaction of Equation (12.22) should be prompt, following the energy deposition closely in space and time. However, the actual altitude profiles and time histories for the 3914 Å N_2^+ first negative (0-0) radiance and for the 4.3 μm radiance are quite different with the CO_2 emission having a time delay $\gtrsim$ 5 min [Kumer, 1975]. The delay arising from the N_2-CO_2 transfer is responsible for the apparently anomalous brightness at 4.3 μm of the IBC II auroral profile in Figure 12-45.

Another potential mechanism can also be ruled out by the delay as a major factor in accounting for enhanced 4.3 μm emission, namely $NO^+(\Delta v = 1)$ chemiluminescence (Table 12-7). The NO^+ 4.3 μm emission results from vibrationally excited NO^+ produced (Figure 12-29) in reactions such as

$$O_2^+ + NO \rightarrow O_2 + NO^+ \qquad (12.24)$$

and the fourth reaction in Equation (12.19). However, it cannot account for the observed time delay since the time constant for NO^+ formation is $\lesssim$10 s [Kumer, 1975].

On the other hand, the reaction sequence of Equation (12.23) has the slow step (b). Assuming a nitrogen vibrational temperature $T_v = 750$ K, one obtains a time constant of 200 s at an altitude of 115 km for the V-V transfer. The effective time constant for response of the ν_3 emission to electron precipitation is lengthened further by repeated transfer of excitation back and forth between N_2 and CO_2 before photon emission occurs and radiative trapping of the emitted photon. The net effect is an appreciable delay in the 4.3 μm emission. To model the process [Kumer, 1975, 1977], one must add quenching of both $N_2^{\ddagger}$ and the CO_2 excited states to the reaction set of Equations (12.20) and (12.23). The reverse reactions, indicated by backward arrows in the reactions of Equations (12.20) and (12.23b), account for repeated collisional transfer of the excitation between CO_2 and N_2 and for radiative transfer of the ν_3 photons. Kumer [1977] has shown that up to 11 combination bands and isotopic bands must be considered in Equation (12.20) and that an error of a factor of three can result if only the fundamental 001-000 band is used.

12.2.6 Summary

Our current understanding of infrared auroral processes suffers from a lack of sufficient high-resolution, high-sensitivity data on infrared emissions. This deficiency should be partially alleviated as analysis of data from the March 1983 rocketborne FWI experiment proceeds. In addition, several planned rocket-probe and shuttle-based experiments will carry aloft telescoped high-resolution interferometers to view the infrared aurora in earthlimb geometry. The combination of improved sensor sensitivity and the preferred earthlimb viewing aspect with greater auroral brightness will provide a comprehensive spectral survey of auroral infrared emissions. The observation of additional auroral emissions is anticipated as detection thresholds are improved and as infrared measurements are extended to higher spectral resolution and longer wavelengths. These experiments should contribute significantly to our understanding of the production and loss processes for infrared auroral emitters.

There is also a great need for data on the variability of the infrared aurora in order to identify seasonal, diurnal, and latitudinal trends, as well as dependences on solar and

geomagnetic activity. Such a data base may be obtained from a satellite platform or, in part, from ground-based observatories and series of aircraft or balloon flights. None of these experiments are without difficulty; the satellite experiments require solving the problem of maintaining detectors at cryogenic temperatures for extended periods, while ground-based and atmospheric platform experiments suffer from the masking and/or absorption of the auroral emission by the lower atmosphere and from the impossibility of using any limb enhancement technique. Nevertheless, the existence of the space shuttle and the success of unmanned infrared satellite experiments such as IRAS (InfraRed Astronomical Satellite) [Neugebauer et al., 1984] portend well for the future of infrared auroral studies.

ACKNOWLEDGEMENTS

The authors are indebted to A.J. Ratkowski, J.R. Winick, and R.D. Sharma for reading Section 12.2 and making useful recommendations.

REFERENCES

Akasofu, S.-I., "Energy Coupling Between the Solar Wind and the Magnetosphere," *Space Sci. Rev.*, **28:** 121, 1981.

Andriyenko, D.A., "Some Vertical Distribution Patterns," *Geomag. and Aeron.*, **5:** 838, 1965.

Baker, D., W. Pendleton, Jr., A. Steed, R. Huppi, and A.T. Stair, Jr., "Near-Infrared Spectrum of an Aurora," *J. Geophys. Res.*, **82:** 1601, 1977.

Baker, D.J., W.R. Pendleton, Jr., G.J. Romick, V.B. Wickwar, and M.J. Baron, "An Auroral Enhancement of O_2 λ1.27-μm Emission," *Planet. Space Sci.*, **26:** 619, 1978.

Baker, K.D., D.J. Baker, J.C. Ulwick, and A.T. Stair, Jr., "Measurements of 1.5- to 5.3-μm Infrared Enhancements Associated with a Bright Auroral Breakup," *J. Geophys. Res.*, **82:** 3518, 1977.

Banks, P.M., C.R. Chappell, and A.F. Nagy, "A New Model for the Interaction of Auroral Electrons with the Atmosphere: Spectral Degradation, Backscatter, Optical Emission, and Ionization," *J. Geophys. Res.*, **79:** 1459, 1974.

Bates, D.R., "Airglow and Auroras," in *Applied Atomic Collision Physics*, **1,** Academic Press, New York, 1982.

Berger, M.J., S.M. Seltzer, and K. Maeda, "Energy Deposition by Auroral Electrons in the Atmosphere," *J. Atm. Terr. Phys.*, **32:** 1015, 1970.

Berkey, F.T., V.M. Driatskiy, K. Henriksen, B. Hultqvist, D.H. Jelly, T.I. Shchuka, A. Theander, and J. Yliniemi, "A Synoptic Investigation of Particle Precipitation Dynamics for 60 Substorms in IQSY (1964–1965) and IASY (1969)," *Planet. Space Sci.*, **22:** 255, 1974.

Besprozvonnaya, A.S. and T.I. Shchuka, "Distribution of Anomalous Ionization in the High Latitude E Region According to Ground-Based Sounding," *Geomag. Aeron.*, **16:** 430, 1976.

Billingsley, F.P., II, "Calculated Vibration-Rotation Intensities for $NO(X^2\Pi)$," *J. Mol. Spectrosc.*, **61:** 53, 1976.

Borst, W.L. and E.C. Zipf, "Lifetimes of Metastable CO and N_2 Molecules," *Phys. Rev. A*, **3:** 979, 1971.

Boyd, J.S., "Rocket-Borne Measurements of Auroral Electrons," *Rev. Geophys. Space Phys.*, **13:** 735, 1975.

Boyd, J.S., A.E. Belon, and G.C. Romick, "Latitude and Time Variations in Precipitated Electron Energy Inferred from Measurements of Auroral Heights," *J. Geophys. Res.*, **76:** 7694–7700, 1971.

Buchau, J., G.J. Gassmann, C.P. Pike, R.A. Wagner, and J.A. Whalen, "Precipitation Patterns in the Arctic Ionosphere Determined from Airborne Observations," *Ann. Geophys.*, **28:** 443, 1972.

Buchau, J., C.P. Pike and M. Wong, "Detailed Specification of the Arctic Ionosphere and an Application to Three-Dimensional Raytracing," AFCRL-TR-73-0726, AD775084, 1973.

Caledonia, G.E. and J.P. Kennealy, "NO Infrared Radiation in the Upper Atmosphere," *Planet. Space Sci.*, **30:** 1043, 1982.

Chamberlain, J.W., *Physics of the Aurora and Airglow*, Academic Press, New York, 1961.

Cohn, A. and G. Caledonia, "Spatial Distribution of the Fluorescent Radiation Emission Caused by an Electron Beam," *J. Appl. Phys.*, **41:** 3767, 1970.

Dalgarno, A., I.D. Latimer, and J.W. McConkey, "Corpuscular Bombardment and N_2^+ Radiation," *Planet. Space Sci.*, **13:** 1008, 1965.

Eather, R.H. and K.M. Burrows, "Excitation and Ionization by Auroral Protons," *Aust. J. Phys.*, **19:** 309, 1966.

Eyler, E.E. and F.M. Pipkin, "Lifetime Measurements of the B $^3\Pi_g$ State of N_2 Using Laser Excitation," *J. Chem. Phys.*, **79:** 3654, 1983.

Feldman, P.D. and E.P. Gentieu, "The Ultraviolet Spectrum of an Aurora 530-1520 Å," *J. Geophys. Res.*, **87:** 2453, 1982.

Feldstein, Y.I., "Pecularities in the Auroral Distribution and Magnetic Disturbance in High Latitudes Caused by the Asymmetrical Form of the Magnetosphere," *Planet. Space Sci.*, **14:** 121, 1966.

Feldstein, Y.I. and G.V. Starkov, "Dynamics of Auroral Belt and Polar Geomagnetic Disturbances," *Planet. Space Sci.*, **15:** 209, 1967.

Frank, L.A., J.D. Craven, J.L. Burch, and J.D. Winningham, "Polar Views of the Earth's Aurora with Dynamics Explorer," *Geophys. Res. Lett.*, **9:** 1001, 1982.

Freund, R.S., "Molecular-Beam Measurements of the Emission Spectrum and Radiative Lifetime of N_2 in the Metastable E $^3\Sigma_g^+$ State," *J. Chem. Phys.*, **50:** 3734, 1969.

Freund, R.S., "Radiative Lifetime of N_2 (a $^1\Pi_g$) and the Formation of Metastable N_2 (a′ $^1\Sigma_u^-$)," *J. Chem. Phys.*, **56:** 4344, 1972.

Garriott, O.K., "Visual Observations from Space," *J. Opt. Soc. Am.*, **69:** 1064, 1979.

Gassmann, G.J., "Analog Model of the Arctic Ionosphere," AFCRL-TR-73-0151, AD762280, 1973.

Gassman, G.J., J. Buchau, R.A. Wagner, C.P. Pike, and M.G. Hurwitz, "Arctic Ionospheric Modelling—Five Related Papers," AFCRL-72-0305, AD775084, 1972.

Gattinger, R.L. and A. Vallance Jones, "Quantitative Spectroscopy of the Aurora. II. The Spectrum of Medium Intensity Aurora Between 4500 and 8900 Å," *Can. J. Phys.*, **52:** 2343, 1974.

Gattinger, R.L. and A. Vallance Jones, "Quantitative Spectroscopy of the Aurora. V. The Spectrum of Strong Aurora between 10,000 and 16,000 Å," *Can. J. Phys.*, **59:** 480, 1981.

Gilmore, F.R., "Potential Energy Curves for N_2, NO, O_2 and Corresponding Ions," *J. Quant. Spectrosc. Radiat. Transfer*, **5:** 369, 1965.

Goldman, A. and S.C. Schmidt, "Infrared Spectral Line Parameters and the Absorptance Calculations of NO at Atmospheric and Elevated Temperatures for the $\Delta v = 1$ Bands Region," *J. Quant. Spectrosc. Radiat. Transfer*, **15:** 127, 1975.

Goody, R.M., *Atmospheric Radiation*, **1,** Clarendon Press, Oxford, U.K., 1964.

Gordiets, B.F., M.N. Markov, and L.A. Shelepin, "I.R. Radiation of the Upper Atmosphere," *Planet. Space Sci.*, **26:** 933, 1978.

Gussenhoven, M.S., D.A. Hardy, and N. Heinemann,

"Systematics of the Equatorward Diffuse Auroral Boundary," *J. Geophys. Res.*, **88:** 5692, 1983.

Hanson, W.B. (ed.), "Special Issue on Atmospheric Explorer Mission," *Radio Sci.*, **8**(No. 4): 1973.

Harang, L., *The Aurora*, Wiley, New York, 1951.

Hartz, T.R. and N.M. Brice, "The General Pattern of Auroral Particle Precipitation," *Planet. Space Sci.*, **15:** 301, 1967.

Heelis, R.A., J.D. Winningham, W.B. Hanson, and J.L. Burch, "The Relationships Between High-Latitude Convection Reversals and the Energetic Particle Morphology Observed by Atmosphere Explorer," *J. Geophys. Res.*, **85:** 3315, 1980.

Herzberg, G., *Molecular Spectra and Molecular Structure*, **2,** Van Nostrand, Princeton, N.J., 1945.

Herzberg, G., *Molecular Spectra and Molecular Structure*, **1,** second edition, Van Nostrand, New York, 1950.

Herzberg, G., *Molecular Spectra and Molecular Structure*, **3,** Van Nostrand, Princeton, N.J., 1967.

Hilliard, R.L. and G.G. Shepherd, "Upper Atmospheric Temperatures from Doppler Line Widths—IV," *Planet. Space Sci.*, **14:** 383, 1966.

Holzworth, R.H. and C.-I Meng, "Mathematical Representation of the Auroral Oval," *Geophys. Res. Lett.*, **2:** 377, 1975.

Hook, J.L., "Morphology of Auroral Zone Radiowave Absorption in the Alaska Sector," *J. Atmos. Terr. Phys.*, **30:** 1341, 1968.

Huber, K.P. and G. Herzberg, *Molecular Spectra and Molecular Structure*, **4,** Van Nostrand Reinhold, New York, 1979.

Huffman, R.E., F.J. LeBlanc, J.C. Larrabee, and D.E. Paulsen, "Satellite Vacuum Ultraviolet Airglow and Auroral Observations," *J. Geophys. Res.*, **85:** 2201, 1980.

Hunten, D.M., "Some Photometric Observations of Auroral Spectra," *J. Atmos. Terr. Phys.*, **7:** 141, 1955.

Hunten, D.M., E.G. Rawson, and J.K. Walker, "Rapid Measurement of N_2^+ Rotational Temperatures in Aurora," *Can. J. Phys.*, **41:** 258, 1963.

Hunten, D.M., F.E. Roach, and J.W. Chamberlain, "A Photometric Unit for the Airglow and Aurora," *J. Atmos. Terr. Phys.*, **8:** 345, 1956.

Huppi, R.J., and A.T. Stair, Jr., "Aurorally Enhanced Infrared Emissions," *Appl. Opt.*, **18:** 3394, 1979.

Huppi, E.R., J.W. Rogers, and A.T. Stair, Jr., "Aircraft Observations of the Infrared Emission of the Atmosphere in the 700–2800 cm^{-1} Region," *Appl. Opt.*, **13:** 1466, 1974.

International Union of Geodesy and Geophysics, *International Auroral Atlas*, Edinburgh University Press, 1963.

Jasperse, J.R. and B. Basu, "Transport Theoretic Solutions for Auroral Proton and H Atom Fluxes and Related Quantities," *J. Geophys. Res.*, **87:** 811, 1982.

Jones, R.A. and M.H. Rees, "Time Dependent Studies of the Aurora, I. Ion Density and Composition," *Planet. Space Sci.*, **21:** 537, 1973.

Kennealy, J.P. and F.P. Del Greco, "The Kinetics of Atmospheric Radiative Processes in the Infrared," Chapter 11, *Defense Nuclear Agency Reaction Rate Handbook*, second edition, edited by M.H. Bortner and T. Baurer, DNA 1948H, 1972.

Kennealy, J.P., F.P. DelGreco, G.E. Caledonia, and B.D. Green, "Nitric Oxide Chemiexcitation Occurring in the Reaction Between Metastable Nitrogen Atoms and Oxygen Molecules," *J. Chem. Phys.*, **69:** 1574, 1978.

Kockarts, G., "Nitric Oxide Cooling in the Terrestrial Atmosphere," *Geophys. Res. Lett.*, **7:** 137, 1980.

Krukonis, A.P. and J.A. Whalen, "Occurrence and Lifetimes of Discrete Auroras Near Midnight," *J. Geophys. Res.*, **85:** 119, 1980.

Krupenie, P.H., "The Spectrum of Molecular Oxygen," *J. Phys. Chem. Ref. Data*, **1:** 423, 1972.

Kumer, J.B., "Summary Analysis of 4.3μm Data," in *Atmospheres of Earth and the Planets*, edited by B.M. McCormac, D. Reidel, Dordrecht, Holland, 347–358, 1975.

Kumer, J.B., "Theory of the CO_2 4.3-μm Aurora and Related Phenomena," *J. Geophys. Res.*, **82:** 2203, 1977.

Loftus, A. and P.H. Krupenie, "The Spectrum of Molecular Nitrogen," *J. Phys. Chem. Ref. Data*, **6:** 113, 1977.

Lui, A.T.Y. and C.D. Anger, "A Uniform Belt of Diffuse Aurora and Airglow from ISIS 2 Spacecraft," *Planet. Space Sci.*, **21:** 819, 1973.

Lui, A.T.Y., P. Perreault, S.-I. Akasofu, and C.D. Anger, "The Diffuse Aurora," *Planet. Space Sci.*, **21:** 857, 1973.

Lui, A.T.Y., D. Venkatesan, C.D. Anger, S.-I. Akasofu, W.J. Heikkila, J.D. Winningham, and J.R. Burrows, "Simultaneous Observations of Particle Precipitations and Auroral Emissions by the ISIS 2 Satellite in the 19–24 MLT Sector," *J. Geophys. Res.*, **82:** 2210, 1977.

McClatchey, R.A., W.S. Benedict, S.A. Clough, D.E. Burch, R.F. Calfee, K. Fox, L.S. Rothman, and J.S. Garing, "AFCRL Atmospheric Absorption Line Parameters Compilation," AFCRL TR-73-0096, AD762904, 1973.

Mende, S.B. and R.H. Eather, "Monochromatic All Sky Observations and Auroral Precipitation Patterns," *J. Geophys. Res.*, **81:** 3771, 1976.

Meng, C.-I., "Diurnal Variation of the Auroral Oval Size," *J. Geophys. Res.*, **84:** 5319, 1979.

Meng, C.-I., R.H. Holzworth, and S.-I. Akasofu, "Auroral Circle—Delineating the Poleward Boundary of the Quiet Auroral Belt," *J. Geophys. Res.*, **82:** 164, 1977.

Muldrew, D.B., "F-Layer Ionization Troughs Deduced from Alouette Data," *J. Geophys. Res.*, **70:** 2635, 1965.

Murphy, R., R. Sharma, R. Picard, J. Winick, K.D. Baker, and J.C. Ulwick, "Preliminary Interpretation of Infrared Interferometer Rocket Measurements," *Eos*, **64:** 785, 1983.

Neugebauer, G., et al., "The Infrared Astronomical Satellite (IRAS) Mission," *Astrophys. J.*, **278:** L1, 1984.

Omholt, A., "The Auroral E-Layer Ionization and the Auroral Luminosity," *J. Atmos. Terr. Phys.*, **7:** 73, 1955.

O'Neil, R.R., F. Bien, D. Burt, J.A. Sandock, and A.T. Stair, Jr., "Summarized Results of the Artificial Auroral Experiment, Precede," *J. Geophys. Res.*, **83:** 3273, 1978a.

O'Neil, R.R., O. Shepherd, W.P. Reidy, J.W. Carpenter,

T.N. Davis, D. Newell, J.C. Ulwick, and A.T. Stair, Jr., "Excede 2 Test, an Artificial Auroral Experiment: Ground-Based Optical Measurements," *J. Geophys. Res.*, **83:** 3281, 1978b.

O'Neil, R.R., E.T.P. Lee, and E.R. Huppi, "Auroral O(^{1}S) Production and Loss Processes: Ground-Based Measurements of the Artificial Auroral Experiment Precede," *J. Geophys. Res.*, **84:** 823, 1979.

O'Neil, R.R., A.T. Stair, Jr., W.R. Pendleton, Jr., and D.A. Burt, "The EXCEDE SPECTRAL Artificial Auroral Experiment: An Overview," in *Artificial Particle Beams in Space Plasma Studies,* edited by B. Grandal, Plenum, New York, pp. 207–215, 1982.

Peterson, L.R., T. Sawada, J.N. Bass, and A.E.S. Green, "Electron Energy Deposition in a Gaseous Mixture," *Computer Phys. Commun.*, **5:** 239, 1973.

Pike, C.P., "An Analytical Model of the Main F-Layer Trough," AFGL TR-76-0098, ADA026031, 1976.

Pike, C.P. and J.A. Whalen, "Satellite Observations of Auroral Substorms," *J. Geophys. Res.*, **79:** 985, 1974.

Piper, L.G., "The Excitation of O(^{1}S) in the Reaction Between $N_2(A\ ^3\Sigma_u^+)$ and O(^{3}P)," *J. Chem. Phys.*, **77:** 2373, 1982.

Piper, L.G., G.E. Caledonia, and J.P. Kennealy, "Rate Constants for Deactivation of $N_2(A)$ $v' = 0,1$ by O_2," *J. Chem. Phys.*, **74:** 2888, 1981a.

Piper, L.G., G.E. Caledonia, and J.P. Kennealy, "Rate Constants for Deactivation of $N_2(A\ ^3\Sigma_u^+, v' = 0,1)$ by O," *J. Chem. Phys.*, **75:** 2847, 1981b.

Rawlins, W.T., G.E. Caledonia, J.J. Gibson, and A.T. Stair, Jr., "Infrared Emission from NO ($\Delta v = 1$) in an Aurora: Spectral Analysis and Kinetic Interpretation of HIRIS Measurements," *J. Geophys. Res.*, **86:** 1313, 1981a.

Rawlins, W.T., G.E. Caledonia, and J.P. Kennealy, "Observation of Spectrally Resolved Infrared Chemiluminescence from Vibrationally Excited $O_3(\nu_3)$," *J. Geophys. Res.*, **86:** 5247, 1981b.

Rearwin, S. and E.W. Hones, "Near Simultaneous Measurement of Low-Energy Electrons by Sounding Rocket and Satellite," *J. Geophys. Res.*, **79:** 4322, 1974.

Rees, M.H., "Auroral Ionization and Excitation by Incident Energetic Electrons," *Planet. Space Sci.*, **11:** 1209, 1963.

Rees, M.H., "Note on the Penetration of Energetic Electrons into the Earth's Atmosphere," *Planet. Space Sci.*, **12:** 722, 1964.

Rees, M.H. and D. Luckey, "Auroral Electron Energy Derived from Ratio of Spectroscopic Emissions 1. Model Computations," *J. Geophys. Res.*, **79:** 5181, 1974.

Rees, M.H. and R.G. Roble, "Effect of a Horizontal Wind on 1.27-μm Auroral Emission from O_2 ($^1\Delta_g$) Molecules," *J. Geophys. Res.*, **85:** 4295, 1980.

Rees, M.H., A.I. Stewart, and J.C.G. Walker, "Secondary Electrons in Aurora," *Planet. Space Sci.*, **17:** 1997, 1969.

Reidy, W.P., T.C. Degges, A.G. Hurd, A.T. Stair, Jr., and J.C. Ulwick, "Auroral Nitric Oxide Concentration and Infrared Emission," *J. Geophys. Res.*, **87:** 3591, 1982.

Robinson, R.M., R.R. Vondrak, and T.A. Potemra, "Electrodynamic Properties of the Evening Sector Ionosphere Within the Region 2 Field-Aligned Current Sheet," *J. Geophys. Res.*, **87:** 731, 1982.

Roble, R.G. and J.M. Gary, "The Effect of Horizontal Transport on Auroral NO Densities," *Geophys. Res. Lett.*, **6:** 703, 1979.

Roble, R.G. and M.H. Rees, "Time-Dependent Studies of the Aurora: Effects of Particle Precipitation on the Dynamic Morphology of Ionospheric and Atmospheric Properties," *Planet. Space Sci.*, **25:** 991, 1977.

Rothman, L.S., "AFGL Atmospheric Absorption Line Parameters Compilation: 1980 Version," *Appl. Opt.*, **20:** 791, 1981.

Rothman, L.S. and L.D.G. Young, "Infrared Energy Levels and Intensities of Carbon Dioxide—II," *J. Quant. Spectrosc. Radiat. Transfer*, **25:** 505, 1981.

Rothman, L.S., A. Goldman, J.R. Gillis, R.R. Gamache, H.M. Pickett, R.L. Poynter, N. Husson, and A. Chedin, "AFGL Trace Gas Compilation: 1982 Version," *Appl. Opt.*, **22:** 1616, 1983a.

Rothman, L.S., R.R. Gamache, A. Barbe, A. Goldman, J.R. Gillis, L.R. Brown, R.A. Toth, J.-M. Flaud, and C. Camy-Peyret, "AFGL Atmospheric Absorption Line Parameters Compilation: 1982 Edition," *Appl. Opt.*, **22:** 2247, 1983b.

Sandford, B.P., "Variations of Auroral Emissions with Time, Magnetic Activity and the Solar Cycle," *J. Atmos. Terr. Phys.*, **30:** 1921, 1968.

Seaton, M.J., "Excitation Processes in the Aurora and Airglow. I. Absolute Intensities, Relative Ultraviolet Intensities, and Electron Densities in High Latitude Aurorae," *J. Atmos. Terr. Phys.*, **4:** 285, 1954.

Sharber, J.R., "The Continuous (Diffuse) Aurora and Auroral-E Ionization," in *Physics of Space Plasmas,* edited by T.S. Chang, B. Coppi, and J.R. Jasperse, *SPI Conference Proceedings and Reprint Series, 4,* Scientific Publishers, Cambridge, Mass., 1981.

Sharp, W.E., "The Ultraviolet Aurora: The Spectrum Between 2100 Å and 2300 Å," *Geophys. Res., Lett.*, **5:** 703, 1978.

Sharp, W.E. and M.H. Rees, "Auroral Spectrum between 1200 and 4000 Angstroms," *J. Geophys. Res.*, **77:** 1810, 1972.

Sheehan, R.E. and R.L. Carovillano, "Characteristics of the Equatorward Auroral Boundary Near Midnight Determined from DMSP Images," *J. Geophys. Res.*, **83:** 4749, 1978.

Sheehan, R.E., R.L. Carovillano, and M.S. Gussenhoven, "Occurrence and Recurrence in Auroral Activity in DMSP Images," *J. Geophys. Res.*. **87:** 3581, 1982.

Shepherd, M.M. and R.H. Eather, "On the Determination of Auroral Electron Energies and Fluxes from Optical Spectral Measurements," *J. Geophys. Res.*, **81:** 1407, 1976.

Slater, D.W., L.L. Smith, and E.W. Kleckner, "Correlated Observations of the Equatorward Diffuse Auroral Boundary," *J. Geophys. Res.*, **85:** 531, 1980.

Spiro, R.W., P.F. Reiff, and L.J. Maher, "Precipitating Electron Energy Flux and Auroral Zone Conductances—An Empirical Model," *J. Geophys. Res.*, **87:** 8215, 1982.

Stair, A.T., Jr., J.C. Ulwick, K.D. Baker, and D.J. Baker, "Rocketborne Observations of Atmospheric Infrared Emissions in the Auroral Region," in *Atmospheres of Earth and the Planets,* edited by B.M. McCormac, D. Reidel, Dordrecht, Holland, pp. 335–346, 1975.

Stair, A.T., Jr., R. Nadile, J.C. Ulwick, K.D. Baker, and D.J. Baker, "Infrared Measurements of Aurora, Airglow and the Upper Atmosphere," in *Proceedings of the 8th Annual Meeting on Upper Atmospheric Studies by Optical Methods,* edited by E. O'Mongain, University College, Dublin, pp. 27–35, 1980.

Stair, A.T., Jr., J. Pritchard, I. Coleman, C. Bohne, W. Williamson, J. Rogers, and W.T. Rawlins, "Rocketborne Cryogenic (10 K) High-Resolution Interferometer Spectrometer Flight HIRIS: Auroral and Atmospheric IR Emission Spectra," *Appl. Opt.,* **22:** 1056, 1983.

Starkov, G.V., "Auroral Heights in the Polar Cap," *Geomag. Aeron.,* **8:** 28, 1968.

Starkov, G.V., "Analytical Representation of the Equatorial Boundary of the Oval Auroral Zone," *Geomag. Aeron.,* **9:** 614, 1969.

Starkov, G.V. and Y.I. Feldstein, "Position of the Auroral Belt at Night During the IGY and IQSY" in *Complex Investigations of the Polar Ionosphere,* edited by Isaev, Nauka Press, Leningrad, 1970.

Steed, A., J.C. Ulwick, C. Harris, F. Cook, and R. Straka, "Rocketborne Interferometer Measurements of SWIR/MWIR Spectra," *Eos,* **64:** 784, 1983.

Stolarski, R.S. and A.E.S. Green, "Calculations of Auroral Intensities from Electron Impact," *J. Geophys. Res.,* **72:** 3967, 1967.

Strickland, D.J., D.L. Book, T.P. Coffey, and J.A. Fedder, "Transport Equation Techniques for the Deposition of Auroral Electrons," *J. Geophys. Res.,* **81:** 2755, 1976.

Strickland, D.J., J.R. Jasperse, and J.A. Whalen, "Dependence of Auroral FUV Emissions on the Incident Electron Spectrum and Neutral Atmosphere," *J. Geophys. Res.,* **88:** 8051, 1983.

Swider, W. and R.S. Narcisi, "Auroral E-Region: Ion Composition and Nitric Oxide," *Planet. Space Sci.,* **25:** 103, 1977.

Torr, M.R. and D.G. Torr, "The Role of Metastable Species in the Thermosphere," *Rev. Geophys. Space Phys.,* **20:** 91, 1982.

Vallance Jones, A., *Aurora,* D. Reidel, Dordrecht, Holland, 1974.

Vallance Jones, A. and R.L. Gattinger, "Quantitative Spectroscopy of the Aurora. III. The Spectrum of Medium Intensity Aurora Between 3100 Å and 4700 Å," *Can. J. Phys.,* **53:** 1806, 1975.

Vallance Jones, A. and R.L. Gattinger, "Quantitative Spectroscopy of the Aurora. IV. The Spectrum of Medium Intensity Aurora between 8800 Å and 11 400 Å," *Can. J. Phys.,* **54:** 2128, 1976.

Wadzinski, H.T. and J.R. Jasperse, "Low Energy Electron and Photon Cross Sections for O, N_2, and O_2, and Related Data," AFGL-TR-82-0008, ADA118921, 1982.

Wagner, R.A. and C.P. Pike, "A Discussion of Arctic Ionograms" in *Radar Propagation in the Arctic,* Chapter 4, edited by J. Frihagen, Technical Editing and Reproduction, London, 1972.

Wagner, R.A., A.L. Snyder, and S.-I. Akasofu, "The Structure of the Polar Ionosphere During Exceptionally Quiet Periods," *Planet. Space Sci.,* **21:** 1911, 1973.

Werner, H.-J. and P. Rosmus, "Ab Initio Calculations of Radiative Transition Probabilities in the $X\ ^1\Sigma^+$ Ground State of the NO^+ Ion," *J. Mol. Spectrosc.,* **96:** 362, 1982.

Whalen, J.A., "Auroral Oval Plotter and Nomograph for Determining Corrected Geomagnetic Local Time, Latitude and Longitude for High Latitudes in Northern Hemisphere," AFCRL 70-0422, AD713170, 1970.

Whalen, J.A. "Characteristics of the High Latitude Ionosphere Produced by Auroral Particle Precipitation," in AGARD Conference Proceedings, No. 263, *Special Topics in HF Propagation,* 1979.

Whalen, J.A. "General Characteristics of the Auroral Ionosphere" in *Physics of Space Plasmas,* edited by T.S. Chang, B. Coppi, and J.R. Jasperse, SPI Conference Proceedings and Reprint Series 4, Scientific Publishers, Cambridge, Mass., 1981.

Whalen, J.A., "A Quantitative Description of the Spatial Distribution and Dynamics of the Energy Flux in the Continuous Aurora," *J. Geophys. Res.,* **88:** 7155, 1983.

Whalen, J.A. and J.R. Sharber, "TheNighttime Auroral-E Layer: Partical Production, Latitudinal and Longitudinal Structure and Dynamics" in *The Effects of the Ionosphere on Radiowave Systems,* edited by J. Goodman and F. Clarke, U.S. Government Printing Office, Washington, D.C., 1981.

Whalen, J.A., J. Buchau, and R.A. Wagner, "Airborne Ionospheric and Optical Measurements of Noontime Aurora," *J. Atmos. Terr. Phys.,* **33:** 661, 1971.

Whalen, J.A., R.A. Wagner, and J. Buchau, "A 12-Hour Case Study of Auroral Phenomena in the Midnight Sector: Oval, Polar Cap and Continuous Auroras," *J. Geophys. Res.,* **82:** 3529, 1977.

Winckler, J.R., "The Use of Artificial Electron Beams as Probes of the Distant Magnetosphere," in *Artificial Particle Beams in Space Plasma Studies,* edited by B. Grandal, Plenum, New York, pp. 3–33, 1982.

Winningham, J.D., F. Yasuhara, S.-I. Akasofu, and W.J. Heikkila, "The Latitudinal Morphology of 10 eV to 10 keV Electron Fluxes during Magnetically Quiet and Disturbed Times in the 2100 to 0300 MLT Sector," *J. Geophys. Res.,* **80:** 3148, 1975.